M Subdwarfs and the Population II Luminosity Function

Thesis by

John E. Gizis

In Partial Fulfillment of the Requirements

for the Degree of

Doctor of Philosophy

California Institute of Technology

Pasadena, California

1998

(Submitted October 17, 1997)

Acknowledgements

This thesis would not have been possible without the advice and encouragement of Neill Reid. Neill taught me how to be a scientist, from proposals to observations to publications. He was always encouraging, understanding, and, perhaps most importantly, available for discussions. I has been both a mentor and a colleague. He has also been a friend. I have learned many things from him; indeed, I will be always grateful to know that "outwith" is a word.

I would also like to thank the faculty of Caltech. In particular, Jeremy Mould provided important advice during my first year here. Jim McCarthy was always a helpful source of information on echelle spectroscopy. I spent what seems like most of my graduate career using his excellent spectrograph on the 60-in. telescope. He also supervised the upgrade of that spectrograph which gave me a "hands on" knowledge of instrumentation. In addition, I would like to thank Suzanne Hawley at Michigan State University, whose collaboration on the Palomar/MSU Nearby-Star Spectroscopic Survey was an essential background to this thesis. I am grateful to Chris Tinney for providing his Ph.D. thesis data. Davy Kirkpatrick and Todd Henry shared their comments on the classification procedures used in this work. I would also like to thank Pierre Demarque and David Guenther for their mentorship when I was a Yale undergraduate.

The students and postdocs made graduate school a remarkably enjoyable and stimulating experience. I would especially like to thank Gautam Vasisht, Erik Leitch, David Hogg, Chris Fassnacht, Jagmit Sandhu, Angela Putney, Lin Yan, Patrick Ogle, Rebecca Bernstein, Mike Pahre, Rudi Danner, Ben Oppenheimer, Martin Shepherd, Donna Womble, Ian Smail, and Adam Showman for their friendship and many scientific discussions. I must also thank Jamie Schlessman who has always provided encouragement.

This thesis is largely based upon data from Palomar observatory. I cannot say

enough about the thanks I owe to Skip Staples for his assistance at the 60-inch telescope. His knowledge and experience always made observing runs as productive and enjoyable as possible. I would also like to thank Juan Carrasco, Jean Mueller, Kelly McIlrath, Rick Burruss, and Karl Dunscombe for their assistance at the telescope. Hal Petrie, Mike Doyle, Dave Tennant, Bob Thicksten, John Henning, Greg Van Idsinga, and the rest of the Palomar staff made this work possible with their fine support of the telescopes and instruments. DiPauli, Roseann, Michelle, and Audrey made the Monastery a wonderful place to stay. I also thank the staff of Las Campanas observatory.

I am extremely grateful for support from a Greenstein Fellowship, a Kingsley Fellowship, and NASA grants GO-06344.01-95A, GO-05913.01-94A, and GO-5353.01-93A. In addition, this work has been made possible by the generous support of astronomy by both private donors and the American public,

Finally, I must thank the people who meant the most to me these past five years. Sheri Chinen Biesen's friendship, love, and support have meant so much to me. I hope that I can be as helpful as she finishes her own dissertation. I also thank my brothers Alec and Rob and my parents. Their love and support have made everything possible.

Abstract

We present a spectroscopic classification system for M-dwarfs and M-subdwarfs based on quantitative measures of TiO and CaH features in the region $\lambda\lambda 6200-7400$Å. Our sample of cool stars covers the range from solar metallicity stars to the most extreme subdwarfs known. Using synthetic spectra computed by Allard and Hauschildt (1995), we derive metallicities for the stars. Stars are classified as dwarfs (M V), subdwarfs (sdM), or extreme subdwarfs (esdM). These classifications correspond to $[m/H] \approx$ 0.0, -1.2, and -2.0 respectively. Our metallicity scale agrees with theoretical HR diagrams and HST globular cluster measurements. We discuss some nearby subdwarfs of particular interest in light of our metallicity scale.

We present spectra of three M subdwarfs which are common proper motion companions to F or G subdwarfs of known metallicity. The assumption that the companions have the same composition allows us to test the Gizis (1997, AJ, 113, 806) M subdwarf classification system and its correspondence to metallicity. The results are in excellent agreement with the Gizis (1997) scale, thereby showing that the Allard & Hauschildt (1995, ApJ, 445, 433) Extended model atmospheres agree well in the 6200 – 7400Å region for cool metal-poor stars. We also show that the results are consistent with the main sequences of globular clusters using the Reid (1997, AJ, in press) distance scale.

We use optical spectra as well as optical and infrared broadband photometry to constrain the effective temperatures of M subdwarfs. We show that the coolest subdwarfs known have $T_{eff} \approx 3000$ K.

We present spectroscopic observations of two halo M subdwarfs which have $H\alpha$ emission lines. We show that in both cases close companions are the likely cause of the chromospheric activity in these old, metal-poor stars. We argue that Gl 781 A's unseen companion is most likely a cool helium white dwarf. Gl 455 is a near-equal-mass M subdwarf system. Gl 781 A is rapidly rotating with $v \sin i \approx 30$ km s^{-1}. The

properties of the chromosphere and X-ray coronae of these systems are compared to M dwarfs with emission (dMe). Although the relative strength of the X-ray coronae to the $H\alpha$ emission are similar to that seen in field and young cluster dMe, Gl 781 A's activity level is weaker than the young cluster dMe. This suggests that different ages and/or metallicities can make two otherwise equally rapidly rotating, equal-mass stars have different activity levels.

Using a proper motion survey based upon the two Palomar Sky Surveys, We measure the luminosity function of the low-mass end of the field Population II. We combine this with earlier measurements of higher mass stars to show that the luminosity function increases down to $M_I \approx 9.5$, but may be flattening at the lowest luminosities $M_I > 9.5$. We discuss the constraints this puts on the mass function of metal-poor stars. The mass function is consistent with a power-law of slope $\alpha \approx -1.35$.

Contents

List of Figures

List of Tables

Chapter 1 Introduction

1.1 The Population II

1.1.1 Discovery of the Population II

In this century, astronomers have learned that our Galaxy, the Milky Way, is a spiral galaxy with our own Sun lying in the disk. The vast majority of the nearby stars of the solar neighborhood are members of this disk population, with near-solar metallicity and space velocity roughly similar to the Sun's own motion. At the Sun's position of $\sim$ 8 kiloparsecs from the Galactic center, the disk rotates at $\sim$ 220 km s$-$1 (Reid 1993). In addition to this dominant disk population (called Population I after Baade 1944), a second halo population (Population II) is known to exist, with its most notable members being the old, metal-poor globular clusters. The halo has small rotational velocity and is nearly spherical; its star follow highly elliptical orbits in contrast to the nearly circular orbits of disk stars. The identification of the halo population involved decades of work, starting with empirical spectral classifications and kinematics which preceding the breakthroughs in astrophysics which allowed the nature of the halo to be understood.

The presence of spectroscopically peculiar stars in our Galaxy was noted over eighty years ago by Adams (1915), who found that HD 19445 and two other stars had weak hydrogen lines for their otherwise A-type spectra. Adams remarked that these stars also had large space velocities and probable low luminosities. Additional stars of this type were found over the following decades, and were sometimes termed "intermediate white dwarfs" due to their position below the main sequence but above the white dwarfs in the HR diagram. Kuiper (1948), who used the term "subdwarfs" for these stars, showed they typically lie on average 1.9 magnitudes below the main sequence.

These nearby field high-velocity stars were linked by Baade (1944) to the Galactic globular clusters and elliptical galaxies in his introduction of stellar populations. What we now recognize as the old Population II was distinguished from the young Population I stars that make up the disks of spiral galaxies.

The realization that the high-velocity subdwarfs are metal-poor was made by Chamberlain & Aller (1951), who studied two of Adam's original stars. Previously it had been thought that these stars with weak hydrogen lines were hydrogen-poor (e.g, Kuiper 1948). Roman (1954) showed that selecting the most metal-poor stars defined a population with very extreme kinematics, with small Galactic rotational velocity and little concentration towards the Galactic plane.

These pieces were finally put together by Eggen, Lynden-Bell, & Sandage (1962) who presented a model (hereafter ELS) of the formation of the galaxy. The Population II stars, or Galactic halo stars, formed very early in the history of the Galaxy during a rapid (few $\times 10^8$ yr) collapse from a roughly spherical gas cloud to the disk structure that exists today. During this time, the gas was rapidly enriched with metals. Thus, the high-velocity and low metallicity of Population II reflects its origin in the formation of the Galaxy. A model involving mergers and a slower enrichment timescale was advanced by Searle & Zinn (1978) The details of the collapse timescale and enrichment history have since been a lively subject of debate (see the review by Majewski 1993).

1.1.2 Halo vs. Disk

Studies of the halo population are complicated by the fact that there are many more high-velocity/high-altitude stars than a simple prediction based upon the observed scale height of $z_0 \approx 350$ parsecs or $\sigma_W = 20$ km s^{-1}[1]. This intermediate population, which was termed the "thick disk " (Gilmore & Reid 1983), has a scale height of ~ 1200 pc and and represents 2% of stars locally.

[1]We use the standard notation of (U,V,W) for the space velocity components. U is positive towards the Galactic Center ($l = 0, b = 0$), W is positive towards the North Galactic Pole, and V is positive in the direction of Galactic rotation

Starcounts down to $V \sim 22$ (Bahcall et al. 1983; Reid & Majewski 1993) can be used to constrain the halo luminosity function and show that the halo represents $0.1 - 0.3\%$ of stars locally (at least for the upper main sequence with $3 \lesssim M_V \lesssim 8$. A more precise estimate, however, is difficult because there is significant degeneracy in the model parameters. One can "trade off" between the local normalization of the halo-to-disk or IPII-to-disk ratios, the halo or IPII density law, and even the shape of the luminosity function near the turnoff (Reid & Majewski 1993). In order to probe to fainter stars with $M_V > 8$, one must clearly extend the starcount surveys to fainter (and redder) magnitudes. Reid et al. (1996) have shown that deeper counts, however, do not give strong constraints on the halo luminosity function because of the difficulty of star-galaxy separation from the ground and the small fields of views available from space and the inability to reach beyond the distance where the IPII dominates. Even at $R \sim 23$, near-solar metallicity M dwarfs dominate the starcounts, as can be seen in the stellar spectra obtained in course of Keck redshift surveys (Reid et al. 1997).

1.1.3 Properties of the Halo

Studies of the kinematics of the halo population do not agree as well as one might like. Studies based upon nearby proper motion stars (e.g., Bahcall & Casertano 198?) and non-kinematically selected nearby metal-poor stars (Norris 1986) have found a prograde rotation of the halo. On the other hand, most surveys of distant ($d > 5$ kpc) stars have found a retrograde rotation for the halo (Majewski 1993). Beers & Sommer-Larson (1995) have analyzed the radial velocities of a sample of metal-poor stars selected without kinematic bias and found hotter halo kinematics than most previous studies with essential no net halo rotation. Studies of the most metal-poor RR Lyrae also find hot kinematics (Layden et al. 1996).

The age of the halo is determined by stellar structure models of globular cluster stars. Until recently, most models of globular clusters gave ages of 15×10^9 years for the most metal-poor clusters (VandenBerg et al. 1996). Recent trigonometric parallaxes of G subdwarfs determined by the Hipparcos satellite project, have led to

revised distances to globular clusters and lower ages ($\sim 11 \times 10^9$ years) which agree better with standard cosmological models (Reid 1997; Gratton et al. 1997).

The abundance distribution of the halo has been determined using the survey of 1022 blue proper motion stars undertaken by Carney et al. (1996). They define the halo as the 135 stars with $V < -220$ km s^{-1} . The metallicity distribution peaks at $[m/H] = -1.62$ and follows a roughly gaussian shape with full-width-at-half-maximum of 1.2 dex in $[m/H]$. This is the same peak metallicity as seen in halo globular clusters, but the field distribution has stronger tails, with both more metal-poor ($[m/H] < -2.5$) and metal-rich ($[m/H > -1$) stars. Carney et al. (1996) note that the metallicity distribution is consistent with simple enrichment models — no precursor "Population III" is required to provide metals to explain the abundances of Population II stars.

In recent years, the possibility that the halo is itself made up of two different populations has been advanced by Norris (1994) and Carney et al. (1996). One component would be a "proto-disk" population whose gas contracted, in the manner described by ELS, into the disk. The second component is an "accreted" population, which perhaps formed in manner similar to the Searle & Zinn (1979) model, in which fragments and accreted satellite galaxies are gathered into the halo. The "accreted population" is nearly spherical and has no net or even retrograde rotation, while the "proto-disk" population is flattened with a net prograde rotation. The existence of two halo populations may explain the sometimes inconsistent kinematics found by different surveys, as different proportions of the two populations may enter surveys with different selection criteria.

1.2 The Very Low Mass Stars

The properties of the halo listed above have all been determined from nearly solar-mass stars, either still on the main sequence (FGK subdwarfs) or evolved (RR Lyraes, red giants). Based on studies of the disk population, we know that there are more stars at lower mass than at higher mass. Analysis of both the nearest stars within

eight parsecs and surveys to $\sim$ 100 parsecs yields a consistent luminosity function which can be transformed to a mass function (Reid & Gizis 1997) This mass function ($\Psi(M)$) can be usefully described as power law, with

$$\Psi(m) = \frac{dN}{dM} \propto M^{-\alpha} \tag{1.1}$$

and $\alpha = 1.05$ for $0.1M_{\odot} < M < 1.0M_{\odot}$. For comparison, higher mass stars ($M > 1M_{\odot}$) show a index of 2.35 (Salpeter 1955).

The present day Population II mass function for low mass stars ($M \lesssim 0.7M_{\odot}$), which have not yet evolved significantly, reflects the mass function that was originally formed early in the Universe's history. Star formation conditions were different at that time — for example, observations of the Population II stars existing today show that the gas clouds were low-metallicity and followed much different orbits that would collide at high velocity. Whether or not the Population II mass function differs significantly from the Population I mass function is one of the few observational clues available to constrain models of early star formation. Schmidt (1975) showed that the observed Population II luminosity function, based on nearby proper motion stars, is consistent with power-laws of index $\alpha = 1$ or $\alpha = 2$, at least down to 0.2 or $0.3M_{\odot}$.

Further extension of this work to low-luminosities has been difficult, in part because the lowest-mass stars have been poorly understood. Indeed, while some metal-poor M stars were noted at least as long ago as Joy (1947), it is now clear that M subdwarfs with metallicities typical of the peak of halo distribution ($[m/H < -1.5$) were not identified until after Luyten's publication of the high proper motion, faint, red stars found from his Palomar survey (Luyten 1979). Very metal-poor M-subdwarfs stars were then identified by Liebert et al. (1979), Ake & Greenstein (1980), and Hartwick et al. (1982). Each of these studies identified subdwarfs as having an extreme deficiency of absorption by the TiO molecule but strong hydride absorption. Monet et al. (1992) obtained parallaxes for those faint stars using CCDs and found that they are 4 magnitudes subluminous in the $V - I, M_V$ HR diagram.

At the same time as good parallax information has become available for these

stars, two other new tools have arrived. New model atmospheres have been computed by Allard & Hauschildt (1995), which as we will show in Chapters 2 and 4, allow observations of these stars to be interpreted. The refurbishment of Hubble Space Telescope has allowed the lower main sequence in globular clusters to be directly observed for the first time.

1.3 Outline of the Thesis

This thesis describes the results of several projects aimed at characterizing the properties of the very low mass (VLM) stars in the halo. Each chapter has been written as a separate paper suitable for publication.

In Chapter 2, we introduce a classification system for M subdwarfs that allows the metallicity of star to be easily assessed. We use model atmospheres to determine the metallicity that applies to each class. Comparison to globular clusters and stellar models allow us to conclude that these metallicities are very likely correct. This chapter has appeared in the Astronomical Journal (Gizis 1997).

In Chapter 3, we confirm the Chapter 2 results by directly comparing our M subdwarf analysis to FGK subdwarfs analyzed by Carney et al. (1996). This chapter is in press at the Publications of the Astronomical Society of the Pacific (Gizis & Reid 1997).

In Chapter 4, we estimate the first temperature scale for M subdwarfs using optical spectrophotometry and broad-band optical and infrared photometry.

In Chapter 5, we turn to magnetic activity in metal-poor VLM stars. Activity has been linked to rapid rotation in disk stars — but this activity causes a decrease in rotation rate. We study two M subdwarf systems which have retained rapid rotation and high activity due to the presence of very close companions. Our results suggest that rapidly rotating metal-poor M subdwarfs cannot maintain as high activity levels as are seen in young, isolated M dwarfs in nearby open clusters. This chapter has been submitted to the Astronomical Journal (Gizis 1998).

In Chapter 6, we present the results from a proper-motion survey aimed at identifying low-luminosity halo stars. This is used to estimate the space density of the VLM component of the halo. We have combined those data with previous observations of the brighter, higher-mass halo stars to determine the halo luminosity function. This study also provides a measurement of the kinematics of the very low mass halo component.

Bibliography

Adams, 1915, ApJ, 42, 172

Ake, T.B., & Greenstein, J.L. 1980, ApJ, 240, 859

Allard, F., & Hauschildt, P.H. 1995, ApJ, 445, 433

Baade, W. 1944, ApJ, 100, 137

Bahcall, J.N., Schmidt, M., & Soneira, R.M. 1983, ApJ, 265, 730

Carney, B.W., Laird, J.B., Latham, D.W., & Aguilar, L.A. 1996, AJ, 112, 668

Chamberlain, J.W., & Aller, L.H. 1951, ApJ, 114, 52

Eggen, O.J., Lynden-Bell, D., & Sandage, A. 1962, ApJ, 136, 748 (ELS)

Gizis, J.E. 1997, AJ, 113, 806 (Chapter 2)

Gizis, J.E. 1998, AJ, submitted (Chapter 5)

Gizis, J.E., & Reid, I.N. 1997, PASP, in press (Chapter 3)

Gratton, R.G., Fusi Pecci, F., Carretta, E., Clementini, G., Corsi, C.E., and Lattanzi, M. 1997, ApJ, submitted

Hartwick, F.D.A., Cowley, A.P., & Mould, J.R. 1984, ApJ, 286, 269

Joy, A.H. 1947, ApJ, 105, 96

Kuiper, G.P. 1948, AJ, 53, 194

Layden, A.C., Hanson, R.B., Hawley, S.L., Hlemola, A.R., & Hanley, C.J. 1996, AJ, 112, 2110

Luyten, W.J. 1979, Catalogue of stars with proper motions exceeding 0".5 annually (LHS), (University of Minnesota, Minneapolis, Minnesota)

Majewski, S.R. 1993, ARAA, 31, 575

Norris, J. 1986, ApJS, 61, 667

Norris, J.E. 1994, ApJ, 431, 645

Reid, I.N., & Majewski, S.R. 1993, ApJ, 409, 635

Reid, I.N., & Gizis, J.E. 1997, AJ, 113, 2246

Reid, I.N., Gizis, J.E., Cohen, J.G., Pahre, M.A., Hogg, D.W., Cowie, L., Hu, E., &

Songaila, A. 1997, PASP, 109, 559

Reid, I.N., Yan, L., Majewski, S., Thompson, I., Smail, I. 1996, AJ, 112, 1472

Reid, M.J. 1993, ARAA, 31, 345

Reid, I.N. 1997a, AJ, 114, 161

Roman, N.G. 1954, AJ, 59, 307

Salpeter, E.E. 1955, ApJ, 121, 161

Schmidt, M. 1975, ApJ, 202, 22

Searle, L., & Zinn, R. 1978, ApJ, 225, 357 (SZ)

VandenBerg, D.A., Bolte, M., Stetson, P.B. 1996, ARAA, 34, 461

Chapter 2 M Subdwarfs: Spectroscopic Classification and the Metallicity Scale

Abstract

We present a spectroscopic classification system for M dwarfs and M subdwarfs based on quantitative measures of TiO and CaH features in the region $\lambda\lambda 6200-7400$Å. Our sample of cool stars covers the range from solar metallicity stars to the most extreme subdwarfs known. Using synthetic spectra computed by Allard and Hauschildt (1995), we derive metallicities for the stars. Stars are classified as dwarfs (M V), subdwarfs (sdM), or extreme subdwarfs (esdM). These classifications correspond to $[m/H] \approx$ 0.0, -1.2, and -2.0 respectively. Our metallicity scale agrees with theoretical HR diagrams and HST globular cluster measurements. We discuss some nearby subdwarfs of particular interest in light of our metallicity scale.

2.1 Introduction

The vast majority of stars are M dwarfs, main sequence stars whose spectra are dominated by molecular absorption. They have lifetimes much greater than the age of the universe which makes them an important fossil record of Galactic history. Their potential is largely unrealized because investigations of their properties have been hampered by the complex absorption spectra of diatomic and triatomic molecules. In particular, theoretical model atmospheres face serious difficulties; as a result, traditional methods of determining abundances from high resolution spectra of weak atomic lines are inapplicable, requiring the use of other techniques.

A fundamental astronomical tool is a classification system that spans the range of observed properties, allowing an estimate of the effective temperature (T_{eff}), lu-

minosity, and abundance ($[m/H]$) from a spectrum by comparison to standard stars with known properties. The system also should also allow identification of rare objects with unusual properties. The MKK dwarf spectral sequence (Morgan et al. 1943) extended to M2 V and only included Population I objects. As progressively cooler stars have been discovered the classification system has been extended to M6.5 by Boeshaar (1976) and M9 (Kirkpatrick et al. 1991, hereafter KHM; see also Bessell 1991). The KHM system uses features in the wavelength ranges $\lambda\lambda 6950 - 7500$Å and $\lambda\lambda 8400 - 8950$Å observed at $\sim$ 18Å resolution or better, and Henry et al. (1994, hereafter HKS) have applied it to cool stars within 8 parsecs. A slightly different approach was taken by Reid et al. (1995, hereafter RHG) and Hawley et al. (1996, hereafter HGR) who used measurements of the 7100 TiO bandhead at higher resolution ($\sim$ 3Å) to classify most of the known M dwarfs within 25 parsecs. The standards from KHM and HKS were used to place the RHG observations on the standard system.

The spectral classification system is thus now well-defined for the near solar abundance M dwarfs of the Galactic Disk. The situation for low metallicity stars, traditionally called subdwarfs, is much more confused. Although many spectra of individual stars have been published, there is no consistent M subdwarf classification system. Examples of metal-poor M subdwarfs were spectroscopically identified as long ago as Joy (1947), although "later investigators had difficulty in recognizing his criteria" (Oort 1965). Mould and McElroy (1978) discussed "old disk subdwarfs" which were less metal poor than other subdwarfs on the basis of TiO and CaH indices. Ake and Greenstein (1980), following a spectroscopic survey of high velocity stars, published spectra of four "extreme subdwarf M stars" which appeared to have "extreme metal deficiency" compared to the usually recognized M subdwarfs. Similar stars were identified spectroscopically in a search for nearby white dwarfs (Liebert et al. 1979), a search for Population II halo stars (Hartwick et al. 1984), and a survey of cool M dwarfs (Bessell 1982), all targeted at faint, high-proper motions stars. Recently, trigonometric parallaxes of 17 extreme subdwarfs have been measured, confirming their subluminosity (Monet et al. 1992, hereafter M92). Thus objects selected by different criteria can be called subdwarfs by different authors. M92 also found that there

is a gap between their extreme subdwarf sequence and the "less extreme" subdwarf and disk sequence in the M_V vs. V-I HR diagram – their preliminary interpretation was that this gap represented a real lack of "intermediate" metallicity stars. In any case, the physical properties of the various subdwarf types remain in doubt; for example, M92 argue that their extreme subdwarfs have $[m/H] \sim -1.7$ whereas Eggen (1996) suggests they have $[m/H] \sim -2.5$ to -3.5.

Here we present a self-consistent set of spectroscopic observations of cool metal-poor stars drawn from a variety of sources. Selection of our subdwarf candidates and the data reduction procedures are discussed in Section 2.2. In Section 2.3, we discuss empirical molecular bandstrengths and suggest a two-dimensional classification system. In Section 2.4, we compare our spectra to model atmospheres and deduce metallicities. In Section 2.5, we discuss the use of color-color and HR diagrams. Some notable individual stars are discussed in Section 2.6. The results are summarized in Section 2.7.

2.2 Observations

2.2.1 Sample Selection

Identification of a metal-poor or halo population can be difficult and ambiguous. It is well known from studies of hotter (F, G, and K) stars that there is no one-to-one correspondence between kinematics and metallicity because there is overlap between the properties of the disk and halo components (e.g., Mihalas and Binney 1981). Even among local stars with $v_{tan} > 100$ km s^{-1}, the halo (Population II) is outnumbered approximately ten to one (Schmidt 1975) by high velocity, slightly metal-poor disk stars (the Intermediate Population II, reviewed by Majewski 1993). Despite the name Intermediate Population II (IPII), these stars have a mean metallicity ($[m/H] \sim -0.6$) close to that of the disk ($[m/H] \sim 0.0$), although the exact abundance distribution of the IPII is difficult to determine (Carney et al. 1989). In contrast, a conservatively selected field halo sample (Laird et al. 1988) (restricted to stars that have $v_{tan} >$

220 km s^{-1} or $V < -220$ km s^{-1} [1]) has a distribution in $[m/H]$ that peaks at -1.7 with FWHM $\sim$ 1.2 dex, and includes tails that extend down to very low abundances (8% of the stars have $[m/H] < -2.5$) and up to IPII-like abundances (9% have $[m/H] > -1.0$). We therefore *a priori* expect that kinematically selected samples with loose selection criteria (e.g., $v_{tan} > 100$ km s^{-1}) will include many IPII stars that have $[m/H] > -1$, and we also expect to see a large range of metallicities even among "true" halo stars.

We have chosen our objects from a number of sources; however, virtually all have been identified in proper motion surveys and appear in the Luyten LHS catalog (Luyten 1979) and most are in the the Lowell Proper Motion Survey (Giclas et al. 1971). These surveys give proper motions, photographic magnitudes, and low-precision color indices which are by themselves not adequate to isolate a halo or metal-poor sample. However, many late-type candidate subdwarfs have been identified in followup surveys. Since we use a variety of sources, selection criteria are ill-defined but typically depend on the star's velocity, color, or spectral features. We particularly favor stars with measured trigonometric parallaxes. These effects are not important for this work since we are not setting out to measure statistical quantities. Of particular note are the Schmidt (1975) complete sample of stars with $\mu > 1.295''$ yr^{-1} and $m_{pg} < 15.95$, the Greenstein (1989) sample of cool halo stars, and the M92 and Ruiz and Anguita (1993, hereafter RA) samples of CCD parallax stars. Other objects have been chosen from lists of unusual stars in photometric followups (Dawson and Forbes 1989; Dawson and Forbes 1992; Reid 1982; Leggett 1992) Finally, it should noted that the Giclas catalog only goes to $m_{pg} \sim 17$ and is incomplete for $m_{pg} \geq 16$. Schmidt (1975) showed that the apparent lack of $M_{pg} > 13.5$ ($M_V \sim 12$) is due to this apparent magnitude limit. The Luyten searches reach $m_R \sim 20$ but are incomplete both for $m_R > 18$ and $\mu > 2.5''$/yr (Dawson 1986). The latter limit implies that stars with typical halo tangential velocities of 220 and 300 km s^{-1} would not have been detected within 18 and 25 parsecs respectively.

[1] We use the standard notation of (U,V,W) for the space velocity components; note that U is positive towards the Galactic Center ($l = 0, b = 0$).

In addition to the candidate subdwarfs selected above, we have utilized the RHG observations of 1700 M dwarfs from the preliminary Third Catalog of Nearby Stars (Gliese and Jahreiss 1991, CNS3) as a reference solar abundance sample. We note particular use of two subsets from this sample. First, we use the stars within eight parsecs, selected to be either single or well separated from their companions, which outline the detailed structure in the HR diagram (e.g., Gizis and Reid 1996). Distances were adopted from RHG, but the stars were required to have accurate trigonometric parallaxes with Lutz-Kelker (1973) corrections less than 0.1 magnitudes. Second, we also use the nearby stars with $v_{tan} > 100$ km s^{-1}.

2.2.2 Spectroscopic Observations and Data Reduction

Spectra were obtained at the Palomar 60 in. telescope, the Hale 200 in. telescope, and the Las Campanas Du Pont 100 in. telescope. We used the G-mode of the Palomar 60 in. spectrograph (McCarthy 1985), a 1 arcsecond slit, and a 600 l/mm grating blazed at 6500Å, yielding 1.5 Å pix^{-1}. Candidate subdwarfs were observed in May 1994, September 1994, and January 1996 while some CNS3 stars were observed with the same setup in 1993 and 1994 (RHG). At the Hale 200 in. telescope we used the double spectrograph. In August 1995, the blue camera was set to observe $6000 - 6900$Å and the red camera was set to $6700 - 8000$Å using 600 l/mm gratings blazed at 4000Å and 10000Å respectively. In October 1995, a new red camera was installed in the double spectrograph, which we used in all subsequent runs to observe the region $\lambda 6000 - 7400$Å at 1.4 Å pix^{-1}. The 100 in. telescope observations used the modular spectrograph with a 1200 line grating blazed at 7500Å. The resolution at all telescopes was $3 - 4$Å. At all telescopes, neon and argon arcs were taken after each observation in order to eliminate the effects of instrument flexure. The data were extracted, sky subtracted, and wavelength calibrated using the FIGARO package. Flux standards (Gunn and Oke 1983 and Baldwin and Stone 1984) were used to set the data on an F_ν scale. Since observing conditions were usually non-photometric with seeing worse than 1 arcsecond, the fluxes are not absolute.

Radial velocities were measured using the FIGARO cross correlation task SCROSS and corrected to a heliocentric frame using VHELIO. M dwarf radial velocity standards were drawn from Marcy and Benitz (1989). For the Hale 200 in. telescope observations, the extreme subdwarf LHS 1174 was also used as a cross correlation standard. A radial velocity of -112 ± 2 km s^{-1} was adopted based upon a Keck HIRES spectrum (Reid, personal communication). Using either the extreme subdwarf or disk M dwarfs did not make a significant change in the derived velocities, which have an uncertainty of $\pm \sim 20$ km s^{-1}. We have 14 stars in common with the more precise measurements of Dawson and De Robertis (1988, 1989) – we find a mean difference of 10 km s^{-1} and a standard deviation of 26 km s^{-1}. The three stars with differences of more than 30 km s^{-1} are LHS 161, 205a, and 479.

2.3 Bandstrengths and a Subdwarf Spectroscopic Sequence

Molecular features are typically very broad (tens or hundreds of Angstroms) and often are asymmetric. In M dwarfs, there are few points that are relatively clear of absorption, but model atmospheres (Allard and Hauschildt 1995) show that even these are depressed from the "true" continuum. Since absolute measurements of the strength of features are therefore impossible, we instead measure molecular features with bandstrength indices defined as

$$R_{ind} = \frac{F_W}{F_{cont}}$$

where pseudo-continuum (F_{cont}) region and the feature (F_W) wavelength limits are taken from RHG and listed here in Table 2.7. In the case of the CaH1 index, two sidebands are used to estimate the pseudo-continuum flux (S_1 and S_2). As in RHG, the spectral indices have an accuracy of $\pm 0.02 - 0.04$. Note that our experience with these indices show that all except CaH2, which uses widely separated pseudo-continuum and feature regions, are insensitive to the flux calibration errors. CaH2

shows systematic offsets of up to 0.03 from observing run to observing run. The measured indices for our stars are given in Table 2.2.

The KHM M dwarf spectral types provide an excellent shorthand description of the spectral properties of Galactic Disk stars – we find that over the range K7 - M6 the relations

$$Sp = -9.64 \times \mathrm{TiO5} + 7.76 \tag{2.1}$$

$$Sp = 7.91 \times \mathrm{CaH2}^2 - 20.63 \times \mathrm{CaH2} + 10.71 \tag{2.2}$$

$$Sp = -18.00 \times \mathrm{CaH3} + 15.80 \tag{2.3}$$

are accurate to ± 0.5 subclass, where K5 and K7 are $Sp = -2$ and -1 respectively. As described by RHG, the CaH1 index saturates at $\sim M3$, beyond which it does not show much temperature dependence. Although TiO5 was used by RHG to classify the stars, the two CaH relations are equally good spectral type indicators for near solar metallicity stars.

Figure 2.1 shows the three CaH indices plotted against TiO5 for our candidate metal-poor stars and the eight parsec disk sample. [2] Fifty stars lie significantly below the mean CaH vs TiO5 relations, a significant difference compared with only 5 of 1685 stars in RHG. There appears to be a fairly well defined sequence to the lower right of each figure – in Figure 2.1b a high-order polynomial illustrates the cutoff adopted. We will call the stars below this cutoff the extreme M subdwarfs. Note however that the region between the extreme M subdwarf sequence and the disk M dwarfs is well represented in our sample.

The extreme subdwarf sequence, with the notable exception of LHS 453, has very weak but detectable TiO absorption at the resolution of our observations. However,

[2]The relations defined by all of the M dwarfs in the northern CNS3 are plotted in RHG's Figure 4.

even the coolest star, LHS 1742a ($M_V = 14.43$), has only the TiO strength of a disk M1 star – the rest of the sequence is equivalent to K7 or K5 stars according to equation 2.1. Indeed, LHS 1174 was classified "sdK7-M1" by Liebert (1991, personal communication reported in M92). A TiO classification thus compresses the entire sequence of M subdwarfs into only three subclasses even though Figure 2.1 shows there is as much or more variation in the CaH strengths as TiO variation in the disk M dwarfs. Use of equations 2.2 or 2.3 gives spectral types of M5.5 (CaH2) or M8 (CaH3, extrapolated) for LHS 1742a.

In many circumstances a simplified shorthand notation may be more useful than measurements of specific molecular features, even though Figure 2.1 shows that there is a full two-dimensional continuum in the properties of M subdwarfs. Using the TiO and CaH indices as a guide, a sequence of low abundance M spectral standards can be defined. While this is the first subdwarf standard sequence to be defined, historical precedent supports using the prefix "sd"before the M spectral class. (Luminosity class VI should not be used for subdwarfs according to Jaschek and Jaschek 1987.) In the past, LHS 64 has been classified sdM1 (Joy 1947), very similar to the "sdK7-M1" classification for LHS 1174. Unfortunately the use of "sd" alone throws away much information – although both types of subdwarfs above are significantly different from Population I stars, they also differ at least as much from each other, as seen in Table 2.2 and Figure 2.1. Second, as discussed above, use of TiO alone would artificially suppress much of the variance among the extreme subdwarfs.

We therefore propose the following classification system, which consists of both a prefix (M, sdM, esdM) and a numerical subclass. The classification system works as follows. First, determine if the star if a subdwarf of some kind using CaH1. Second, use CaH2 to determine if the star is a sdM or esdM. Finally, assign a numerical subclass. Each step is described in detail below.

In the first step, stars that show significantly stronger CaH absorption for their TiO5 strength compared with disk dwarfs are designed subdwarfs with the prefix "sdM" or "esdM". Quantitatively, we define significant as lying 0.07 below the mean Population I CaH1-TiO5 relation of the RHG stars. If the other indices are unavail-

able, 0.06 below the RHG CaH2-TiO5 or CaH3-TiO5 relations is equivalent. For the coolest stars ($TiO5 < 0.49$), CaH2 or CaH3 must be used since the disk CaH1 relation is "saturated." The equations for these cutoffs are:

$$\mathrm{CaH1} < 0.695 \times \mathrm{TiO5}^3 - 0.818 \times \mathrm{TiO5}^2 + 0.413 \times \mathrm{TiO5} + 0.651 \qquad (2.4)$$

$$\mathrm{CaH2} < 0.968 \times \mathrm{TiO5}^3 - 1.358 \times \mathrm{TiO5}^2 + 1.315 \times \mathrm{TiO5} - 0.033 \qquad (2.5)$$

$$\mathrm{CaH3} < 0.639 \times \mathrm{TiO5}^3 - 1.199 \times \mathrm{TiO5}^2 + 1.161 \times \mathrm{TiO5} + 0.307 \qquad (2.6)$$

Stars that fulfill Equations 2.4, 2.5, or 2.6 are either sdM or esdM. Equation 2.4 is plotted in Figure 2.1a. In the second step, the extreme subdwarfs are identified. A high order polynomial, shown in Figure 2.1b, was used to interpolate between arbitrarily chosen points to define a cutoff in CaH2 vs. TiO5. The coordinates of the points, expressed as (TiO5,CaH2), are (0.0,-0.1), (0.433,0.234), (0.600,0.303), (0.800,0.456),(0.905,0.626), (0.977,0.788), and (1.020,0.914). The sdM lie above these points and the esdM lie below. The separation between the subdwarfs and extreme subdwarfs is natural (at least for this sample) for the M stars, but at the hotter end the weakness of the features makes the sequences merge. At the cool end, the relation is not defined beyond TiO5 $\sim$ 0.6, but the points given prevent the interpolating polynomial from inconveniently crossing the disk sequence.

Finally, the numerical subclass is determined. The definition of the numerical subclasses is problematic. Larger numbers correspond to lower temperatures, but since effective temperatures are not well determined for cool stars it is impossible to ensure that sdM subclasses correspond to the same temperatures as M V stars or esdM stars. Some authors (e.g., Hamilton and Stauffer 1993) have used pseudocontinuum indices to assign types for late-type disk M dwarfs, but we find that the pseudocontinuum points available in our spectral range show more scatter than the bandstrength indices we are using. We adopt Equation 2.2 as the definition of numerical subclasses for the

sdM and esdM because this feature shows the same range ($0.2 \lesssim$ CaH2 $\lesssim 1.0$) for all metallicities. Use of the disk relation for the CaH3 feature (Equation 2.3) or the TiO5 feature (Equation 2.1) leads to very large and very small ranges in the spectral type for the esdM. The subclass, however, is relatively uncertain when using only the CaH2 feature since the spectral type determination then depends upon only a single feature. We have therefore determined the following linear fits:

$$Sp_{\rm sdM} = -16.02 \times {\rm CaH3} + 13.78 \tag{2.7}$$

$$Sp_{\rm esdM} = -13.47 \times {\rm CaH3} + 11.50 \tag{2.8}$$

The numerical subclasses listed in Table 2.2 are the average of the CaH2 relation (Equation 2.2) and the appropriate CaH3 relation (Equation 2.3, 2.7, or 2.8). We continue to classify stars as "sd" or "esd" as early as K7. For earlier stars, we assign classes of only sdK (or sdG for stars with strong $H\alpha$ absorption). The cooler sdK can be distinguished in Figure 2.1 where they have stronger CaH1 relative to the K stars presented in RHG. These features are quite weak so the measurement errors are more important. The classifications of the K stars are therefore not as certain and should be regarded with caution – they are presented here to show the continuity with the M subdwarfs. The new classifications are listed in Table 2.2. Figures 2.2 and 2.3 show sequences of spectra for the subdwarfs and extreme subdwarfs respectively.

The cool ends of the sequences are not yet well-defined, since there are as yet observations of only a few very cool spectroscopic subdwarfs. LHS 407 has been classified as sdM5.0. Although in Figure 2.1 it is well to the left of the esdM, it lies with the extreme subdwarfs in Figure 2.4 and the HR diagram (Figure 2.7). It is easily distinguished from LHS 1742a (esdM5.5), which is at present the coolest extreme subdwarf known. LHS 3061 is similar enough to LHS 1742a to also be esdM5.5, but it is slightly hotter according to its spectral indices and M92 V-I color ($\Delta_{V-I} = 0.13$). LHS 3409, observed by RHG, is apparently more metal-rich than

LHS 407, yet its indices are significantly different from the Population I, or even most stars with velocities typical of the IPII. We have therefore called it sdM4.5. LHS 3480 is a similar star. A considerably redder sdM is the star LHS 377 (shown by M92 to have $M_V = 15.66$). Its TiO5 index is equivalent to an M5.5 V star, but CaH2 gives the classification sdM7 (M92 report that Boeshaar and Liebert call the star sdM5 in a private communication). Finally, we have also observed TVLM 832-42500 which is subluminous in the I-K vs M_K diagram, which suggests it has $[m/H] \sim -0.5$ to -1.0 (Tinney et al. 1995). It is at spectral type $\sim$ M7 V where the indices break down; however, compared to the RHG stars of similar TiO5 strength it has slightly stronger CaH2 and CaH3, suggesting it is indeed slightly more metal poor, or at least spectroscopically different. Its TiO5 and CaH2 absorption is slightly stronger than LHS 377 but the CaH3 absorption is much weaker. It thus appears to be more metal rich than LHS 377. A proper understanding of the distinction between cool sdM vs. esdM will require identification of more very cool stars from the LHS catalog. However, since we determine the M spectral subclass by the quantitative CaH2 index, the classification of M4.5 and M5.5 for the stars above is well-defined in our system.

The relative strengths of bandstrength indices contains more information than just a simple classification. HGR show that there are systematic differences in the TiO indices of dMe and dM stars. In Figure 2.4, we plot the ratio CaH3/CaH2 as a function of CaH2 strength for all the RHG stars and for the sdM and esdM. The sdM tend to lie below the Population I sequence. The extreme M subdwarfs lie systematically well below the sequence. The trend is that the first band of CaH (CaH3) is stronger relative to the entire bandhead (CaH2) – similar to the behavior seen in TiO for late type M dwarfs. Since the deeper band must reflect conditions higher in the atmosphere, the difference might be caused by a slight surface gravity difference and/or a lower temperature in the CaH3 formation region compared to sdM and dM. Detailed modeling is necessary to understand this difference.

2.4 Model Atmosphere Fitting

Interpretation of the observed spectra in terms of the physical parameters effective temperature (T_{eff}) and metallicity ($[m/H]$) requires the use of model atmospheres. In principle, surface gravity is also a relevant parameter; however, both theory and observations indicate dwarf stars have $\log g \sim 5.0 \pm 0.2$ (Leggett et al. 1996) and we therefore restrict analysis to $\log g = 5.0$ models. We use the Extended Model grid computed by Allard and Hauschildt (1995, hereafter AH) which assumes local thermodynamic equilibrium (LTE).

The theoretical uncertainties and limitations of the atmosphere models have been extensively discussed by AH. Although there are uncertainties in the appropriate treatment of the physics such as non-LTE effects, the treatment of molecular opacities (usually the Just Overlapping Line Approximation is used in these models), and the treatment of convection, the primary limitation is simply the lack of both laboratory data and theoretical computations of the electronic band oscillator strengths. In particular, no data exist for the CaH molecule which is extremely important in our spectral region. In Figure 2.5, we show a synthetic spectrum based upon a solar metallicity model and a representative disk star, the KHM M 4.0 V standard Gl 402. (The treatment of the TiO molecule in solar metallicity models has recently been improved by Allard and Hauschildt in the "NextGen" model). The spectra are in good general agreement, although the specific strengths of the molecular features are incorrect, as expected. In particular, the CaH feature at $\sim$ 6950Å is too strong in all models compared to the observed spectra. However, AH show that their models capture the general overall behavior of metal-poor stars – with decreasing metallicity the hydride bands and atomic lines both increase in strength – the latter due to an increase in gas pressure.

Figures 2.2 and 2.3 clearly show the expected increase in the atomic line strength with increasing hydride strength. Until accurate data or calculations are available for all the important molecules, but especially the hydride bands, any comparison between observations and theory will remain uncertain. Since such information is not

likely to be available for many years, the uncertainties of this study will not reduced in the near future. Other authors have compared the AH models to cool solar abundance and metal-poor dwarfs using broad band colors and low-resolution optical and infrared spectra (Dahn et al. 1995; Leggett et al. 1996) or higher resolution infrared spectra (Jones et al. 1996). Our study is most sensitive to variations in CaH and TiO which dominate our more limited wavelength region. It should also be noted that the metal poor models are computed assuming scaled solar abundances. If $[O/C]$ is enhanced in the Population II M subdwarfs, as it is in hotter Population II stars, it will affect the strength of TiO and H_2O absorption (Mould 1976).

Due to the uncertainties in the molecular data, the AH models cannot be used to predict the bandstrengths measured in Section 2.3, nor are they able to reproduce the CaH3/CaH2 relation in Figure 2.4. Instead, we compare the spectral region ($\lambda\lambda 6200-7300$) by minimizing the least squares difference (χ^2) between the observed spectrum and the models. We first shift the observations to rest velocity and vacuum wavelengths, convert to F_λ, and rebin to 2Å steps. The models are convolved with a $\sigma = 2$Å Gaussian to approximate the instrumental resolution (in practice, this has negligible effects since the synthetic spectra often show 50Å wide "features" due to the computation technique). The extended models have been computed for steps of 0.5 dex in metallicity between $[m/H] = 0.0$ and $[m/H] = -4.0$. We consider $100K$ steps for the temperature range $2500K \leq T_{eff} \leq 4000K$ (higher temperatures are not available and lower temperatures are irrelevant to the stars under consideration here). For temperatures that were not calculated (T_{eff} = 2600, 3100, 3400, 3600, 3800, and 3900 K), we approximate the synthetic spectra by linearly interpolating between the two nearest temperatures.

The best fit model parameters for the subdwarf candidates are listed in Table 2.7. We have also fit the eight parsec sample of single disk M dwarfs; below 3800 K, the spectra are best matched by solar metallicity models, as expected. Above 3800 K, the fits are poor because the molecular features are too weak to constrain the fits well. We therefore report only those fits with $T_{eff} < 3800$ K. The uncertainties from the fitting procedure are the grid spacing of ± 0.5 in $[m/H]$ and ± 100 K in T_{eff}. The systematic

uncertainties are unknown, but are dominated by the errors in the synthetic spectra discussed above. We note that different temperature scales for the disk M dwarfs have historically had systematic differences of up to 300 K (e.g., Leggett et al. 1996) and our fits are subject to all the same uncertainties. Compared to Leggett et al. (1996), our fits give somewhat higher temperatures (ΔT_{eff} = 150K for LHS 377, ΔT_{eff} = 400 K for LHS 57).

The extreme subdwarfs have best fits at $[m/H] \sim -2$. Figure 2.6 shows one representative fit. The coolest extreme subdwarf, LHS 1742a, has an effective temperature of 3300 K. A difference of one extreme subdwarf spectral subclass derived from CaH2 corresponds to an approximately 100 K difference in temperature. Some authors (e.g., Eggen 1996) have argued that the the extreme subdwarfs are likely to have $[m/H] = -2.5$ to -3.0, whereas our least-squares fitting of model atmospheres gives metallicities a factor of 10 higher. The model atmospheres show that the most obvious qualitative difference is that $\sim$ 7100Å TiO features for the -2.5 and -3.0 models should be completely absent. The observed spectra, however, show that although the feature is weak it does exist in our extreme subdwarfs (except LHS 453), supporting the model atmosphere fits. LHS 453 completely lacks the TiO5 feature (the TiO feature at 6200Å is also missing) and therefore is more metal poor than the other esdM. The best fit is $[m/H] = -2.5$. For higher metallicities ($[m/H] = -1.0$) the TiO feature remains strong which is qualitatively seen in the stars classified sdM. Indeed, the sdM have best $[m/H]$ fits of -1.0 to -1.5. For the stars that were not classified subdwarfs, the model fits give $[m/H]$ of 0.0 to -1.0.

In summary, the spectroscopic classification system of Section 2.3 can be used to derive metallicities based upon our fits to AH synthetic spectra. Stars classified as extreme M subdwarfs (esdM) have $[m/H]$ of -2.0 ± -0.5, whereas sdM have a metallicity of -1.2 ± 0.3. Stars that do not show significant differences from the RHG disk sample in their CaH indices have $[m/H] > -1.0$. When model atmospheres are able to accurately reproduce the CaH and TiO bandheads more accurate metallicities should be possible.

2.5 HR diagrams

HR diagrams are an important tool for the study of cool stars. Observational HR diagrams are a critical test of stellar structure theory, provided that the transformation between theoretical temperatures and luminosities and observed quantities (colors and absolute magnitudes) can be made. In practice there has been disagreement over the Population I temperature scale (Leggett et al. 1996) and relatively little discussion of the temperature of Population II subdwarfs. The HR diagram can also be used to predict absolute magnitude from observed color and thus is used in interpretation of star count data and derivation of the luminosity function. Finally, derivation of the mass function from the luminosity function of metal-poor stars depends upon the quality of the theoretical mass-luminosity relations and evolutionary tracks since there are no cool Population II binaries with mass determinations.

Table 2.7 lists optical photometry and trigonometric parallaxes from the literature for the stars in our sample. We have adopted the Cousins R and I system and where necessary have used the color transformations compiled by Leggett (1992). Because the photometry is from heterogeneous sources of varying quality, in some cases the colors may be incorrect by as much as 0.1 magnitudes but the typical accuracy should be about 5% (Leggett 1992). In addition, the transformations have been derived for near solar metallicity stars and may be inaccurate for subdwarfs. Absolute parallaxes were taken from the preliminary Yale Parallax Catalog (van Altena et al.1991) when available. In the case of the CCD relative parallaxes reported by RA, we added a correction of 0.5 milliarcseconds to the parallaxes to transform them to absolute measurements. This approximately matches the correction applied by M92 for similar magnitude stars and the uncertainty in this correction is much less than the uncertainties in the relative parallaxes. Although the measured parallax is the best estimator of the distance to any particular star, there is a statistical bias to underestimate the distance and hence underestimate the the mean luminosity of the sample stars. Lutz and Kelker (1973) derived statistical corrections to the observed absolute magnitudes as a function of σ/π and showed that only parallaxes with $\sigma/\pi < 0.2$

are useful. However, selecting the stars by proper motion reduces the statistical correction (Hansen 1979). Since the selection of our sample is not well-defined, we do not apply any statistical correction to the absolute magnitudes, but we list the Lutz-Kelker corrections (derived from the approximation given by Hansen 1979 and defined as $M_{true} = M_{obs} + \Delta_{LK}$) as a guide to likely biases in the sample. The V-I, M_V diagram is shown in Figure 2.7. The eight parsec single stars are plotted with Lutz-Kelker corrections applied, but the sample is restricted to stars with corrections less than 0.1 magnitude. We also plot the B-V version of this diagram in Figure 2.8, including the bluer K subdwarfs in the sample and the disk G and K dwarfs within eight parsecs from the CNS3. It is well known that B-V colors are poorly suited for estimating absolute magnitudes for the disk M dwarfs (in the disk sequence M_V changes by 4 magnitudes in the range $1.4 < \mathrm{B} - \mathrm{V} < 1.6$.) In our diagram, the sdM and esdM sequences cross the disk sequence at B-V $\sim$ 1.5, and the reddest sdM and esdM actually lie above the disk sequence for B-V > 1.65.

Optical and near-infrared color-color diagrams for M dwarfs have recently been extensively discussed by Leggett (1992). In Figure 2.9 we show the V-I vs. B-V diagram for the objects we have classified. The well-known tendency for metal-poor M subdwarfs to have redder B-V at a given V-I (e.g., Mould and McElroy 1978; Dahn et al. 1995) is clearly evident, for $V - I > 1.7$. The offset appears to be strongly related to metallicity, as the esdM are approximately 0.3 magnitudes redder than the disk stars in B-V with our sdM lying in between the two sequences. A V-I vs. B-V diagram is therefore useful in identifying red subdwarfs and extreme subdwarfs. However, giants also lie redwards in B-V at a given V-I (Weistrop 1977). Indeed, Reid (1982) suggested on the basis of optical (BVRI) colors that Sm 183 might be a subdwarf similar to Kapteyn's star, but also noted the possibility that it could be a giant. In our spectrum, the CaH indices are weak compared to TiO, implying that it is a low surface gravity giant.

2.5.1 Tests of the Spectroscopic Metallicity Scale

Theoretical stellar structure models and HST globular cluster observations provide checks on our spectroscopic metallicity scale. We compare with broadband colors and magnitudes for $[m/H] = 0.0$, -0.5, and -1.5 computed with stellar interior models that use the Allard and Hauschildt model atmospheres as outer boundary conditions (Baraffe et al. 1995). The tracks are shown in Figure 2.10. Baraffe et al. (1996) did not compute $[m/H] = -1.0$ models, but they did note that for $[m/H] = -2.0$ the models are shifted blueward by ~ 0.2 magnitudes with respect to the -1.5 track. Also shown is an even more recent set of solar metallicity models computed with the latest Allard and Hauschildt NextGen models (Baraffe and Chabrier 1996). The results dramatically illustrate the importance of boundary conditions – at $0.3M_{\odot}$ (M_V = 11.31, V-I=2.19, T_{eff} = 3403), the newer model is 201 K hotter, 1.21 magnitudes brighter in M_V, and 0.63 magnitudes bluer in V-I. As a result, the newer models fail to match observations (suggesting that they would be a poor choice to use for the M_V-Mass relation). In our HR diagram, the earlier set of computations give better agreement with the Population I sequence, although none of them convincingly duplicate the structure seen. As it stands, these models support the identification of the esdM with $[m/H] \sim -1.5$ to -2.0 and the sdM as more metal poor than -0.5. Given the change of the theoretical models in less than one year, effective temperatures, metallicities, and masses derived from evolutionary models are clearly very uncertain – but the use of Allard and Hauschildt's extended model grid leads to consistent results for both spectroscopic and HR diagram metallicities.

HST photometry of a stellar cluster yields both a luminosity function and a color-magnitude diagram. Santiago et al. (1996, hereafter SEG) provide piecewise linear fits to the HR diagram of the clusters M15 ($[m/H] = -2.26$), ω Cen (-1.6), 47 Tuc (-0.6), NGC 2420 (-0.45), and NGC 2477 (0.0), which are shown in Figure 2.11 superimposed on our data (including the earlier subdwarfs). The globular cluster data reach only the brightest of the sdM and esdM. The offsets however appear to be consistent with the esdM having abundances between -1.6 and -2.26 and the sdM

between -1.6 and -0.6, as deduced for our spectroscopic analysis. SEG note that the slopes of their CMD are steeper than the nearby field parallax subdwarfs and attribute this to either calibration errors in the HST photometry or real astrophysical differences. The considerable difficulties in transforming HST magnitudes to the Cousins system are discussed by Harris et al. (1991) and Holtzman et al. (1995). In particular, the HST F606W filter includes a substantial fraction of the R_C passband. However, the differences in slope of the main sequence are less evident in Figure 2.11 than in the fits reported by SEG in the region of overlap. It appears likely that the confusion in the definition of subdwarfs led the the inclusion of progressively less metal-poor stars at redder colors in the Richer and Fahlman (1992) main sequence, in particular stars with V-I $\gtrsim 2.4$ which we argue below are Intermediate Population II ($[m/H] \sim -0.6$) and which, in any case, are clearly much fainter and redder than the stars used to define the globular cluster slopes in the HST study. The fit to the NGC 2477 lower main sequence appears to lie above the local stars – perhaps due to color terms but perhaps also because of the inclusion of binaries or non-cluster members in the fits.

Most of the cool extreme subdwarfs in this paper come from the M92 USNO CCD parallaxes. Our spectroscopic metallicity scale is in agreement with the M92 estimate that the mean $[m/H]$ of extreme subdwarfs is ~ -1.7. Some authors have disputed the argument that the extreme subdwarfs represent the "typical" halo metallicity of ~ -1.7. Richer and Fahlman (1992) argue that the extremely hot kinematics (15 of the 17 M92 extreme subdwarfs have $v_{tan} > 275$ km s^{-1} and the 5 stars with known total space velocities have $< v_{tot} >= 427$ km s^{-1}) may point to their being more metal poor than the typical Population II stars. However, since there is no metallicity-velocity relation within the higher mass stars of the Population II halo (Norris 1986) this argument seems unconvincing. Note however that the Richer and Fahlman color-magnitude relation matches our sdM at V-I ~ 1.5 but matches the disk sequence by $V - I \sim 3$, which may be appropriate for their sample since their "Population II" luminosity function is in fact dominated by the IPII at the faint end (Reid et al. 1996). Lacking a direct determination of metallicity, Eggen (1996)

estimated values of -2.5 to -3.5 for the M92 extreme subdwarfs but considered these values "guesses only."

2.5.2 Where are the Cool sdM?

M92 note that their HR diagram (their Figure 10) shows a remarkable gap between the extreme subdwarfs and the disk sequence. In their HR diagram, only one subdwarf appears between the two sequences (at about V-I of 2.2). In our sample, there is clearly a continuous distribution for stars with V-I$<$ 2.2, leaving the gap for 2.2 $<$ V-I$<$ 2.8. There are three major solutions to the gap, each of which was addressed by M92. First, the gap may be an illusion caused by stellar astrophysics – a continuous distribution in metallicity may not necessarily correspond to a simple distribution in a given observational HR diagram. Second, the gap may be due to selection effects such that stars in the gap are not chosen for parallax programs. Finally, it may represent a real lack of stars with metallicities between the disk sequence and the extreme subdwarf sequence. We will reconsider each of these options. It is certainly true that bandpass effects and the properties of cool atmospheres are important in interpreting HR diagrams. In Figure 2.8, we have seen that the behavior of the B-V HR diagram is opposite to that of the V-I diagram – at the reddest colors, the subdwarfs lie above the disk sequence, and the esdM lie above the sdM. A second example of the importance of bandpass effects is in the V-I HR diagram, where it appears that for the very coolest disk stars (LHS 2924 and 2065) V-I turns around, and becomes bluer with decreasing temperature (Bessell 1991; M92). Nevertheless, there is no evidence at present that the gap is caused by bandpass effects because M92 report the Allard model atmospheres do not produce such an effect. M92 consider that it is "very unlikely" that the gap is due to the USNO selection criteria, and therefore offer the preliminary interpretation that stars with intermediate metallicities are rare in the solar neighborhood. Since this result is quite surprising, we will next reconsider the selection effects that may entered this sample.

There necessarily were important selection effects in the catalog, since as discussed

in Section 2.2, even in a proper motion survey the majority of stars will not be extremely metal poor or halo stars. It is difficult to know exactly what the selection effects entering the catalog were, but early studies that emphasized the targets surely were influential. Some of the M92 stars were never studied before (according to SIMBAD), but others had already been noted as interesting. Two of their stars (LHS 3382 and LHS 489) were pointed out by Ake and Greenstein (1980) as being spectroscopically much more metal poor than other known subdwarfs. Liebert et al. (1979) reported "sdM" spectra for five others (LHS 192, 197, 205a, 207, and 453) from a search for nearby degenerate stars – their Figure 2 presents a noisy spectrum of LHS 205a with strong hydride bands and a lack of TiO. Four others (as well as LHS 3382 again) were chosen by Hartwick et al. (1984) for having extremely large reduced proper motions, defined as

$$H = M + 5 \log v_{tan}/4.74 = m + 5 \log \mu + 5$$

The lack of the sdM is obvious in their reduced proper motion diagram (their Figure 5). In contrast, there is no obvious gap in the reduced proper motion diagram (based on B and R magnitudes from the POSS plates) of the entire LHS catalog presented by Dawson (1986, his Figure 7). One explanation of the very large tangential velocities of the M92 sample ($< v_{tan} >= 380$ km s^{-1}) is that there was a implicit selection effect favoring large H. If so, a group of subdwarfs $\sim$ 1 magnitude more luminous but the same reduced proper motions would have $< v_{tan} >= 600$ km s^{-1}. Since this is greater than the escape velocity of the galaxy (500 km s^{-1}, Carney et al. 1988)), these subdwarfs could not enter the sample. Similarly, the (unexplained) lower limit of $v_{tan} = 275$ km s^{-1} would correspond to a lower limit of $v_{tan} = 435$ km s^{-1}. We therefore suggest that such a selection effect (as well as spectral selection of very weak TiO lines) would explain the lack of intermediate metallicity stars. As noted above, these stars are too faint to have been included in the more completely studied Giclas catalog which includes many bright early sdM. In any case, there are some likely LHS Catalog red sdM in the study of Hartwick et al. (1984) which do not yet

have parallaxes – they identified both Class H stars (e.g., LHS 192, 1970, 3259, 3382, and 3548), which we call esdM, and Class I stars (e.g., LHS 29 and 64) which we can identify as sdM stars. They found three faint class I stars: LHS 2533, 2630, and 3189. We confirm the latter as an sdM5.0 star. Further observations of these three stars would greatly increase the information available on cool sdM stars.

2.5.3 Kinematics

Using the trigonometric parallaxes in Table 2.7, the radial velocities in Table 2.2, and the LHS catalog proper motion values, we can compute the U,V,W components of galactic velocity (Table 2.7). The errors in radial velocity, $\pm \sim 20$ km s^{-1}, are comparable to the uncertainties due to the trigonometric parallax errors. The kinematics of the sample are not representative of the Population II due to the uncertain selection criteria, but they can provide some information on the selection criteria used. Mean values and standard deviations (velocity dispersions) for the spectroscopic classes are listed in Table 2.7. The sdM, with the mean velocity component $< V >= -202$ km s^{-1}, and the esdM, with a mean galactic velocity component $< V >= -287$ km s^{-1}, have clear Population II kinematics (the mean V velocity for the halo is disputed but lies between -270 and -180 km s^{-1} according to Majewski 1993). Our candidate halo stars that were classified as M V have both smaller $< V >= -134$ km s^{-1} and smaller U and V velocity dispersions – more typical of the IPII and certainly much greater than the disk ($< V >= -22$ km s^{-1}). These non-subdwarfs in fact have bandstrength indices similar to the majority of RHG nearby stars with $V_{tan} > 100$ km s^{-1}, which should be an IPII dominated sample. For both sdM and esdM, σ_U and σ_W are somewhat greater and σ_V is somewhat less than the halo values of Norris (1986) as expected for a sample selected by large velocity but excluding near solar V values. Also given in Table 2.7 are the velocity dispersions for late M dwarf RHG stars with $TiO5 < 0.4$ and either weak CaH1 (CaH1 ≥ 0.74) or strong CaH1 (CaH1 < 0.74), as well as the RHG values for nearby disk M dwarfs. The strong CaH1 stars have larger velocity dispersions, suggesting that they are older

and supporting the idea they are more metal poor – but their velocities are much less than a Population II group. Thus although CaH1 is useless as a temperature indicator for stars cooler than M3, it may prove to be a useful metallicity indicator for late-type (M4 to M6.5) disk stars, particularly if CaH features can be reproduced by future model atmospheres.

We have also computed total galactocentric velocity for the stars after correcting for the Sun's motion with respect to the Local Standard of Rest (Mihalas and Binney 1981) and assuming a LSR circular velocity of 220 km s^{-1}. All of the stars are easily bound to Galaxy – the fastest sdM (LHS 467, v_{Gal} = 342 km s^{-1}) and the fastest esdM (LHS 3548, v_{Gal} = 364 km s^{-1}; LHS 453, v_{Gal} = 451 km s^{-1}) are comfortably less than the galactic escape speed of $\sim$ 500 km s^{-1} (Carney et al. 1988).

2.6 Notes on Individual Stars

2.6.1 CM Dra (LHS 421)

CM Dra (Gl 630.1) is a short period eclipsing binary with component masses M_A = 0.2307 ± 0.0010 and M_B = $0.2136 \pm 0.0010 M_\odot$ and helium abundance Y_A = 0.32 and $Y_B = 0.31 \pm 0.04$ (Metcalfe et al. 1996). Based on the large W velocity and the observed low flaring rate and lacking a spectroscopic metallicity, Metcalfe et al. 1996 interpret the system as Population II and therefore interpret the high helium abundance as possible support for a higher primordial helium abundance. Using the observed spectrum (taken from RHG), we find that the system not very metal poor, with a best fit model of $[m/H] = 0.0$, and does not show any CaH excess compared to Population I stars; however, infrared photometry (Leggett 1992) suggests it is more metal-poor than most disk stars. We therefore conclude CM Dra formed from significantly enriched material. The CNS3 W velocity of -34 (-27 when corrected for the solar motion given in Mihalas and Binney 1981) implies that its maximum height above the plane is only $\sim$ 350 pc (Kuijken and Gilmore 1989), whereas starcounts show the true Population II does not become dominant until beyond 5 kpc (Majewski

1993), so CM Dra can probably be considered an Intermediate Population II, or even Population I, star.

2.6.2 Barnard's Star (LHS 57) and Gl 299 (LHS 35)

M92 have discussed the well-known Barnard's Star (Gl 699) extensively. It lies perhaps 1.6 magnitudes below their mean disk main sequence, yet it is well-known that spectroscopically it is an M dwarf, a result that this study confirms. We believe that the distance below the main sequence is "artificially" enhanced by the presence of the kink in the main sequence (Gizis and Reid 1996 Figure 5) which is not fit well by a line. At spectral type M4.5 the disk sequence, when restricted to only single stars with high quality parallaxes and photometry, shows a sharp 1 magnitude drop. Hence Barnard's Star is only about 0.6 magnitudes below the disk sequence. It seems likely that Barnard's Star has a metallicity between -0.5 and -1.0. It is a weak outlier in TiO and CaH. The well-known star Gl 299 (LHS 35) is quite similar in both its indices and absolute magnitude. We identify both as Intermediate Population II stars and as cool analogues to the spectroscopically unremarkable stars (e.g., LHS 301 and 376). The M4.5 V star LHS 3684 which has an M92 parallax is an only slightly cooler counterpart of Barnard's Star in both the spectroscopic indices and the HR diagram.

2.6.3 The sdMe (LHS 482 and 2497) and Unresolved Binaries

Two subdwarfs in this study show noticeable $H\alpha$ emission. Gl 781 (LHS 482) shows large radial velocity variations typical of a short period binary (Joy 1947). We have obtained echelle spectra that confirm the radial velocity variations but do not show lines from the secondary (Gizis et al.1996). We therefore have not adjusted the absolute magnitude in Table2.7 for the secondary component. Gl 455 (LHS 2497) shows weak H alpha emission (Hawley et al. 1996) and our recent echelle spectra have shown the system to be a short period double-lined spectroscopic binary (Gizis et al.1996). Since the system is near-equal luminosity we have not adjusted the color but have subtracted 0.75 from the absolute magnitude in Table 2.7. The system

is a strong outlier in Figure 2.1, yet even with the adjustment it has an absolute magnitude and color similar to the subluminous IPII dM stars. The YPC parallax is based upon two determinations with good agreement and has an uncertainty of less than 10%. If it is not in error, perhaps the chromospheric activity affects the spectrum or magnitude of this interesting system. Unfortunately we have no other examples of late sdM that is comparable to this system. Young et al. (1987) argue that M dwarf binaries with short periods ($P \lesssim 5$ days) must show emission. The observed radial velocity variations are consistent with this limit. Mass determinations would provide a important constraint on theories of metal poor low-mass stars, but the short periods imply small separations ($a \lesssim 4$ milliarcseconds) for these systems. No other sdM or esdM show $H\alpha$ emission in this study, and indeed no extreme M subdwarfs with emission are yet known.

The sdMe discussed above are the only stars in the sample known to have unresolved companions. LHS 169, also known as Gl 129 but no longer within the nearby star catalog (CNS3) due to an improved parallax, has been reported to be spectroscopic binary. Three measurements of the radial velocity (Joy 1947) found radial velocities of -139.6, -91.0 and -75.9 km s^{-1} with probable error 2.1 km s^{-1}. The radial velocity variations have evidently never been confirmed or refuted since then, and Dawson and De Robertis (1988) suggest that the Joy (1947) velocities may be incorrect for a number of subdwarfs. LHS 64 has been reported to have velocity varying between -292 and -242 by Joy (1947) but we have obtained 3 echelle spectra which are consistent with no variations at all. Lacking any further data, we do not apply any correction to the absolute magnitude of either star for any companion. Presumably at least a few of the stars in our sample have unresolved companions that are still unknown, which could affect the magnitudes or radial velocities in a few cases.

2.6.4 The Most Extreme Subdwarf: LHS 453

One important use of a classification system is identifying unusual stars. Our indices have allowed us to identify LHS 453 as even more metal poor than the other extreme

subdwarfs. We would therefore expect this star to be below the other stars in the HR diagram, but the M92 observations (V-I = 2.22, M_V = 13.08) place the star in the midst of the extreme subdwarf sequence. However, the reported mean error in M_V is still fairly large at $\pm$0.20 magnitudes. Perhaps coincidentally, this most metal poor star also has the largest galactocentric velocity in the sample, though Dawson and De Robertis (1988) showed that despite the large tangential velocity (M92 give 466.9 ± 42.8) the star is bound to the galaxy. If the parallax is indeed reduced, the tangential velocity would also be decreased. Alternatively, if LHS 453 is a binary, its M_V would be fainter by up to 0.75 magnitudes. The best fit synthetic spectrum has $[m/H] = -2.5$, but we note that the synthetic $[m/H] = -3.0$ spectrum is almost identical. Although TiO is absent, LHS 453 is not likely to be more metal poor than this because the observed atomic lines are prominent and similar in strength to those of LHS 205a (which is only slightly later type in V-I color and CaH indices). According to the models, the atomic lines should be much weaker or absent for $[m/H] = -3.5$ or -4 at all temperatures.

2.7 Conclusions

This paper presents spectroscopy of 50 late-type stars that are significantly more metal-poor than the Population I. Bandstrength indices are used to measure TiO and CaH features and show that many different metallicities can be distinguished in the Population II M stars, as expected from the metallicity spread seen in G-subdwarfs. The TiO feature at $\sim$ 7100Å is shown to put all the extreme subdwarfs into only a few spectral subclasses (K7 and M0). Instead, a CaH index which reproduces the Population I spectral classification system of Kirkpatrick, Henry, and McCarthy (1991) is used to classify stars. Based on the differences between the (weak) TiO and the CaH the metal poor M stars are divided into the simple categories of M subdwarfs (sdM) and extreme M subdwarfs (esdM) and spectral standards are presented (Figures 2.2 and 2.3).

Synthetic spectra computed by Allard and Hauschildt (1995) are fit to the ob-

served spectra. Metallicities of $[m/H] \sim -2$ are derived for the esdM and ~ -1.2 for the sdM. These estimates are in agreement with the estimates of G89 and M92 but not those of Richer and Fahlman (1992) or Eggen (1996). HR diagrams based on literature observations are presented for dM, sdM and esdM. They are at least qualitatively in agreement with theoretical computations and HST observations of globular clusters. However, the former are sensitive to the boundary conditions used and the latter are likely to suffer from large color terms. The agreement of all three methods seems to indicate the metallicity scale is accurate to ~ 0.5 dex.

Given this metallicity scale, we discuss a number of interesting subdwarfs and stars that have been called subdwarfs. The eclipsing binary system CM Dra is shown to be significantly enriched such that its composition is not likely to reflect the primordial helium abundance. The "old disk subdwarfs" such as Gl 299 and Gl 699 are probably not as subluminous as is usually thought – taking into account the detailed structure of the HR diagram, rather than simply fitting a straight line, they are only ~ 0.6 magnitudes subluminous rather than the usually cited ~ 1.2 magnitude. This naturally explains the only slight spectral differences, which are shown to be similar to differences of hotter M dwarfs that are also ~ 0.6 magnitudes subluminous. Finally, we show that LHS 453 is more metal poor than the other extreme subdwarfs with $[m/H] \sim -2.5$ to -3.

Acknowledgments

The referee, Todd Henry, provided comments which substantially improved this paper. I am indebted to France Allard and Peter Hauschildt for making their synthetic spectra available. I am grateful for Greenstein and Kingsley Fellowships and partial support through NASA grant GO-5353.0-93A. This research has made use of the Simbad database, operated at CDS, Strasbourg, France.

Bibliography

Ake, T.B., & Greenstein, J.L. 1980, ApJ, 240, 859

Allard, F., & Hauschildt, P.H. 1995, ApJ, 445, 433

Baldwin, J.A., & Stone, R.P.S. 1984, MNRAS, 206, 241

Baraffe, I., Chabrier, G., Allard, F., & Hauschildt, P.H. 1995, ApJ, 446, L35

Baraffe, I., & Chabrier, G. 1996, ApJ, 461, L51

Bessell, M.S. 1982, Proc. ASA, 4, 417

Bessell, M.S. 1990, A&AS, 83, 357

Bessell, M.S. 1991, AJ, 101, 662

Boeshaar, P.C. 1976, Ph.D. Thesis, Ohio State University

Carney, B.W., Latham, D.W., & Laird, J.B. 1988, AJ, 96, 560

Carney, B.W., Latham, D.W., & Laird, J.B. 1989, AJ, 97, 423

Dahn, C.C., Liebert, J., Harris, H.C., & Guetter, H.H. 1995, The Bottom of the Main Sequence – And Beyond, edited by C.G. Tinney (Berlin, Springer), p.239

Dawson, P.C. 1986, ApJ, 311, 984

Dawson, P.C., & De Robertis, M.M. 1988, AJ, 95, 1251

Dawson, P.C., & De Robertis, M.M. 1989, AJ, 98, 1472

Dawson, P.C., & Forbes, D. 1989, PASP, 101, 614

Dawson, P.C., & Forbes, D. 1992, AJ, 103, 2063

Eggen, O.J. 1979, ApJS, 39, 89

Eggen, O.J. 1987, AJ, 92, 379

Eggen, O.J. 1996, AJ, 111, 466

Giclas, H.L., Burnham, R., & Thomas, N.G. 1971, The Lowell Proper Motion Survey (Lowell Observatory, Flagstaff, Arizona)

Gizis, J.E., & Reid, I.N. 1996, AJ, 111, 365

Gizis, J.E., Reid, I.N., Hawley, S.L. 1996, in preparation

Gliese, W., & Jahreiss, H. 1991, Preliminary Version of the Third Catalog of Nearby

Stars (CNS3)

Greenstein, J.L. 1989, PASP, 101, 787

Gunn, J.E., & Oke, J.B. 1983, ApJ, 266, 723

Hamilton, D., & Stauffer, J.R. 1993, AJ, 105, 1855

Hanson, R.B. 1979, MNRAS, 186, 875

Harrington, R.S., & Dahn, C.C. 1980, AJ, 85, 454

Harris, H.C., Baum, W.A., Hunter, D.A., & Kreidl, T.J. 1991, AJ, 101, 677

Hartwick, F.D.A., Cowley, A.P., & Mould, J.R. 1984, ApJ, 286, 269

Hawley, S.L., Gizis, J.E., & Reid, I.N. 1996, A.J., in press

Henry, T.J., Kirkpatrick, J.D., & Simons, D.A. 1994, AJ, 108, 1437

Holtzman, J.A., et al. 1995, PASP, 107, 1065

Jaschek, C., & Jaschek, M. 1987, The Classification of Stars (Cambridge University Press, Cambridge)

Jones, H.R.A., Longmore, A.J., Allard, F., & Hauschildt, P.H. 1996, MNRAS, 280, 77

Joy, A.H. 1947, ApJ, 105, 96

Kirkpatrick, J.D., Henry, T.J., McCarthy, D.W. 1991, ApJS, 77, 417

Kuijken, K., & Gilmore, G. 1989, MNRAS, 239, 605

Laird, J.B., Rupen, M.P., Carney, B.W., Latham, D.W. 1988, AJ, 96, 1908

Leggett, S.K. 1992, ApJS, 82, 351

Leggett, S.K., Allard, F., Berriman, G., Dahn, C.C., & Hauschildt, P.H. 1996, ApJS, 104, 117

Liebert, J., Dahn, C.C., Gresham, M., Strittmatter, P.A. 1979, ApJ, 233, 226

Lutz, T.E., & Kelker, D.H. 1973, PASP, 85, 573

Luyten, W.J. 1979, Catalogue of stars with proper motions exceeding 0".5 annually (LHS), (University of Minnesota, Minneapolis, Minnesota)

Majewski, S.R. 1993, ARAA31, 575

Marcy, G.W., & Benitz, K.J. 1989, ApJ, 344, 441

McCarthy, J.K. 1985, Proc. SPIE, 554, 155

Metcalfe, T.S., Mathieu, R.D., Latham, D.W., & Torres, G. 1996, ApJ, 456, 356

Mihalas, D.M. & Binney, J. 1981, Galactic Astronomy: Structure and Kinematics, 2nd ed. (W.H. Freeman, San Francisco)

Monet, D.G., Dahn, C.C., Vrba, F.J., Harris, H.C., Pier, J.R., Luginbuhl, C.B., & Ables, H.D. 1992, AJ, 103, 638

Morgan, W.W., Keenan, P.C., & Kellman, E. 1943, An Atlas of Stellar Spectra (Chicago: Univ. of Chicago Press)

Mould, J.R. 1976, A&A, 48, 443

Mould, J.R., & McElroy, D.B. 1978, ApJ, 220, 935

Norris, J. 1986, ApJS, 61, 667

Oort, J.H. 1965, Stars and Stellar Systems V, Galactic Structure, edited by A. Blaauw & M. Schmidt (University of Chicago Press), p. 500.

Reid, I.N. 1982, MNRAS, 201, 51

Reid, I.N., Hawley, S.L., & Gizis, J.E. 1995, AJ, 110, 1838

Reid, I.N., Yan, L., Majewski, S., Thompson, I., & Smail, I.R. 1996, A.J., 112, 1472

Richer, H.B., & Fahlman, G.G. 1992, Nature, 358, 383

Ruiz, M.T., & Anguita, C. 1993, AJ, 105, 614

Ryan, S.G. 1992, AJ, 104, 1144

Santiago, B.X., Elson, R.A.W., & Gilmore, G.F. 1996, MNRAS, 281, 1363

Schmidt, M. 1975, ApJ, 202, 22

Tinney, C.G., Reid, I.N., Gizis, J., & Mould, J.R. 1995, AJ, 110, 3014

Van Altena, W.F., Lee, J.T., & Hoffleit, E.D. 1991, The General Catalog of Trigonometric Stellar Parallaxes: A Preliminary Version

Weis, E.W. 1984, ApJS, 55, 289

Weis, E.W. 1988, AJ, 96, 171

Weis, E.W. 1991, AJ, 101, 1882

Weis, E.W., & Upgren, A.R. 1982, PASP, 94, 821

Weistrop, D. 1977, ApJ, 215, 845

Young, A., Sadjai, S., & Harlan, E. 1987, ApJ, 314, 272

Table 2.1: Spectroscopic Indices

Band	S1	W	S2
TiO 5	7042-7046	7126-7135	
CaH 1	6345-6355	6380-6390	6410-6420
CaH 2	7042-7046	6814-6846	
CaH 3	7042-7046	6960-6990	

Table 2.2: Spectroscopic Observations

LHS	Name	TiO5	CaH1	CaH2	CaH3	v_{rad}	class	Source
12	G 003-036	0.894	0.852	0.746	0.878	25.1	sdM0.0	60
20	GJ 1062	0.677	0.708	0.499	0.710	-104.3	sdM2.5	RHG
29	Kapteyn's	0.810	0.778	0.594	0.792	242.8	sdM1.0	100
42	Ross 451	0.925	0.871	0.757	0.885	-148.0	sdM0.0	60
55	GJ 1200	0.439	0.816	0.420	0.705	-21.2	M3.5 V	60
57	Barnard's	0.394	0.752	0.394	0.652	-120.2	M4.0 V	60
61	Gl 817	0.645	0.823	0.582	0.799	25.9	M1.5 V	60
64	Wo 9722	0.773	0.731	0.572	0.754	-235.5	sdM1.5	RHG
104	G 030-048	1.009	0.911	0.854	0.938	-173.8	esdK7	60
156	G 004-029	0.655	0.648	0.445	0.659	-42.5	sdM3.0	100
161	G 075-047	0.964	0.739	0.515	0.751	-35.1	esdM2.0	100
169	G 005-022	1.008	0.879	0.862	0.951	-119.2	esdK7	60
170	G 078-026	1.007	0.986	0.931	0.961	-183.2	sdK	60
173	G 038-001	0.961	0.942	0.868	0.938	-159.2	sdK7	60
174	G 037-040	0.877	0.817	0.686	0.833	-225.2	sdM0.5	60
178	G 079-059	0.674	0.766	0.551	0.760	-59.7	sdM1.5	60
182	G 095-059	0.975	0.842	0.735	0.843	-238.1	esdM0.0	60
185	G 007-017	0.957	0.737	0.659	0.795	37.7	esdM0.5	60
192	LP 302-31	0.946	0.710	0.603	0.768	79.9	esdM1.0	200
205a	LP 417-44	0.889	0.512	0.347	0.513	-76.4	esdM4.5	200
211	G 099-033	0.796	0.797	0.703	0.837	-129.2	sdM0.0	100
216	G 105-023	0.725	0.743	0.496	0.732	392.5	sdM2.0	60
218	G 103-046	0.500	0.759	0.413	0.686	-20.4	M3.5 V	100
236	G 251-044	0.980	0.944	0.879	0.931	66.8	sdK7	60
254	LP 666-11	0.178	0.678	0.230	0.517	20.2	M6.5 V	100
272	LP 788-27	0.678	0.676	0.441	0.669	264.4	sdM3.0	100
276	G 117-061	0.686	0.888	0.623	0.828	46.9	M1.0 V	60
301	GJ 1146	0.481	0.773	0.431	0.683	94.4	M3.5 V	60
307	G 176-040	0.910	0.763	0.671	0.837	-64.8	sdM0.5	60
320	G 011-035	0.620	0.756	0.512	0.751	81.1	sdM2.0	60
343	G 061-021	1.001	0.953	0.901	0.937	165.5	sdK	60
364	G 165-047	0.979	0.699	0.604	0.740	12.8	esdM1.5	60
375	LP 857-48	0.829	0.499	0.372	0.547	181.2	esdM4.0	60
376	G 135-067	0.448	0.795	0.423	0.682	-19.6	M3.5 V	60
377	LP 440-52	0.232	0.567	0.205	0.396	179.7	sdM7.0	200
407	LP 803-27	0.601	0.584	0.351	0.528	-173.1	sdM5.0	60
410	G 016-018	0.724	0.822	0.612	0.814	10.5	M1.0 V	60
418	G 138-025	0.941	0.908	0.814	0.910	-14.4	K7 V	60

LHS	Name	TiO5	CaH1	CaH2	CaH3	v_{rad}	class	Source
425	G 138-059	0.646	0.762	0.503	0.738	-49.3	sdM2.0	60
453	LP 139-14	1.070	0.514	0.407	0.590	32.1	esdM3.5	200
460	GJ 1225	0.337	0.736	0.321	0.603	-53.2	M5.0 V	60
467	G 021-023	0.966	0.898	0.786	0.897	183.6	sdK7	60
479	G 142-052	0.792	0.768	0.610	0.801	-75.4	sdM1.0	60
482	Gl 781	0.774	0.718	0.558	0.746	-107.6	sdM1.5	RHG
489	LP515-3	0.998	0.853	0.766	0.889	-95.3	esdM0.0	60
491	G 210-019	0.843	0.708	0.582	0.759	-142.9	sdM1.5	60
522	G 018-051	1.024	0.926	0.854	0.929	-159.8	esdK7	60
536	G 128-034	0.883	0.784	0.659	0.826	-57.8	sdM0.5	60
537	G 028-043	1.002	1.010	0.978	0.982	-113.0	K5 V	60
1088	G 217-055	0.454	0.781	0.427	0.740	17.5	M3.5 V	60
1164	L 220-27	0.654	0.868	0.988	0.955	-22.5	K5 V	100
1174	LP 406-47	0.924	0.607	0.454	0.659	-111.7	esdM3.0	200
1481	LP 711-32	0.554	0.708	0.443	0.681	94.5	sdM3.0	RHG
1742a	LP 417-42	0.689	0.428	0.284	0.429	218.1	esdM5.5	200
1970	LP 484-6	0.878	0.589	0.475	0.657	9.8	esdM2.5	200
2110	LP 787-4	0.362	0.747	0.366	0.653	37.8	M4.0 V	100
2497	Gl 455	0.542	0.656	0.400	0.627	36.2	sdM3.5	RHG
2715	Gl 506.1	0.994	1.019	0.971	0.975	36.0	sdK	60
2852	LP 856-36	0.651	0.736	0.507	0.725	13.3	sdM2.0	RHG
3061	LP 502-32	0.737	0.497	0.292	0.497	65.4	esdM5.0	200
3073	G 137-008	0.989	0.918	0.869	0.922	-254.5	sdK7	60
3084	G 015-026	0.840	0.878	0.724	0.857	-43.8	sdK	60
3189	LP 225-22	0.341	0.637	0.305	0.579	-106.2	sdM5.0	200
3192	Gl 871	0.454	0.768	0.433	0.706	0.6	M3.5 V	60
3193	G 169-007	0.688	0.878	0.635	0.829	20.1	M1.0 V	60
3259	LP 686-36	0.995	0.811	0.657	0.803	-217.0	esdM0.5	200
3382	LP 24-219	0.937	0.635	0.485	0.667	-138.9	esdM2.5	200
3409	LP 141-1	0.443	0.645	0.355	0.587	-80.3	sdM4.5	RHG
3480	LP 869-24	0.458	0.695	0.363	0.632	12.9	sdM4.0	200
3481	LP 753-21	0.782	0.669	0.467	0.694	75.4	sdM2.5	200
3548	LP 695-96	0.886	0.839	0.435	0.660	80.6	esdM3.0	200
3628	LP 757-13	0.908	0.643	0.576	0.742	10.1	esdM1.5	100
3684	LP 518-12	0.377	0.733	0.344	0.637	-75.3	M4.5 V	200
3867	G 067-030	1.024	0.997	0.962	0.982	-108.8	sdK	60
3957	G 190-026	0.727	0.846	0.648	0.842	-85.0	M0.5 V	60
6304	G 169-009	0.587	0.785	0.505	0.751	-9.1	M2.5 V	60
...	G 017-006	0.781	0.920	0.702	0.875	8.9	M0.0 V	60
...	Sm 183	0.880	0.947	0.867	0.920	-12.3	gM	100
TVLM	832-42500	0.186	0.842	0.171	0.452	72.1	>M6.0 V	200

Table 2.3: Model Best Fits

TABLE 2.3. Model Best Fits

Star	Class	T_{eff}	$[m/H]$	Star	Class	T_{eff}	$[m/H]$	Star	Class	T_{eff}	$[m/H]$
LHS 410	M1.0 V	3700	-1.0	LHS 307	sdM0.5	3700	-1.5	LHS 3259	esdM0.5	3700	-2.0
LHS 301	M3.5 V	3700	-0.5	LHS 29	sdM1.0	3700	-1.5	LHS 192	esdM1.0	3600	-2.5
LHS 218	M3.5 V	3600	-1.0	LHS 479	sdM1.0	3700	-1.0	LHS 364	esdM1.5	3600	-2.5
LHS 3192	M3.5 V	3600	-0.5	LHS 178	sdM1.5	3600	-1.0	LHS 3628	esdM1.5	3600	-1.5
LHS 376	M3.5 V	3600	-0.5	LHS 482	sdM1.5	3600	-1.0	LHS 161	esdM2.0	3600	-2.0
LHS 6304	M2.5 V	3600	-1.0	LHS 491	sdM1.5	3600	-1.5	LHS 3382	esdM2.5	3500	-1.5
LHS 1088	M3.5 V	3500	0.0	LHS 64	sdM1.5	3600	-1.0	LHS 1970	esdM2.5	3500	-1.5
LHS 2110	M4.0 V	3500	0.0	LHS 320	sdM2.0	3600	-1.0	LHS 1174	esdM3.0	3500	-1.5
LHS 55	M3.5 V	3500	0.0	LHS 216	sdM2.0	3600	-1.0	LHS 3548	esdM3.0	3500	-1.5
LHS 57	M4.0 V	3500	-0.5	LHS 425	sdM2.0	3600	-1.0	LHS 453	esdM3.5	3400	-2.5
LHS 3684	M4.5 V	3500	-0.5	LHS 2852	sdM2.0	3600	-1.0	LHS 375	esdM4.0	3400	-2.0
LHS 460	M5.0 V	3300	0.0	LHS 20	sdM2.5	3600	-1.0	LHS 205a	esdM4.5	3400	-2.0
LHS 254	M6.5 V	3200	0.0	LHS 3481	sdM2.5	3600	-1.5	LHS 3061	esdM5.0	3300	-2.0
TVLM 832-42500	>M6.0 V	3000	0.0	LHS 272	sdM3.0	3600	-1.5	LHS 1742a	esdM5.5	3300	-2.0
				LHS 156	sdM3.0	3600	-1.5				
				LHS 1481	sdM3.0	3600	-1.0				
				LHS 2497	sdM3.5	3500	-1.0				
				LHS 3480	sdM4.0	3500	-1.0				
				LHS 3409	sdM4.5	3400	-1.0				
				LHS 3189	sdM5.0	3400	-1.0				
				LHS 407	sdM5.0	3400	-1.5				
				LHS 377	sdM7.0	3200	-1.5				

Table 2.4: Photometry

LHS	V	B-V	V-R	R-I	V-I	π ($''$)	σ_π ($''$)	Δ_{LK}	M_V	Source
12	12.24	1.45	0.90	0.90	1.80	0.0359	0.0031	-0.08	10.02	Y,L
20	13.01	1.68	1.03	1.17	2.20	0.0648	0.0025	-0.01	12.07	Y,L
29	8.84	1.56	0.96	1.00	1.96	0.2583	0.0065	-0.01	10.9	Y,L
35	12.83	1.72	1.25	1.67	2.92	0.1480	0.0022	-0.00	13.68	Y,L
42	12.23	1.45	1.06	0.92	1.98	0.0327	0.0025	-0.06	9.8	Y,E79
44	6.45	0.76	...	...	...	0.1127	0.0014	-0.00	6.71	Y,S
52	9.43	0.84	0.52	0.49	1.01	...	...	...	...	R
53	9.04	0.78	0.45	0.46	0.91	...	...	...	...	R
55	12.90	1.54	...	...	...	0.0550	0.0029	-0.03	11.6	H,S
64	13.30	1.55	...	...	...	0.0419	0.0022	-0.03	11.41	Y,S
103	14.16	...	1.15	1.47	2.62	0.0536	0.0021	-0.02	12.81	Y,WU
104	13.78	1.34	0.81	0.91	1.72	...	...	...	...	E79
137	13.36	1.60	...	...	...	0.0463	0.0027	-0.03	11.69	Y,S
139	15.05	1.86	1.24	1.61	2.85	0.0485	0.0044	-0.09	13.48	Y,E79
156	14.89	1.70	0.92	1.25	2.17	0.0277	0.0035	-0.18	12.1	Y,E79
161	14.75	1.55	1.01	0.96	1.98	0.0260	0.0048	-0.42	11.82	Y,E79
163	13.06	1.57	1.12	1.43	2.55	0.0496	0.0043	-0.08	11.54	Y,B
169	14.13	1.45	0.91	0.76	1.72	0.0309	0.0023	-0.06	11.58	Y,L,E79
170	10.69	1.22	0.80	0.70	1.50	0.0348	0.0025	-0.05	8.4	Y,E79
173	11.12	1.31	...	...	...	0.0353	0.0031	-0.08	8.86	Y,S
174	12.75	1.52	0.94	0.89	1.83	0.0204	0.0045	-0.65	9.3	Y,DF89
175	9.91	0.65	...	...	...	0.0218	0.0022	-0.11	6.6	Y,R
178	12.90	1.55	0.95	1.11	2.06	0.0451	0.0066	-0.24	11.17	Y,E79
182	13.42	1.57	...	...	...	0.0234	0.0025	-0.12	10.27	Y,S
185	15.30	1.79	0.98	0.85	1.83	0.0167	0.0046	L	11.41	Y,DF89
192	17.33	...	...	...	1.98	0.0102	0.0008	-0.06	12.37	M92
205a	18.93	...	...	...	2.35	0.0104	0.0013	-0.17	14.02	M92
211	14.11	1.45	0.91	1.05	1.96	0.0188	0.0029	-0.28	10.48	Y,L
216	14.66	1.62	0.99	1.09	2.08	0.0306	0.0030	-0.10	12.09	Y,L
218	14.84	1.57	1.12	1.33	2.45	0.0296	0.0030	-0.11	12.2	Y,DF89
232	13.72	1.15	...	...	...	0.0148	0.0025	-0.34	9.57	Y,S
236	13.10	1.33	...	...	...	0.0187	0.0018	-0.10	9.46	Y,S
241	8.32	0.62	...	...	...	...	...	...	...	S
254	17.41	1.75	1.90	2.07	3.97	...	...	...	...	L
272	13.46	...	1.34	1.36	2.70	...	...	...	...	DF89
276	11.86	1.43	0.93	1.04	1.97	0.0347	0.0025	-0.05	9.56	Y,B
301	13.57	1.57	1.08	1.39	2.47	0.0540	0.0036	-0.04	12.23	Y,W7
307	15.22	1.56	...	...	1.92	0.0183	0.0027	-0.25	11.53	Y,L*
320	14.00	1.54	0.88	1.26	2.14	0.0260	0.0034	-0.19	11.07	Y ,E79

LHS	V	B-V	V-R	R-I	V-I	π ($''$)	σ_π ($''$)	Δ_{LK}	M_V	Source
343	13.87	1.30	0.87	0.69	1.56	0.0167	0.0031	-0.43	9.98	H,L
364	14.61	1.71	1.03	0.92	1.95	0.0374	0.0037	-0.10	12.47	Y,DF92
375	15.68	1.87	1.08	1.12	2.20	0.0395	0.0010	-0.01	13.66	RA
376	15.00	1.64	1.08	1.33	2.41	0.0207	0.0048	-0.74	11.58	Y,E79
377	18.39	...	...	...	3.48	0.0284	0.0008	-0.01	15.66	M92
407	16.57	1.93	1.06	1.33	2.39	0.0315	0.0020	-0.04	14.06	RA
410	13.36	...	0.94	1.06	2.00	0.0240	0.0034	-0.23	10.26	Y,H,W1
418	13.51	1.42	0.88	0.80	1.68	0.0141	0.0033	-0.76	9.26	H,La
420	7.30	0.54	...	...	...	0.0324	0.0057	-0.37	4.85	Y,S
425	15.00	1.60	...	...	...	0.0261	0.0047	-0.40	12.08	Y,S
453	18.02	...	...	...	2.22	0.0103	0.0009	-0.08	13.08	M92
460	15.40	1.77	1.34	1.70	3.04	0.0544	0.0028	-0.03	14.08	Y,DF92
467	12.21	1.43	...	...	1.70	0.0362	0.0020	-0.03	10	Y,L
479	14.31	1.51	...	...	...	0.0224	0.0023	-0.11	11.06	Y,S
482	11.98	1.56	0.95	1.04	1.99	0.0603	0.0017	-0.01	10.88	Y,L
489	15.48	1.69	0.91	0.86	1.77	0.0189	0.0036	-0.45	11.86	Y,DF89
491	14.70	1.68	0.98	0.98	1.96	0.0211	0.0036	-0.35	11.32	Y,DF92
522	14.15	1.41	0.84	0.78	1.62	0.0268	0.0021	-0.06	11.29	Y,B
536	14.65	1.55	...	...	...	0.0227	0.0025	-0.13	11.43	Y,S
537	9.96	0.70	...	...	...	...	...	...	...	S
1174	16.99	...	...	...	2.09	0.0157	0.0012	-0.06	12.97	M92
1319	14.82	1.45	...	...	...	...	...	...	...	S
1481	12.67	1.73	1.08	1.32	2.40	...	...	...	...	G,E87
1555	13.90	1.70	...	...	...	0.0168	0.0019	-0.14	10.03	Y,S
1742a	18.80	...	...	...	2.74	0.0134	0.0012	-0.08	14.44	M92
1970	17.76	1.68	...	...	2.09	0.0129	0.0008	-0.04	13.31	M,L
2045	18.49	...	...	...	2.46	0.0111	0.0009	-0.07	13.72	M92
2110	16.97	...	...	...	2.84	0.0151	0.0010	-0.04	12.86	M92
2204	16.80	...	...	...	3.23	0.0288	0.0009	-0.01	14.1	M92
2497	12.85	1.74	1.08	1.22	2.47	0.0493	0.0031	-0.04	12.06	Y,S
2715	10.83	1.03	0.62	0.55	1.17	0.0286	0.0033	-0.14	8.11	Y,AM,B
2852	12.15	1.70	1.06	1.22	2.18	0.0395	0.0174	L	10.13	Y,E87
3061	19.50	...	...	...	2.61	0.0089	0.0008	-0.08	14.25	M92
3073	13.69	1.41	0.84	0.74	1.58	0.0187	0.0034	-0.41	10.05	Y,DF92
3084	13.43	1.43	0.93	0.90	1.83	0.0190	0.0025	-0.19	9.82	Y,DF92
3181	17.18	1.69	1.02	1.19	2.21	0.0265	0.0030	-0.14	14.3	RA
3189	18.10	...	1.11	1.70	2.81	...	...	...	...	HCM
3192	14.76	1.63	1.11	1.38	2.49	0.0274	0.0023	-0.07	11.95	Y,
3193	12.49	1.43	0.93	0.99	1.92	0.0274	0.0023	-0.07	9.68	Y,DF92
3259	18.26	...	...	...	2.03	0.0064	0.0012	-0.44	12.29	M92

LHS	V	B-V	V-R	R-I	V-I	π ($''$)	σ_π ($''$)	Δ_{LK}	M_V	Source
3382	17.02	1.99	1.03	1.06	2.09	0.0104	0.0009	-0.08	12.11	M,L
3409	15.16	1.85	1.21	1.61	2.82	0.0500	0.0013	-0.01	13.65	Y,M92
3480	17.24	···	···	···	2.76	0.0177	0.0008	-0.02	13.48	M92
3481	17.58	···	···	···	2.35	0.0067	0.0007	-0.12	11.71	M92
3548	17.52	1.78	···	···	2.09	0.0083	0.0006	-0.05	12.12	M,L
3555	17.93	1.94	1.10	0.97	2.07	0.0125	0.0060	L	13.41	RA
3628	17.41	···	···	···	2.05	0.0088	0.0008	-0.09	12.13	M92
3684	17.95	···	···	···	2.92	0.0152	0.0010	-0.04	13.86	M92
3867	13.41	1.19	···	···	···	0.0120	0.0050	L	8.81	Y,S
3957	13.55	1.39	···	···	···	0.0257	0.0037	-0.23	10.6	Y,S
4037	13.52	0.88	···	0.47	···	···	···	···	···	R89
6304	14.07	···	1.05	1.25	2.30	···	···	···	···	W4

L indicates the Lutz-Kelker correction is undefined but < -0.80.
References for the trigonometric parallaxes and photometry are: B - Bessell (1990), DF89 - Dawson and Forbes (1989), DF92 - Dawson and Forbes (1992), E79 - Eggen (1979), E87 - Eggen(1987), G - Gliese and Jahreiss (1991), H - Harrington and Dahn (1980), L - Leggett (1992), M92 - Monet et al. (1992), R - Ryan (1992), RA - Ruiz and Anguita (1993), S - SIMBAD, T - Tinney et al. (1995), W4 - Weis (1984), W7 - Weis (1987), W1 - Weis (1991), WU - Weis and Upgren (1982), Y - Van Altena et al. (1991)

Table 2.5: Space Velocities

LHS	U	V	W	v_{tan}	LHS	U	V	W	v_{tan}
LHS 12	-196	-254	15	321	LHS 453	-239	-148	371	465
LHS 20	140	-185	76	221	LHS 460	151	-48	20	151
LHS 29	19	-284	-53	159	LHS 467	282	-90	-117	260
LHS 42	178	-416	180	465	LHS 479	189	-260	-17	313
LHS 55	-92	-100	112	175	LHS 482	103	-116	19	114
LHS 57	-148	0	16	89	LHS 489	147	-257	-116	304
LHS 61	121	-141	-3	184	LHS 491	245	-210	70	298
LHS 64	259	-190	-88	237	LHS 522	30	-318	-83	289
LHS 156	1	-204	-42	204	LHS 522	30	-318	-83	289
LHS 161	-84	-236	94	265	LHS 536	-268	-121	-31	290
LHS 169	32	-273	51	253	LHS 1088	-175	-57	114	216
LHS 170	96	-234	-13	175	LHS 1174	-88	-286	-19	278
LHS 173	56	-255	16	208	LHS 1742a	-229	-263	108	293
LHS 174	139	-382	-127	362	LHS 1970	158	-318	-49	359
LHS 178	60	-165	-6	165	LHS 2110	154	-103	4	181
LHS 182	123	-335	-118	291	LHS 2497	-71	-38	21	76
LHS 185	4	-289	-169	333	LHS 2715	-57	-94	28	108
LHS 192	-143	-463	-60	482	LHS 2852	-34	-5	57	65
LHS 205a	119	-455	-45	466	LHS 3061	73	-277	103	297
LHS 211	200	-247	99	307	LHS 3073	-239	-238	-76	234
LHS 216	-321	-311	-14	216	LHS 3084	31	-223	-65	230
LHS 218	4	-188	-77	202	LHS 3192	45	-136	72	160
LHS 236	-207	-229	93	315	LHS 3193	55	-126	85	160
LHS 276	-115	-115	-47	163	LHS 3259	-189	-382	125	388
LHS 301	-7	-179	8	153	LHS 3382	-302	-232	-60	360
LHS 307	173	-247	33	296	LHS 3409	-30	-100	42	79
LHS 320	-38	-215	0	203	LHS 3480	-13	-72	-124	144
LHS 343	107	-418	89	408	LHS 3481	274	-314	-6	410
LHS 364	120	-53	19	132	LHS 3548	335	-331	-67	470
LHS 375	24	-188	155	166	LHS 3628	273	-215	112	365
LHS 376	-173	-295	98	356	LHS 3684	162	-197	-58	251
LHS 377	207	-125	125	205	LHS 3867	-149	-186	-78	227
LHS 407	-215	-160	-24	206	LHS 3957	-148	-125	40	179
LHS 410	165	-190	-112	276	TVLM 832-42500	-120	-22	8	99
LHS 418	279	-240	-161	402					

Table 2.6: Velocity Statistics

Group	N	$< V >$	σ_U	σ_V	σ_W
dM	16	-134	125	78	71
sdM	26	-202	177	100	82
esdM	19	-287	176	95	126
sdK	5	-238	111	118	61
strong CaH1	24	-38	61	44	30
weak CaH1	157	-26	48	30	24
Disk (RHG)	514	-22	43	31	25

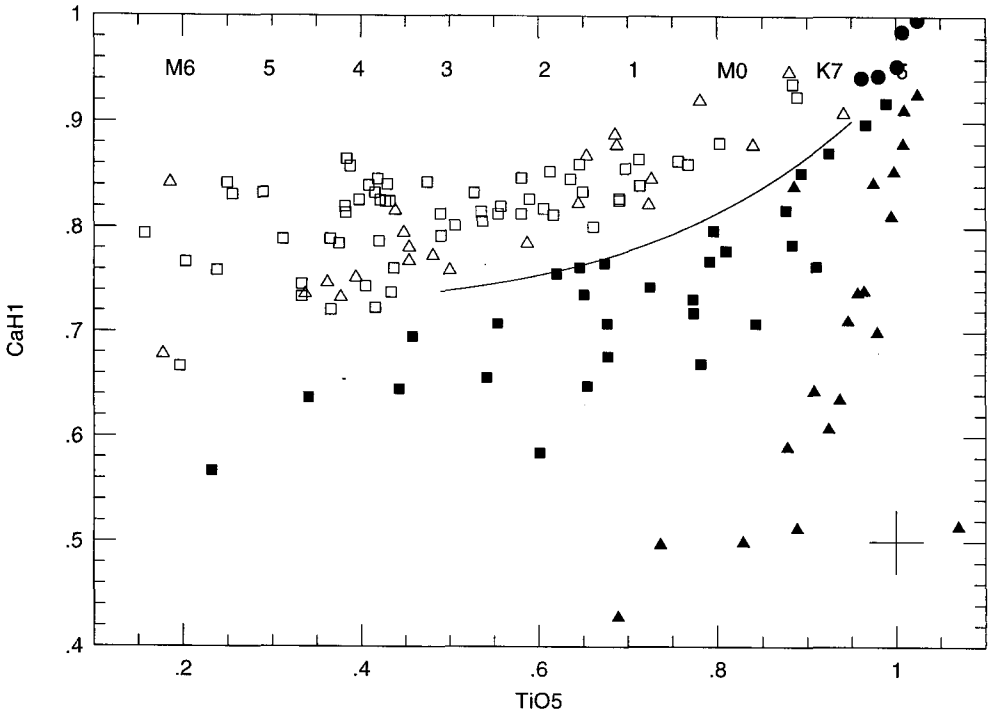

Figure 2.1: The CaH indices as a function of TiO5. Stars classified as sdM appear as filled squares, esdM as filled triangles, sdK as filled circles, and spectroscopic non-subdwarfs as open triangles. In the CaH1 diagram we also plot the single stars within eight parsecs as open squares. All other figures use the same symbols. Representative error bars (± 0.03) appear in the lower right.

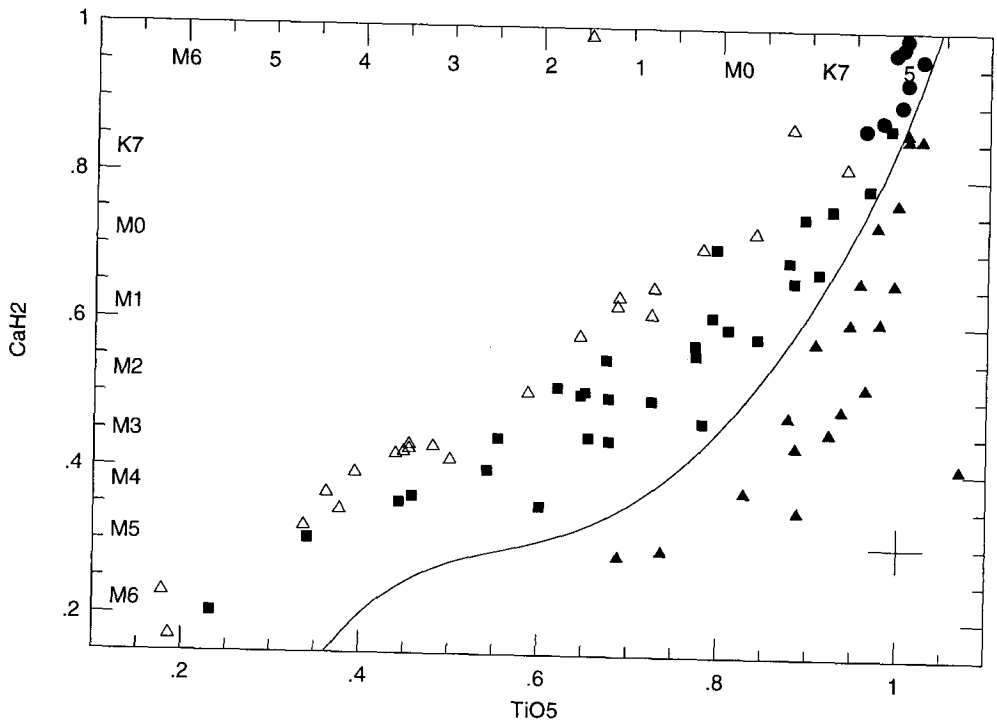
M6
5
4
3
2
1
M0
K7
5
K7
M0
M1
M2
M3
M4
M5
M6
1
.8
.6
.4
.2
CaH2
.2
.4
.6
.8
1
TiO5

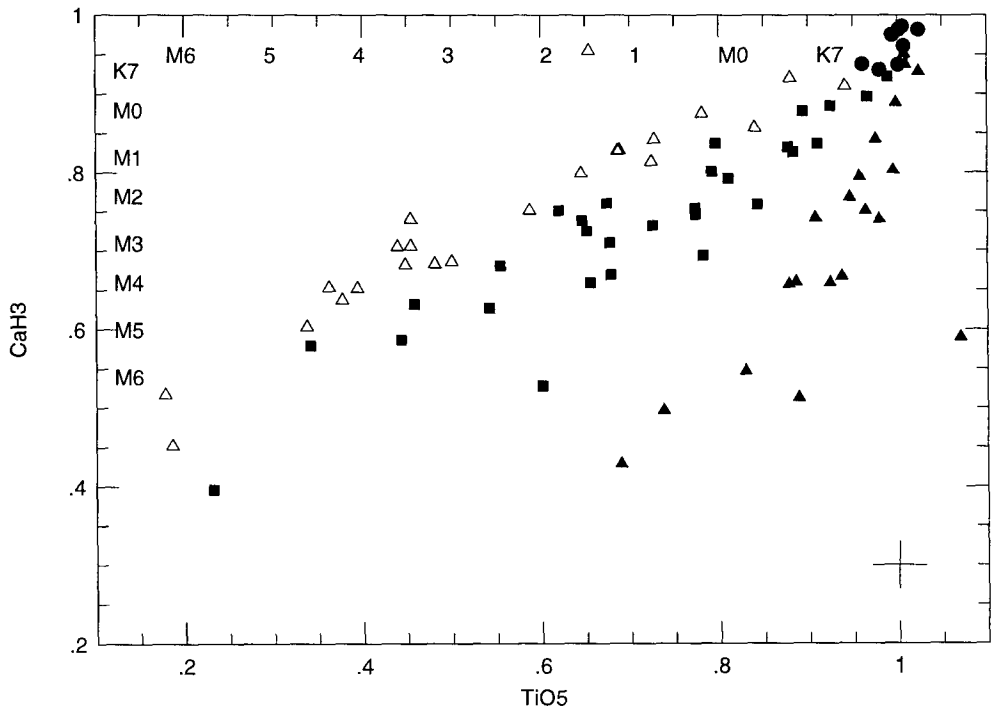
M6
5
4
3
2
1
M0
K7
K7
M0
M1
M2
M3
M4
M5
M6
1
.8
.6
.4
.2
CaH3
.2
.4
.6
.8
1
TiO5

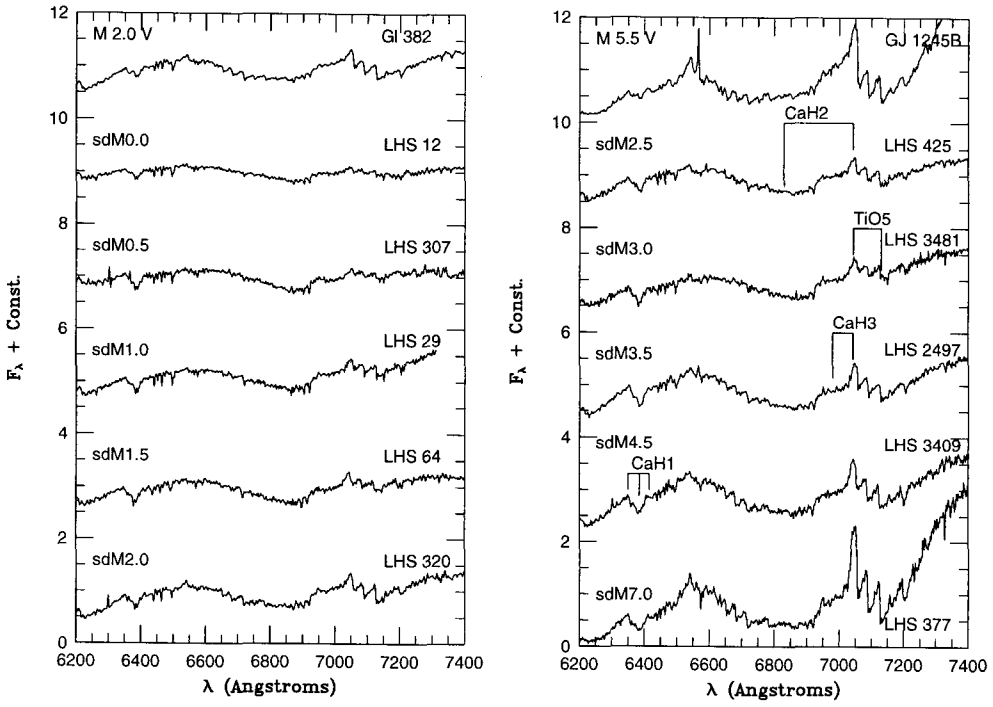

Figure 2.2: A sequence of M subdwarfs (sdM). The positions of the bandstrength indexes defined in Table 1 appear on the right. Two near-solar metallicity KHM spectral standards are also shown at the top.

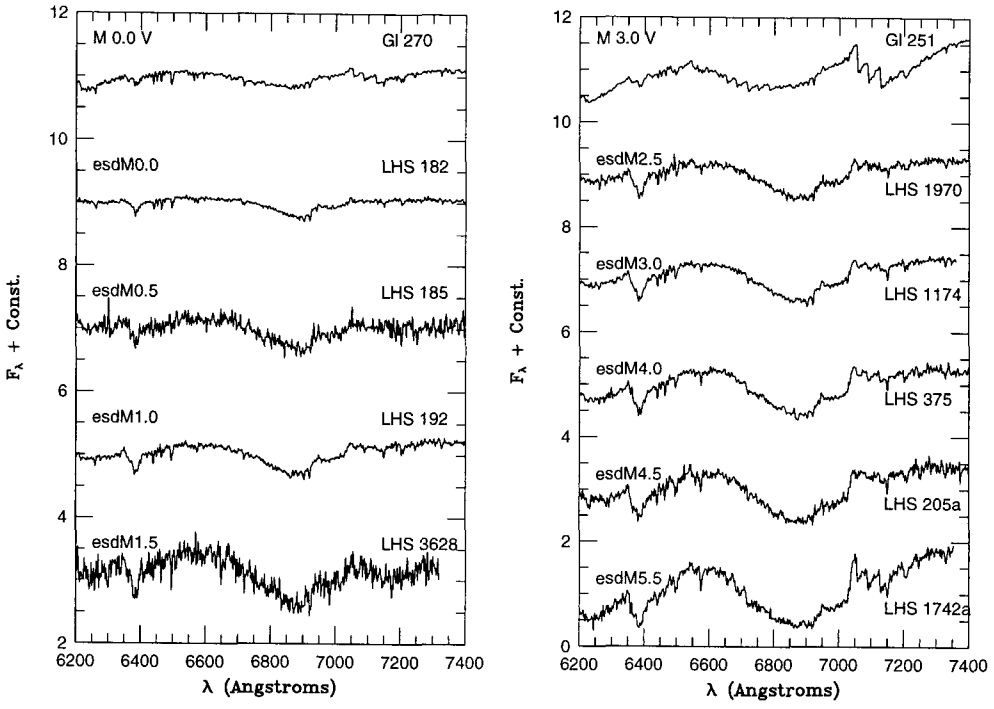

Figure 2.3: A sequence of extreme M subdwarfs (esdM). Two near-solar metallicity KHM spectral standards are also shown at the top.

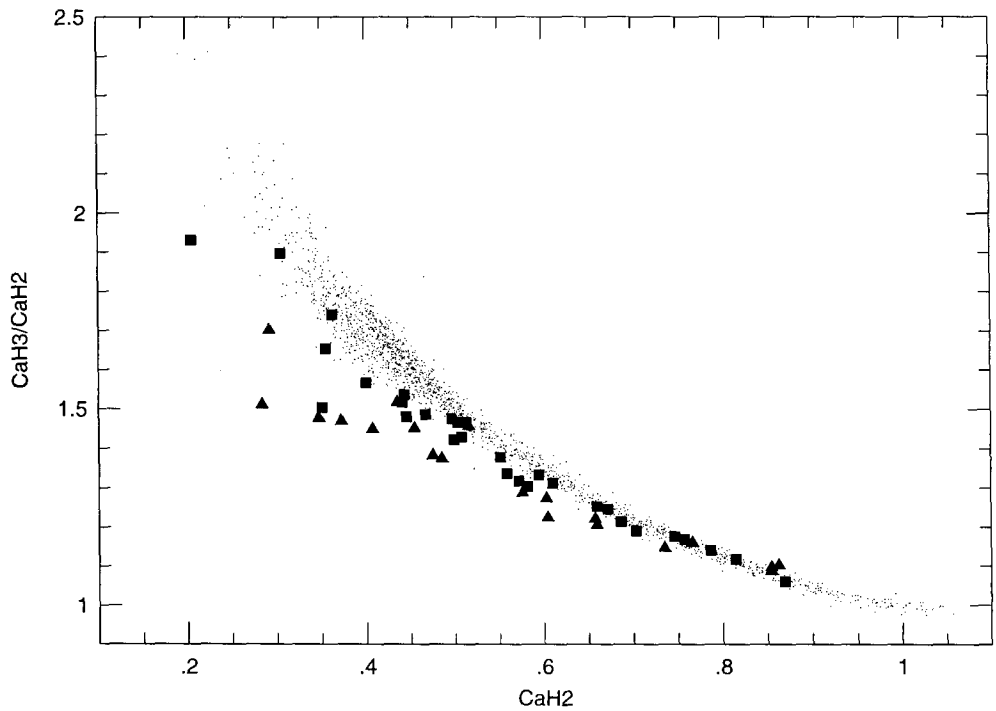

Figure 2.4: The CaH3/CaH2 ratio as function of CaH2. The sdM and esdM lie below the RHG Population I relation. The RHG stars appear as dots.

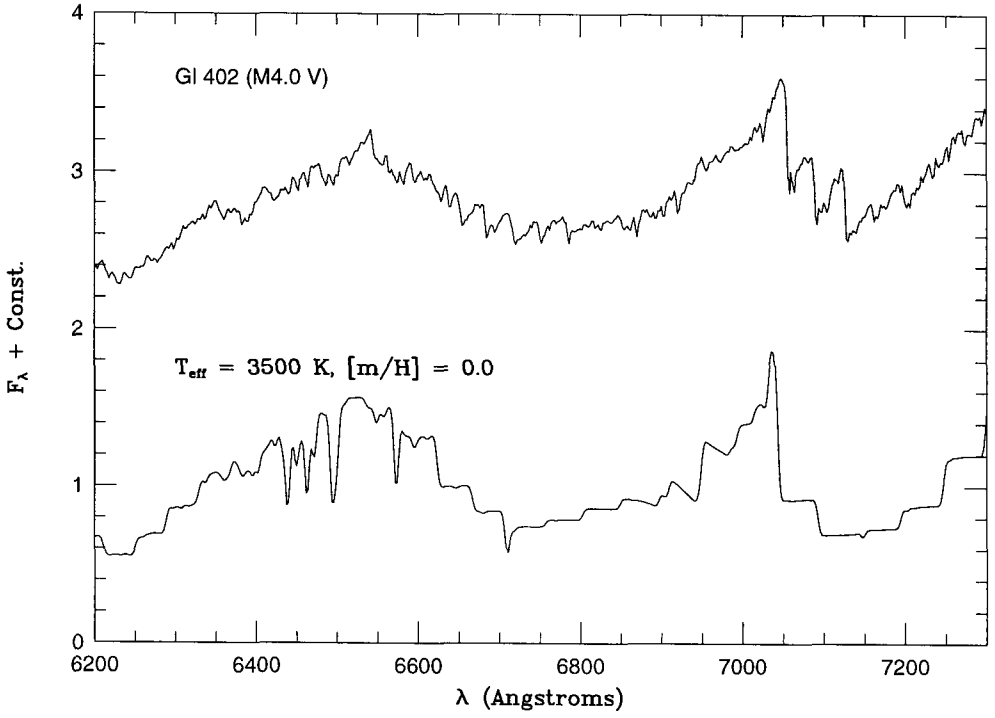

Figure 2.5: A model atmosphere fit to the Population I star Gl 402, an M 4.0 V standard. Note that the overly strong atomic lines are an artifact of the computation technique.

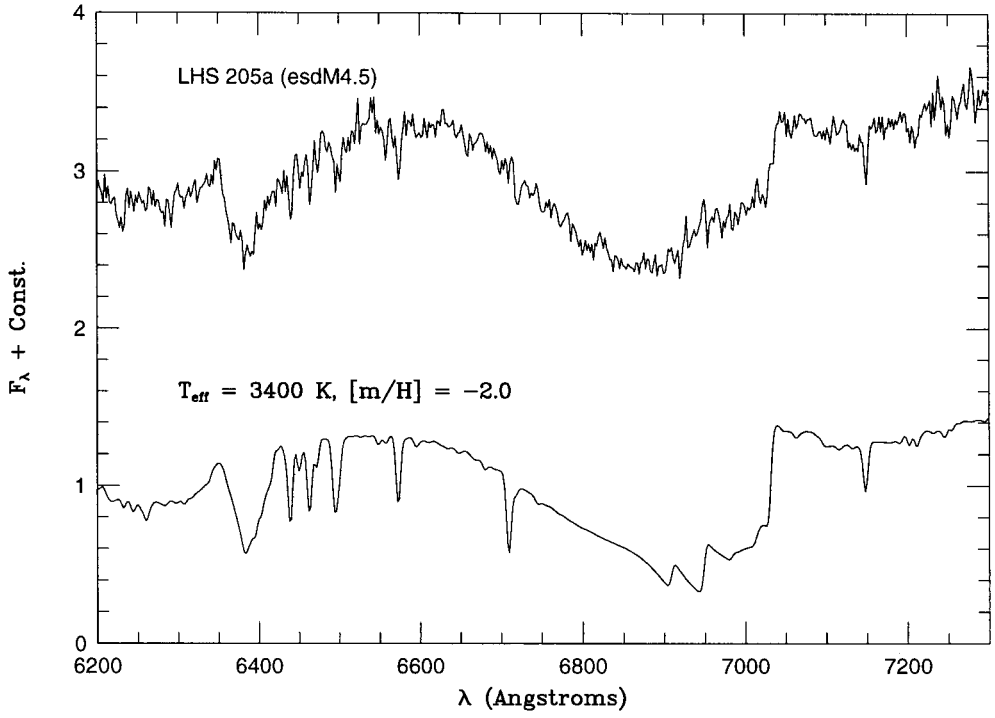

Figure 2.6: Model Atmosphere fit to the extreme subdwarf LHS 205a

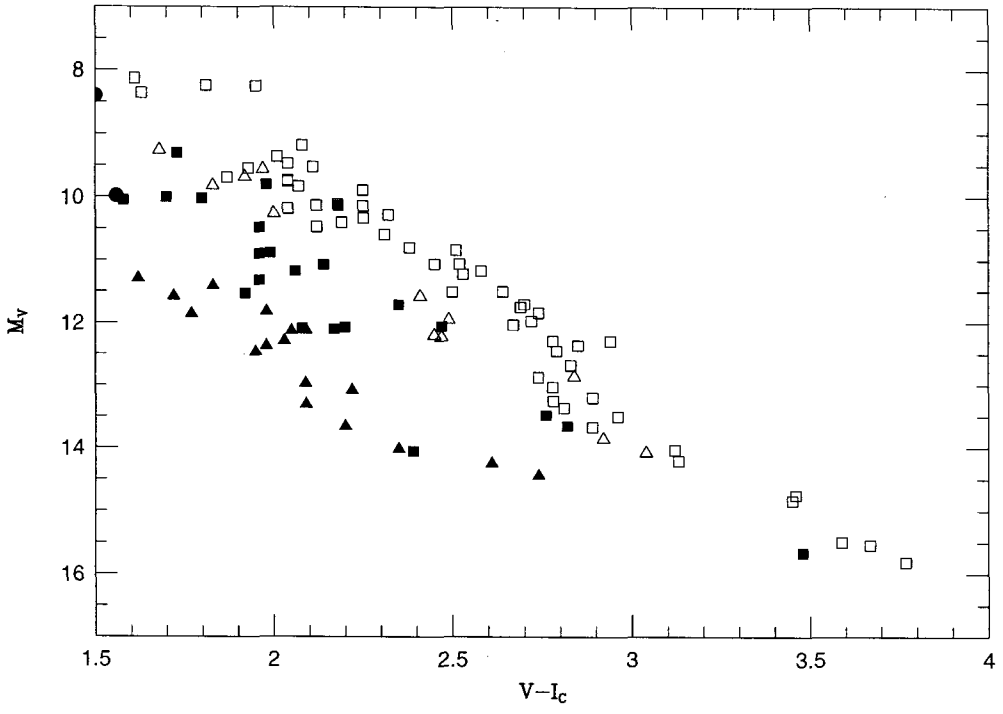

Figure 2.7: The observed HR diagram. The spectroscopic extreme subdwarfs (esdM) are filled triangles, the intermediate subdwarfs (sdM) are filled squares, and the subdwarf candidates that were spectroscopically indistinguishable are open triangles. The open squares are the single stars within eight parsecs with good parallaxes – note the step at V-I $\sim$ 2.8 which is discussed in HGR.

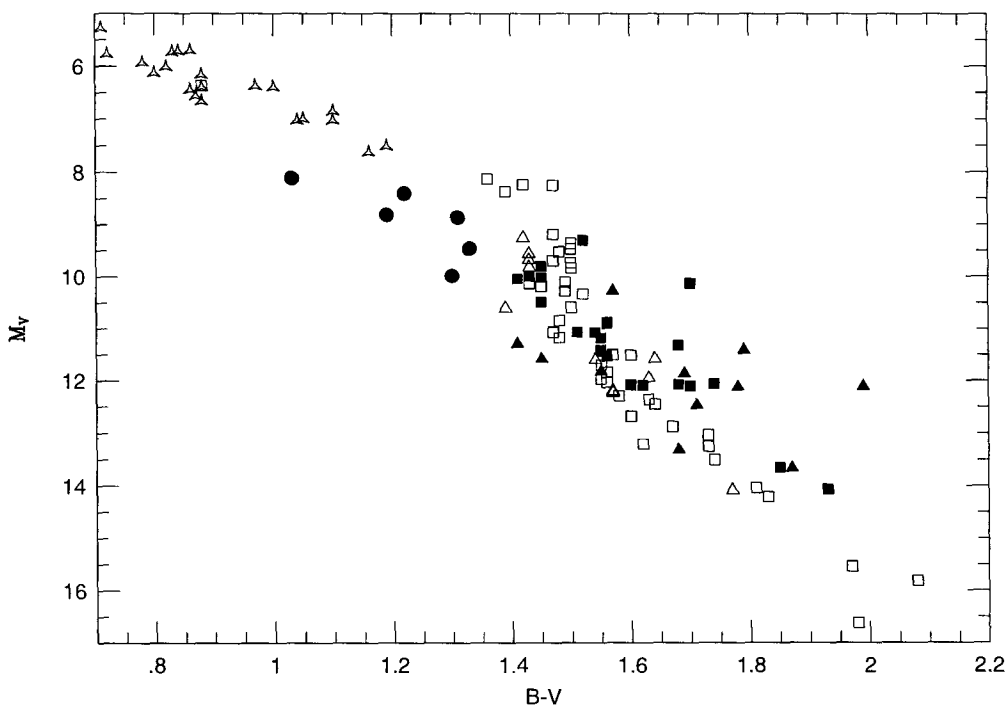

Figure 2.8: The HR diagram for B-V colors. The three pointed stars are nearby G and K dwarfs. Note that the blue K-subdwarfs lie below the disk sequence, but the sdM and esdM sequences cross the disk main sequence and are actually brighter at the reddest colors.

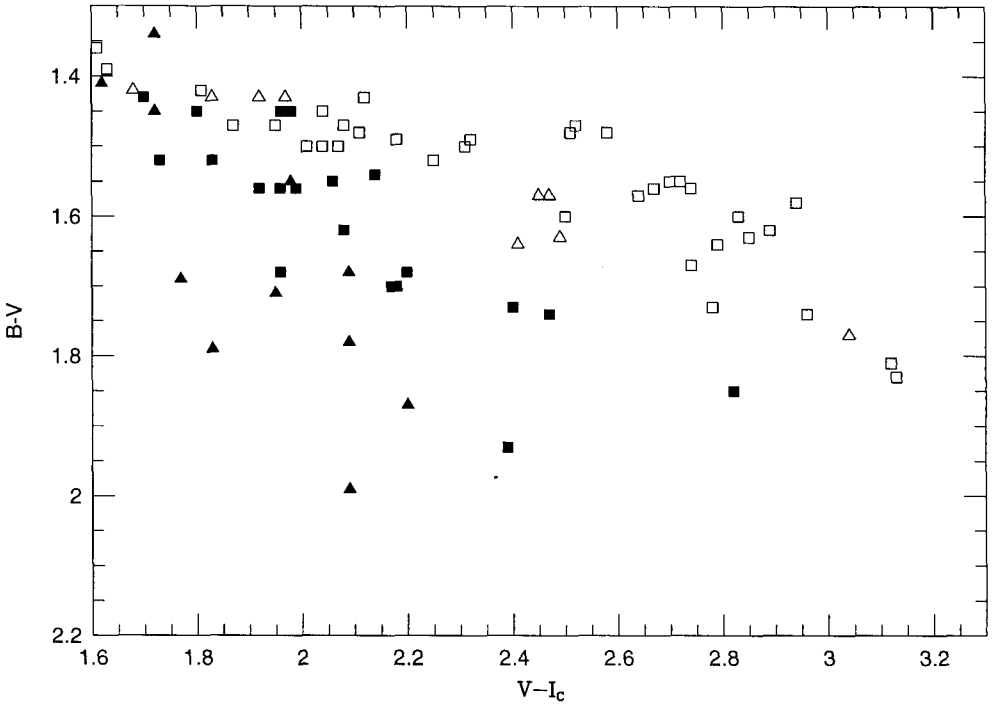

Figure 2.9: V-I vs. B-V. The sdM are redder in B-V at a given V-I color than the disk stars. The esdM show a larger offset than the sdM.

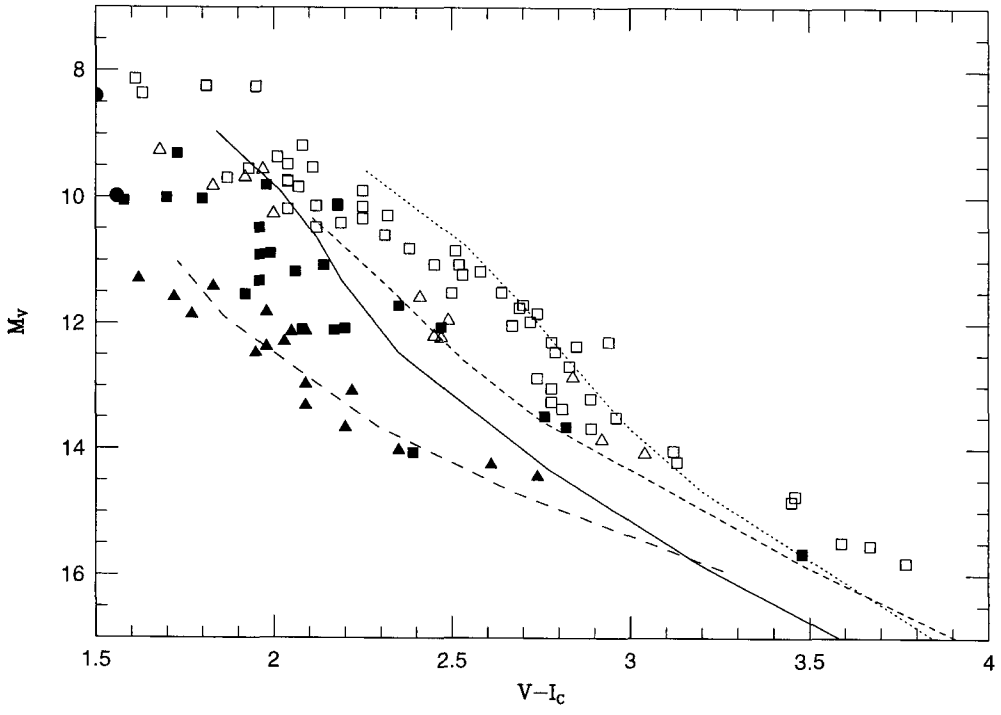

Figure 2.10: The observed HR diagram with theoretical sequences. Metallicities of $[m/H] = 0.0$ (dotted line), -0.5 (short dashed line), and -1.5 (long dashed line) from Baraffe et al. (1995). A more recent solar metallicity model (solid line) computed by Baraffe and Chabrier using the NextGen model atmospheres is also shown. The latter model does not match the observed disk stars, but the agreement of the previous models is quite good.

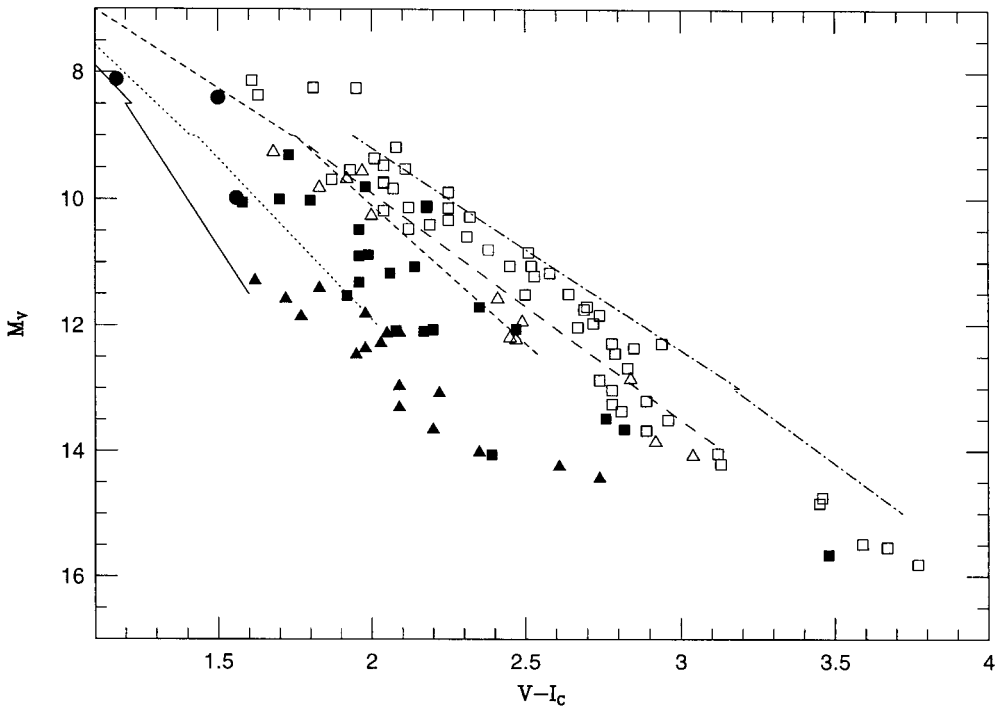

Figure 2.11: The observed HR diagram with the cluster main sequences fit by Santiago et al.(1996) using HST observations. From left to right, the clusters are M15 (solid line, $[Fe/H] = -2.26$), ω Cen (dotted, -1.6), 47 Tuc (short dashed, -0.6), N2420 (long dashed, -0.45), and N 2477 (long dash-dotted, 0.00). Note that the position of the cluster sequences agrees with our spectroscopic metallicity estimates. The slopes of the cluster sequences do not disagree with the local subdwarfs in the region of color overlap when using our classifications. The discrepancy of the reddest stars in the metal rich clusters may be due to color terms, as well as the inadequacy of a linear fit for the main sequence.

Chapter 3 M Subdwarf Secondaries: A Test of the Metallicity Scale

Abstract

We present spectra of three M subdwarfs which are common proper motion companions to F or G subdwarfs of known metallicity. The assumption that the companions have the same composition allows us to test the Gizis (1997, AJ, 113, 806) M subdwarf classification system and its correspondence to metallicity. The results are in excellent agreement with the Gizis (1997) scale, thereby showing that the Allard & Hauschildt (1995, ApJ, 445, 433) Extended model atmospheres agree well in the 6200 – 7400Å region for cool metal-poor stars. We also show that the results are consistent with the main sequences of globular clusters using the Reid (1997, AJ, 114, 161) distance scale.

3.1 Introduction

The metal-poor stars of the thick disk and halo provide an invaluable record of Galactic history. The main-sequence FGK subdwarfs have proven to be an important source of information on these populations (e.g., Carney et al. 1994). The much cooler and fainter M subdwarfs offer an important alternative tracer group. Indeed, in addition to the possibility of observing nearby proper motion M subdwarfs, it is now feasible to obtain both photometry for the M subdwarfs in globular clusters with the Hubble Space Telescope (e.g., Santiago, Elson, & Gilmore 1996) and spectra for M dwarfs and M subdwarfs at distances of a few kiloparsecs above the galactic plane with 10-meter class telescopes (Reid et al. 1997). Using these objects as probes of Galactic structure, however, requires a good understanding of their properties in order to derive

metallicities and luminosities.

Gizis (1997, hereafter G97) has presented a spectroscopic classification scheme which is based on moderate resolution ($\sim$ 3Å) spectra covering the wavelength range 6200 – 7400 Å. Quantitative bandstrength indices measuring TiO and CaH features are used to classify stars as M V (ordinary disk stars), sdM (M subdwarfs), and esdM (extreme M subdwarfs). Comparison to the Allard & Hauschildt (1995) synthetic spectra allowed G97 to show that these classes correspond to $[m/H] \sim 0.0$, $[m/H] \sim -1.2 \pm 0.3$, and $[m/H] \sim -2.0 \pm 0.5$ respectively. Comparison of the $(M_V, V-I)$ HR diagram shows that HST globular cluster sequences (Santiago, Elson, & Gilmore 1996) and stellar interior calculations with Allard & Hauschildt (1995) model atmospheres (Baraffe et al. 1995) are in agreement with this scale; however, serious systematic errors could in principle affect all of these methods of estimating metallicity.

We present spectra of three M subdwarfs which are companions to hotter subdwarfs of known metallicity. Our aim is to test the metallicities derived from the M subdwarf spectra by comparison with those measured for their better understood primaries. The data are presented in Section 3.2, the implications for the metallicity scale are discussed in Section 3.3, and the results are summarized in Section 3.4.

3.2 Observations

We observed two systems (G116-009; G176-046) whose low-luminosity components were recently discovered (Martin & Rebolo 1992; Martin, Rebolo, & Zapatero Osorio 1995). We also observed VB 12 (LHS 541), the low luminosity companion to HD 219617 (LHS 540) discovered by van Biesbroeck (1961). All three stars were identified as common proper motion companions to already-known, relatively-bright high proper motion objects. We refer to the low-luminosity component of G 116-009 as G 116-009B and the primary as G 116-009A. CLLA find that G 116-009A has $B-V = 0.86$, corresponding to $T_{eff} = 4750$ K. The case of the G 176-046 system is rather complicated — Martin et al. (1995) note that their object is the fourth member of this system, since Latham et al. (1992) deduce that G 176-046 is a spatially unresolved

triple from their high-resolution spectra. We therefore will refer to the low-luminosity companion as G 176-046D and the primary as G 176-046ABC. Latham et al. (1992) find that this "primary" has $B-V=0.80$ and $T_{eff}=4860$ K. In fact, this system is a quintuple system, since Ryan (1992) has shown that LP 215-35 is a common proper motion companion at 343″ separation. This companion has $B-V=0.86$. VB 12's primary, HD 219617, is itself a double star with a orbital semi-major axis of 0.80″ (Heintz 1991). CLLA find $B-V=0.48$ and $T_{eff}=5857$ K.

The stars were observed with the Palomar 200-in on UT Date 1 June 1997 using the Double Spectrograph. A dichroic which divided the light at 5500Å was used. The red camera was used with a 600 l/mm grating, yielding wavelength coverage from 6040 to 7380Å at $\sim$ 3Å resolution. Very few counts were obtained in the blue camera for the M subdwarfs and those data were therefore not used. The setup is similar to that used by Reid, Hawley, & Gizis (1995) and G97. The spectra were wavelength calibrated with neon and argon lamps and flux calibrated with the Gunn & Oke (1983) standards using FIGARO.

The resulting spectra are plotted in Figure 3.1. We measure bandstrength indices defined in Table 3.4 as the ratio of flux in the features (W) to flux in the pseudo-continuum regions (S1 and S2). They were originally defined in Reid et al. (1995). Our measurements of the indices as well as photometry from the literature are reported in Table 3.2. Standards from Marcy & Benitz (1989) were used as templates to determine radial velocities accurate to ± 20 km s^{-1} for the M subdwarfs. All are consistent with the more precisely-known primary velocities. The metallicities derived by Carney et al. (1994, hereafter CLLA) for the primaries are also listed in Table 3.2.

3.3 The Metallicity Scale

G97 found that the mean $[m/H]$ for the sdM and esdM are -1.2, with a range of ± 0.3, and -2.0, with a range of ± 0.5, respectively. G97 also argued that stars of $[m/H] \gtrsim -0.6$ are not distinguishable on the basis of their indices from ordinary

(near solar metallicity) nearby M dwarfs. The three stars in the present sample have classifications of M1.0 V, sdM0.5, and sdM3.0. We can derive more quantitative metallicity estimates by considering the values of bandstrength indices rather than the shorthand classification. The three stars are compared to the G97 standards in the TiO-CaH diagrams in Figure 3.2. The two sdM stars G 116-009B and VB 12 lie quite close to separation line between sdM and esdM, implying that they have similar $[m/H]$ near to the lower end of the sdM range, i.e. -1.4 or -1.5. The indices of G 176-046D indicate that it is substantially more metal-rich than the other stars. Although classified as "M1.0 V", G 176-046D lies within 0.01 in CaH1 of being classified as "sdM." This offset is less than the observational error of ± 0.02. We conclude that this subdwarf lies at the upper range of sdM abundances and at the lower extreme of the high-velocity disk (Intermediate Population II) stars, so $-0.6 < [m/H] \lesssim -0.9$.

These expectations from the analysis of the M subdwarf spectra are confirmed by the CLLA measurements of the primaries. G 116-009A has $[m/H] = -1.46$[1]. This system provides the cleanest test, since CLLA's finding of no radial velocity variations implies the primary is single. HD 219617 has $[m/H] = -1.40$ but is an unresolved binary. It should be noted that Axer, Fuhrmann, & Gehren (1994) derive a significantly higher value of $[Fe/H] = -1.08$, but specifically note that their value is "suspect." The CLLA values are in good agreement with our M subdwarf estimates for both stars above. Finally, we must consider G 176-046. CLLA derive $[m/H] = -1.07$ but since the "primary" is made up of three stars this value is uncertain. An independent estimate may be obtained from the Ryan (1992) UBV photometry of the distant subdwarf companion LP 215-35. Inspection of Ryan's Figure 1 shows that LP 215-35 is more metal-rich than $[m/H] = -1$. His photometry of G 176-046ABC implies $[m/H] = -1$, but this may also be affected by its unresolved nature. The M subdwarf calibration, indicating that the system is probably slightly more metal-rich than -1, is more consistent with the LP 215-35 photometry than with

[1]The metallicities for G 116-009A and G 176-46ABC cited in Martin et al. (1995) are those derived by Laird, Carney, & Latham (1988) which are significantly more metal-poor than the more recent estimates given by CLLA. As a result, the comparison of G176-046 and G116-009 to ω Cen made by Martin et al. is no longer appropriate.

the G 176-046ABC data. In any case, we can at least conclude that $[m/H] = -1.07$ measurement is consistent with the position of G 176-046D above the $[m/H] \sim -1.2$ sdM but below the $[m/H] \sim -0.6$ stars.

The spectroscopic classification can be tested against position in the HR diagram for VB 12[2]. HD 219617 has a Hipparcos trigonometric parallax ($\pi = 12.41 \pm 2.04$ milliarcseconds). VB 12 has $V = 16.46$, $V - I = 2.09$, (Bessell 1990) implying $M_V = 11.93$. These values place it slightly above the extreme subdwarf sequence (Monet et al. 1992; Gizis 1997) as expected from the bandstrength indices.

The current G97 M-subdwarf metallicity scale is in good agreement with the CLLA metallicities although the possibility remains of systematic uncertainties at the ± 0.3 dex level. One potential problem is the elemental abundance ratios used in the Allard & Hauschildt (1995) model atmospheres which form the basis of the G97 calibration. Those atmospheres are computed using scaled solar metallicities. However, Ruan's (1991) spectroscopic analysis of VB 12 (and HD 219617) indicates that both stars have the expected oxygen- and α-enhancement, and that changing the abundance ratios has a significant effect on the colors. Baraffe et al. (1997) have argued that the appropriate method of comparing stellar interior models (as well as stellar atmosphere models) for the M-subdwarfs is to consider $[m/H] \approx [O/H] = [Fe/H] + [O/Fe] \approx [Fe/H] + 0.35$ for $[Fe/H] \leq -1$. They find that the Monet et al. (1992) esdM are consistent with an average $[m/H] \sim -1.3$ or -1.5 based upon the $(M_V, V - I)$ HR diagram, whereas G97 found $[m/H] \sim -2 \pm 0.5$ for the same stars on the basis of spectroscopy. The discrepancy between the two calibrations is thus at least 0.5 dex.

Since the publication of Gizis' analysis, Reid (1997a) and Gratton et al (1997) have used main-sequence fitting to re-derive distances to a number of well-known clusters, using nearby F & G subdwarfs with high-precision Hipparcos parallax measurements as local calibrators. The resultant distances are significantly higher for the lowest abundance clusters (such as M92, M15 and NGC 6397). We can compare the re-calibrated cluster color-magnitude diagrams against the (M_V, (V-I)) distribution of

[2]Neither of the other systems has a reliable trigonometric parallax measurement

the local M subdwarfs. In Figure 3.3, we plot the parallax subdwarfs classified by Gizis (1997). We readjust published globular cluster main sequences to the distances and reddenings used by Reid (1997a, 1997b). We use the clusters NGC 6397 (Cool et al. 1996), M15 (Santiago, Elson, & Gilmore 1996), and 47 Tuc (Santiago, Elson, & Gilmore 1996). The metallicities ($[Fe/H]$) for these clusters are -1.82, -2.12, and -0.70 respectively (Carretta & Gratton 1997).[3] NGC 6397's main sequence passes through the esdM sequence. M15 lies at the bottom edge of esdM distribution, although the HST data do not extend very far to the red. As in G97, 47 Tuc lies above the sdM, indicating that they have $[m/H] < -0.7$. Thus, an empirical calibration suggests that the G97 M subdwarf abundance scale is consistent with the globular cluster $[Fe/H]$ scale.

3.4 Summary

We have compared the metallicities estimated directly from spectra of three M subdwarfs to the metallicities derived for their FGK subdwarf companions. We find that the metallicities based on the Gizis (1997) spectroscopic classification system are consistent with the metallicities derived by Carney et al. (1994) from high-resolution spectra. We argue that $[m/H]$ on the G97 scale corresponds to $[m/H] \approx [Fe/H]$.

Acknowledgments

We thank the Palomar Observatory staff for their capable support. JEG gratefully acknowledges support by Greenstein and Kingsley Fellowships as well as NASA grants GO-06344.01-95A and GO-05913.01-94A. This research has made use of the Simbad database, operated at CDS, Strasbourg, France.

[3]The Baraffe et al. (1997) $[m/H] = -1.3$ and -2 tracks are also plotted. With the new distances, the best fitting model for NGC 6397 is now $[m/H] = -1.3$ rather than -1.5.

Bibliography

Allard, F., & Hauschildt, P.H. 1995, ApJ, 445, 433

Axer, M., Fuhrmann, K., Gehren, T. 1994, A&A, 291, 895

Baraffe, I., Chabrier, G., Allard, F., & Hauschildt, P.H. 1995, ApJ, 446, L35

Baraffe, I., Chabrier, G., Allard, F., & Hauschildt, P.H. 1997, A&A, in press

Bessell, M.S. 1990, A&AS, 83, 357

Carney, B.W., Latham, D.W., Laird, J.B., & Aguilar, L.A. 1994, AJ, 107, 2240 (CLLA)

Carretta, E., & Gratton, R.G. 1997, A&AS, 121, 95

Cool, A.M., Piotto, G., King, I.R. 1996, ApJ, 468, 655

Gizis, J.E. 1997, AJ, 113, 806 (G97)

Gratton, R.G., Fusi Pecci, F., Carretta, E., Clementini, G., Corsi, C.E., & Lattanzi, M. 1997, ApJ, in press

Gunn, J.E., & Oke, J.B. 1983, ApJ, 266, 723

Heintz, W.D. 1991, A&AS, 90, 311

Laird, J.B., Carney, B.W., & Latham, D.W. 1988, AJ, 95, 1843

Latham, D.W., Mazeh, T., Stefanik, R.P., Davis, R.J., Carney, B.W., Krymolowski, Y., Laird, J.B., Torres, G., & Morse, J.A. 1992, AJ, 104, 774

Marcy, G.W., & Benitz, K.J. 1989, ApJ, 344, 441

Martin, E.L., & Rebolo, R. 1992, Complementary Approaches to Double & Multiple Star Research, IAU Colloquium 135, eds. Harold A. McAlister & William I. Haprtkopf, ASP Conference Series Vol. 32, p. 336

Martin, E.L., Rebolo, R., Zapatero Osorio, M.R. 1995, The Bottom of the Main Sequence – & Beyond, ed. C.G. Tinney (Springer, Berlin), p. 253

Monet, D.G., Dahn, C.C., Vrba, F.J., Harris, H.C., Pier, J.R., Luginbuhl, C.B., & Ables, H.D. 1992, AJ, 103, 638

Reid, I.N. 1997a, AJ, 114, 161

Reid, I.N. 1997b, AJ, submitted

Reid, I.N., Gizis, J.E., Cohen, J., Pahre, M., Hogg, D., Cowie, L., Hu, E., & Songaila, A. 1997, PASP, in press

Reid, I.N., Hawley, S.L., & Gizis, J.E. 1995, AJ, 110, 1838

Ruan, K. 1991, Ph.D. Thesis, The Australian National Observatory

Ryan, S.G. 1992, AJ, 104, 1144

Santiago, B.X., Elson, R.A.W., & Gilmore, G.F. 1996, MNRAS, 281, 1363

Van Briesbroeck, G. 1961, AJ, 66, 528

Table 3.1: Spectroscopic Indices

Band	S1	W	S2
TiO 5	7042-7046	7126-7135	
CaH 1	6345-6355	6380-6390	6410-6420
CaH 2	7042-7046	6814-6846	
CaH 3	7042-7046	6960-6990	

Table 3.2: Data for Binary Systems

Star	V	V-I_C	Src	Sep ($''$)	$[m/H]_p$
	TiO5	CaH1	CaH2	CaH3	Sp. Type
G 116-009B	18.4	2.0	MR	10.2	-1.46
	0.93	0.83	0.65	0.84	sdM0.5
G 176-046D	18.0	2.2	MR	4.7	-1.07
	0.76	0.80	0.63	0.83	M 1.0 V
VB 12	16.46	2.09	B	15	-1.40
	0.71	0.60	0.44	0.65	sdM3.0

Photometry sources are MR (Martin & Rebolo 1992; Martin et al. 1995) and B (Bessell 1990).

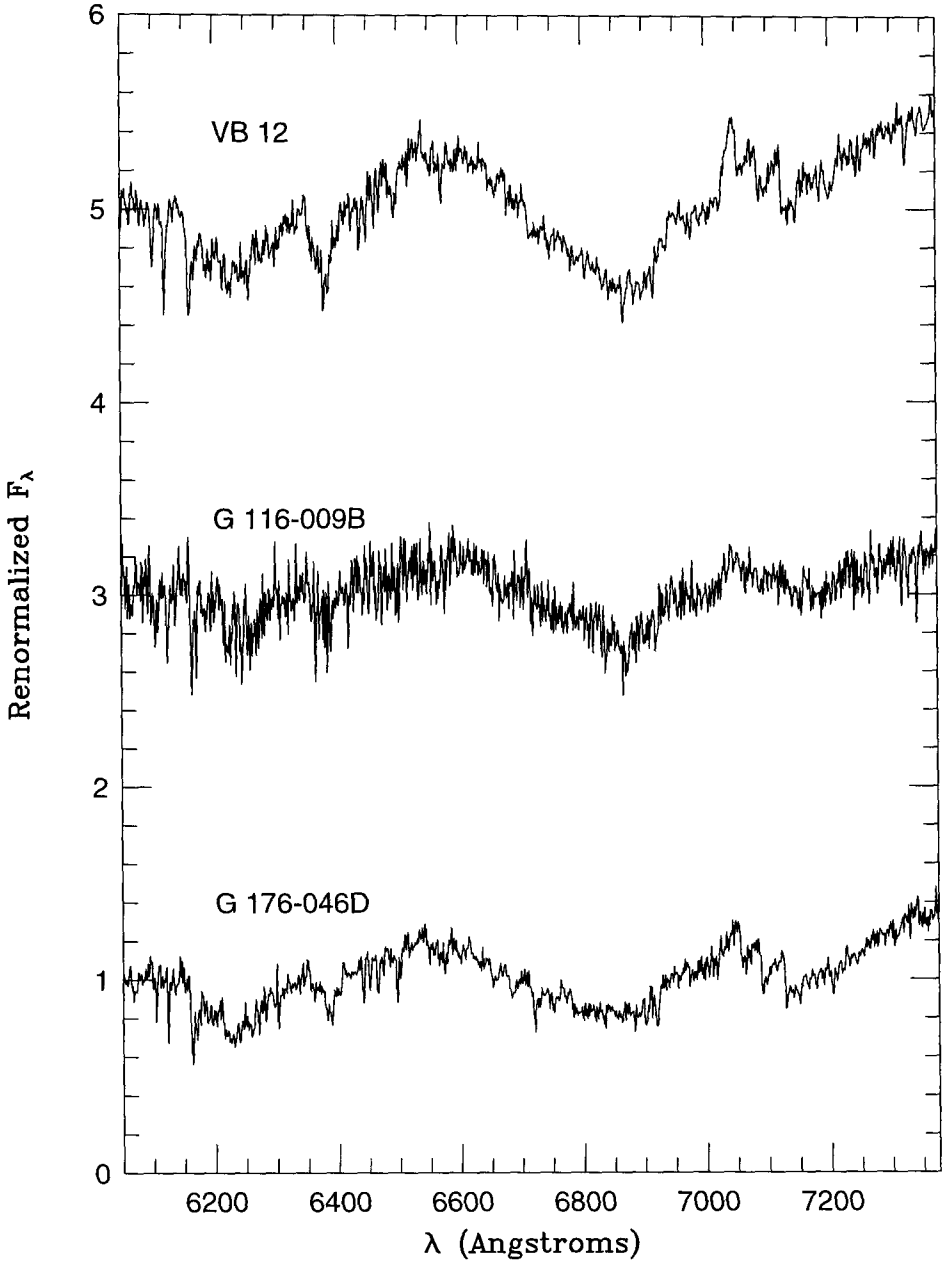

Figure 3.1: Spectra of the three metal-poor M subdwarf companions. The spectra have been renormalized by a mean value of 1. G116-009B and VB 12 respectively have been displaced upwards by 2 and 4 respectively.

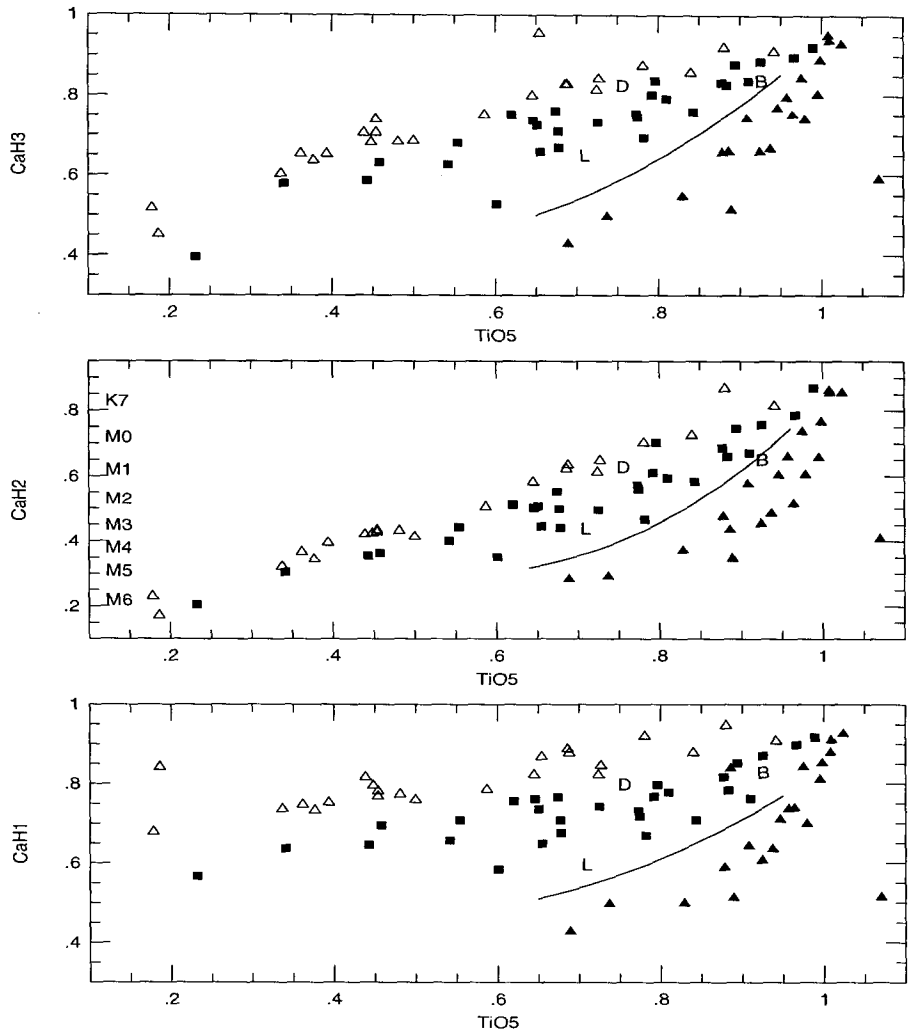

Figure 3.2: The TiO and CaH indices of the three low-luminosity companions (solid circles) are plotted with the Gizis (1997) values for high velocity M V (open triangles), sdM (solid squares), and esdM (solid triangles). The solid curves show the approximate boundary between sdM and esdM. LHS 541, G 116-009B , and G 176-046D are plotted as L, B, and D respectively. G176-046D lies close to the M V/sdM boundary. The sdM G 116-009B and VB 12 lie just above the esdM sequences.

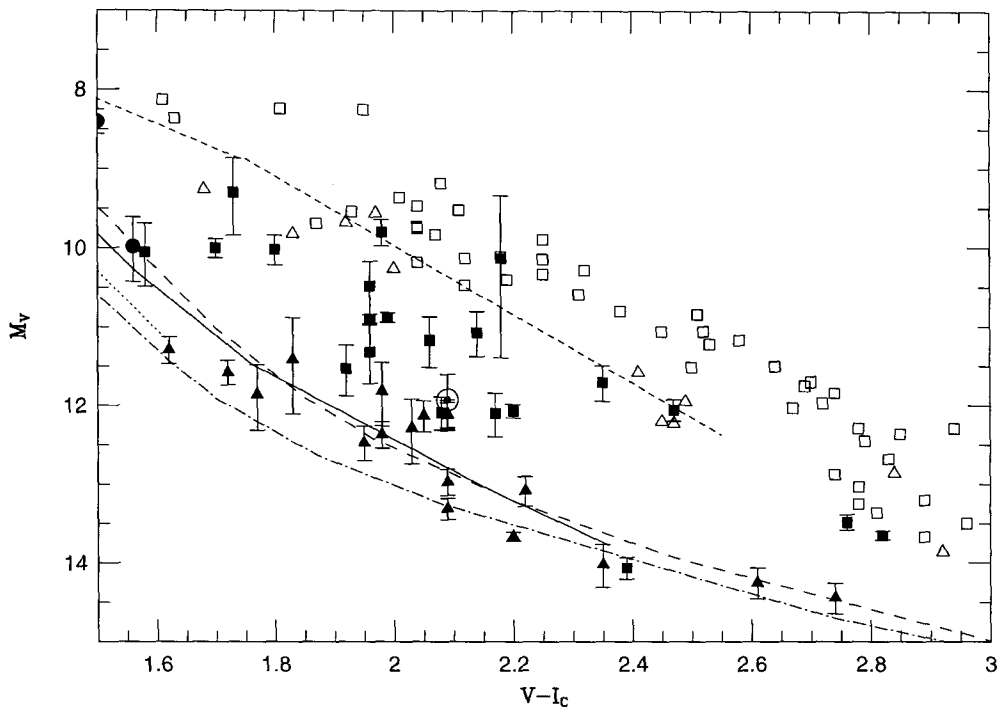

Figure 3.3: The HR Diagram of very low mass stars. Shown are the esdM (solid triangles), sdM (solid squares), high velocity M V (open triangles), and single nearby disk M V stars (open squares). VB 12 is the circled point at $M_V = 11.93, V-I = 2.09$. Also shown are the main sequences of three globular clusters: NGC 6397 (solid line, $[Fe/H] = -1.82$), M15 (dotted line, $[Fe/H] = -2.12$), and 47 Tuc (short dashed line, $[Fe/H] = -0.70$. The globular cluster main sequences use the Hipparcos-based distances of Reid (1997a,1997b). The recent model calculations of Baraffe et al. for $[m/H] = -2$ and -1.3 are plotted as long-dashed and dotted and as long-dashed lines respectively. The -1.3 model is in good agreement with NGC 6397.

Chapter 4 M-Subdwarfs: The Temperature Scale

4.1 Introduction

M subdwarfs are the metal-poor counterparts of the familiar M dwarfs of the Galactic disk. Although some M subdwarfs were identified half a century ago (Joy 1947), the extreme M subdwarfs were recognized relatively recently (e.g., Ake and Greenstein 1980) following Luyten's (1979) proper motion survey of faint red stars. Spectroscopically, M subdwarfs are classified by their weak TiO and strong hydrides (Gizis 1997, hereafter G97). Photometrically, they are distinguishable in the (J-H,H-K) and (B-V,V-I) diagrams (Mould and McElroy 1978; Leggett 1992; Dahn et al. 1995) and in (M_V,V-I) and (M_K,I-K) HR diagrams (Monet et al. 1992; Tinney et al. 1995). G97 used modern model atmospheres (Allard and Hauschildt 1995) to show that synthetic spectra and observations show a good match in the 6200 – 7300Å region, allowing the metallicities of these stars to be directly determined, to an systematic accuracy of $\sim$ 0.3 dex. G97 additionally showed that these estimates are consistent with Hubble Space Telescope observations of globular clusters, and are consistent with stellar structure calculations using the same model atmospheres (Baraffe et al. 1995). Additional observations of wide binaries allowed Gizis & Reid (1997b) to show that the G97 M subdwarf metallicities are consistent with the Carney et al. (1996) metallicities of FGK subdwarfs.

Although the metallicities are thus relatively well-constrained for M subdwarfs, little is known about the temperatures of these stars. This has probably been due to the uncertainty over the metallicities, the lack of reliable model atmospheres, and the difficulties in determining temperatures for the more common and brighter M dwarfs (Leggett et al. 1996, hereafter LABDH). All of these difficulties are now reduced,

although we must caution that the changes evident even between different generations of the same models for both the spectra (Kirkpatrick et al. 1993; LABDH) and the structure models (Baraffe et al. 1995; Baraffe et al. 1997) suggest that changes of 5%, and perhaps even 10%, cannot be ruled out for the current M dwarf temperature scale.

We present optical and infrared observations aimed at constraining the temperatures of cool metal-poor stars. In Section 4.2, we describe our optical spectroscopy and infrared photometry. In Section 4.3, we use our optical spectroscopy to derive synthetic filter photometry to investigate the effects of metallicity on optical photometry. In Section 4.4, we discuss the infrared color-color and HR diagrams of M subdwarfs. In Section 4.5, we derive the temperatures by comparing our data to model atmospheres. We summarize our conclusions in Section 4.6.

4.2 Data Analysis

4.2.1 Spectra

We obtained spectra using the Palomar 60-in. telescope and spectrograph (McCarthy 1985) on U.T. Dates 9 and 10 July 1996. The first night was photometric but the second night's observations were taken through clouds. We used the 150R grating ($\lambda_{Blaze} = 8000$Å) which provided wavelength coverage from 4600Å to 10170Å. Beyond 9900Å, the counts rapidly dropped off due to the lack of CCD sensitivity and telluric absorption. The wavelength calibration was computed using neon and arc lamps. The slit had a width of 4.65 arcseconds. The resolution, as determined by fitting gaussians to the arc lines, is $\sigma = 17.8$Å (2.5 pixels). The stellar observations have significantly better resolution since their resolution is set by the seeing rather than the slit. (The seeing was better than 1.5 arcseconds). The $H\alpha$ line of the flux standards has $\sigma = 6.0$Å (0.86 pixels), which we adopt as the instrumental resolution. This resolution is only used for the comparison of the spectra to model predictions. We used the standard FIGARO "Palomar" extinction corrections, which we found

gave better consistency for spectra observed at different airmasses than the "EXTIN" corrections (Hayes & Latham 1975).

Gunn & Oke (1983) flux standards were observed during the course of the nights and were used to flux calibrate the data. Our objectives for this program were to obtain spectrophotometry for the VRI bands. We therefore intended to use the GG455 order-blocking filter, which would have allowed all the V light through without contaminating the I band with blue second-order light. Analysis of the data, however, indicates that the GG-385 filter was used since second-order light clearly contaminates the blue flux standards beyond 7600Å. This second-order contamination is not important for the M dwarf stars themselves, since they are quite red. We therefore used the Gunn & Oke standards to flux calibrate the data, with the knowledge that an additional correction was then necessary beyond 7600Å. Dr. Kirkpatrick kindly provided M dwarf spectra (Kirkpatrick et al. 1991; Henry et al. 1994) covering the wavelength range $\sim$ 6400 to $\sim$ 9200Å. These spectra have the correct shape (but not the correct absolute flux level). There are 25 stars in common. We found that a single correction was able to bring the shape of all our M dwarf spectra into agreement with Kirkpatrick's spectra. We therefore are confident that the blue second-order light leak does not affect our program objects. Beyond 9200Å we do not have any data suitable for recalibrating our spectra. In addition, there are broad telluric absorption features in this region which affect any attempt at photometry. We have applied a simple linear correction to the redmost ($\lambda > 9000$Å) data to make the unabsorbed regions flat in F_λ vs. λ for an M4 star, as the data plotted by Leggett et al. (1996) suggest. We cannot, however, consider this region of the spectrum to be suitable for photometric purposes.

4.2.2 Infrared Photometry

We obtained infrared photometry of the program stars using the Las Campanas Swope 40-in. The IR camera, which uses a NICMOS3 detector, has nearly identical design to the IR camera of the Palomar 60-in. telescope (Murphy et al. 1995). The 256 $\times$ 256

chips have scales of 0.619″ pixel^{-1} (Palomar) and 0.599″ pixel^{-1} (Las Campanas). Each star was observed at 5 different positions, each selected to avoid regions with bad pixels. The new faint IR standards for HST (Persson, private communication) were observed throughout each night. These fainter standards are on the "CIT" system of Elias et al. (1982) but lie in a magnitude range ($10.9 < J < 12.4, 10.6 < H < 12.2, 10.5 < Ks < 12.1$) that will not saturate the detector in 10-15 second exposures. Note that the seeing was excellent ($< 1''$) and therefore the PSF was moderately undersampled. Most of our target stars are fainter than the standards, and we therefore used longer (30 second) exposures at each position, with up to four images taken at each position. The standards were photometered through a 10″ radius aperture. It should be noted that the "J" filter used at both telescopes for both our project and the definition of the standards is a "J-short" filter. There is, however, no evidence of significant differences from standard "J" filters (Persson et al. 1998, in preparation)

The data were linearized, dark-subtracted, flat-fielded, and sky-subtracted using IRAF scripts developed by M. Pahre. We found that we obtained the best results using flatfields made from sky images taken during the night. The photometry of the standards shows a scatter of ± 0.02 magnitudes for the Las Campanas data. The resulting photometry is listed in Table 4.6. The quoted uncertainties for the Las Campanas include the poisson uncertainties and the observed scatter of ± 0.03 magnitudes for the standards. We note, however, that the three stars (LHS 211, LHS 216, and LHS 1970) in common with the study of Leggett (1992) are ~ 0.06 magnitudes fainter in all three colors. LHS 211 was measured on two different nights with magnitudes that agreed to within 0.02 magnitudes in all three bandpasses. Table 4.6 also includes G97's spectral classifications. LHS 1691 and LHS 2045 have been classified esdM on the basis of the spectra presented by Kirkpatrick et al. (1995).

4.3 Synthetic Colors

We have used our flux-calibrated spectra to derive VRI filter photometry. Our interest is to determine whether metallicity significantly affects VRI photometry for M dwarfs. The photometry in the literature (see Gizis 1997 for a compilation) cannot answer this question as most of it has required significant color transformations to place on the Cousins system; in any case, some metal-poor stars appear to strongly deviate from near-solar metallicity color-color relations, others do not. Derivation of photometry also tests our flux calibration. Bessell (1990b) has determined the passband response for the Johnson V and Kron-Cousins RI system. We also use the Bessell (1986) passband response for photographic III-aF plates (R_{59F} and R_{63F}). In Figure 4.1, we plot our observation of Barnard's Star with the bandpass responses superimposed.

We take the zeropoints of the magnitude system to be the star Vega. We use the Vega spectrum of Hayes (1985). The magnitude is then

$$mag = -2.5 \times \log_{10} \left(\frac{C \times \int F_\lambda(star) \times T_\lambda d\lambda}{\int F_\lambda(Vega) \times T_\lambda d\lambda} \right) \tag{4.1}$$

where mag is the observed apparent magnitude, F_λ is the observed spectrum, T_λ is the passband response, and C is a constant that corrects the observed flux to the true flux. For photometric conditions, as in our first night, C should be one, but for non-photometric conditions C will be greater than one. If the shape of the spectrum has been correctly determined, then the same value C should apply for all bandpasses for a given spectrum. Thus colors can be correctly determined for all of our observed spectra.

We first consider the standard VRI_C photometry determined from our spectra. In Figure 4.2, we plot R-I_C vs. V-I_C. Four features are worthy of note. First, both the non-photometric and photometric data follow the same relation. Second, our data are in agreement with a sixth-order polynomial fit to the Bessell (1990a) photometry of Gliese catalog stars. These two facts together show that our spectra are correctly flux calibrated. Third, twelve of the fourteen sdM and the three esdM lie on the same

relation defined by the ordinary M dwarfs. There are two outliers, which apparently have poorly calibrated spectra: LHS 491, classified as sdM1.5, and LHS 536, classified as sdM0.5. We conclude on the basis of the majority of the spectra that there is no significant deviation from the disk $V-I_C, R-I_C$ relationship due to metallicity for the sdM stars. An independent test is the sdM1.0 Kapteyn's Star (LHS 29; Gl 191) for which Bessell (1990a) measured $R-I=0.995, V-I=1.95$. The discrepancy from the value predicted by the polynomial fit is 0.015 magnitudes which is not significant.

Another filter system of interest for low-mass stars is the "Palomar" system established by Tinney, Reid & Mould (1993, hereafter TRM) for their measurement of the disk luminosity function and later used by Gizis & Reid (1998, in prep.) for their measurement of the halo luminosity function. TRM's system was well-calibrated for near-solar metallicity stars, but for halo stars the possibility of color terms must be investigated. This system used a CCD with Gunn R and I filters to calibrate Cousins R and I standards. A transformation with a significant $R-I$ color term was found. The CCD data was then used to calibrate photographic data using IIIaF (with RG590, 610, or 630 filters) and IVN emulsions. The CCD-to-Photographic color term reached 0.5 magnitudes at $r-i_P=2.0$, while the CCD-to-Cousins transformation was only 0.02 magnitudes at $R-I_C=2.0$. We adopt the Gunn bandpass response given by Bessell (1986). We find that we are unable to reproduce the TRM transformations, in the sense, that we predict a larger CCD-to-Cousins color term and a smaller CCD-to-Photographic term. Since, however, we find that the overall magnitude and sign of the color term between the Cousins system and the photographic data is reproduced, we believe that the question of the metallicity dependence can be answered. We find that the metal-poor stars can be calibrated photometrically on the VRI system using the same transformation as for disk stars.

4.4 Infrared Magnitudes

In Figure 4.3, we plot the infrared color-color diagram for the stars observed at Las Campanas. In addition to our own data, we use infrared photometry from Leggett

(1992), Ruiz & Anguita (1993), and LABDH and the optical photometry compiled by G97. Also shown on the same diagram is the disk sequence for dwarf and giant stars determined by Bessell & Brett (1988) and Leggett's (1992) metallicity classifications of M dwarfs into Young Disk (YD), Old Disk (OD), Halo (H), and two intermediate classifications (Y/O, H/O). Most of Leggett's H stars are "M V" and "sdM" stars according to the G97 classification system. Our observations include mostly esdM stars. The few "M V" high-velocity stars that we observe lie either in the OD (LHS 3684) or at the edge of the H region (LHS 2110) which is consistent with the G97 and Reid, Hawley & Gizis (1995) classifications of Leggett's sample and the observational uncertainties. A few stars have IR colors that are inconsistent with their classifications; given the number of stars and relatively large error bars, some such objects are expected. We find, however, that most of the esdM lie well into Leggett's Halo region.

We also plot the HR diagram using V-K and I-K in Figure 4.4. As previously noted by Tinney et al. (1995), the I-K, M_K diagram main sequence is nearly vertical for the most extreme subdwarfs and is consistent with Allard & Hauschildt's $[m/H] = -1.5$ models. The models of Baraffe et al. (1997, hereafter BCAH97) are consistent with $[m/H] = -1.3$ or -1.5.

4.5 Temperature Scale

The effective temperature of a star is defined as

$$L = 4\pi R^2 \sigma T_{eff}^4 \tag{4.2}$$

Unfortunately, there are no direct measurements of the radius (R) for M subdwarfs, so there is no way to derive T_{eff} directly from observations at present. Comparison of synthetic spectra from model atmosphere calculations to observations provides an alternative way of estimating effective temperatures. These results must be viewed with caution, since there are significant uncertainties in the model calculations (as

reviewed by Allard et al. 1997) and significant discrepancies with, for example, the infrared JHK diagram (Leggett 1992). Despite these uncertainties, synthetic spectra based upon the "Extended" Allard & Hauschildt (1995, hereafter AH) models give remarkably good fits to moderate (3Å) resolution spectra in the wavelength range 6200 – 7400Å, allowing an estimate of the metallicity (Gizis 1997, hereafter G97). These fits also provide an estimate of the effective temperature, but as the wavelength range covered is not very large, those estimates are necessarily uncertain. Our new data provides much better wavelength coverage, allowing a new derivation of the effective temperatures of M subdwarfs. We will compare two different sets of data to the models: the optical (VRI) spectrophotometry and the broadband (VIJHK) colors.

In Figures 4.5 and 4.6, we plot our spectra according to the G97 classifications. For comparison, we also plot in Figure 4.7 an M V sequence based upon the Kirkpatrick et al. (1991) classification system. The G97 numerical subclasses are based upon the strength of the CaH feature at 6900Å. Numerical subclasses are useful insofar as they distinguish between stars of differing temperature which have noticeable observational differences. Since the M V, sdM, and esdM stars have differing compositions, they will have different spectral energy distributions even at the same effective temperature. As noted by G97, it might be ideal if a numerical subclass system could be devised that corresponded to effective temperature, so that M3.0 V, sdM3.0, and esdM3.0 all had the same temperatures. This, however, is impractical since the effective temperature scale is still uncertain; in any case, such a procedure would perhaps be unwise since spectral types should be based upon purely observational criteria rather than theory. The G97 spectral subtypes are chosen in a well-defined observational manner, but since they are based on particular absorption features, the overall spectral energy distributions will differ significantly. Examination of Figures 4.5 and 4.7, reveals that the overall slope of the sdM4.5 spectrum is quite close to the M4.0 V star (note, however, that this is Barnard's Star), and that of the sdM3.5 star is close to the M2.5 V star. Thus classification based on spectra such as the ones in this paper must pay careful attention to the absorption features (CaH,MgH) which are enhanced and

the features (TiO) which are weaker in the sdM spectra before assigning a numerical subclass based upon the slope (or overall shape) of the spectrum.

We first estimate effective temperatures by comparing our low-resolution spectra to the AH95 synthetic spectra. Kirkpatrick et al. (1993) compared their low-resolution optical and infrared spectra to an earlier generation of Allard models by minimizing the least-squares fit. LABDH compared their optical and infrared spectra to more recent AH95 models by evaluating the fits by eye. Here, we minimize the least-squares difference. For each star, we fix the metallicity to that determined in G97. For the sdM, the fits from the low-resolution spectra give the same temperatures as those determined in G97 to $\pm$100 K. We do not, however, have low-resolution spectra of any extreme M subdwarfs later than subclass esdM0. In Figure 4.8, we plot the spectrum with the best fit model for the sdM1.5 star LHS 482. It is clear that these models have certain absorption bands that are too strong compared to the observation. There appears to be some tendency for the I band flux to be underestimated. Indeed, it appears that the best region of agreement is the 6000 – 7500Å region used by G97.

We also estimate temperatures by fitting the observed VIJHK photometry to the model atmosphere predictions. For each star, we compute the least squares difference between the observed magnitudes and predicted magnitudes for each model temperature, as follows:

$$D = \sum_{i=V}^{K} [M_i^o - (m_i^m + a)]^2 \tag{4.3}$$

where i represents each of the VIJHK filters, M_i^o is the observed absolute magnitude, M_i^m is the model magnitude, and a is a constant chosen to minimize this sum for this particular model. The best fit model is the one with the minimum value of D. We improve this estimate of the temperature by interpolating between the models using a parabolic fit to D. Specifically,

$$T_{best} = T_1 - \frac{1}{2} \frac{(T_1 - T_0)^2[D(1) - D(2)] - (T_1 - T_2)^2[D(1) - D(0)]}{(T_1 - T_0)[D(1) - D(2)] - (T_1 - T_2)[D(1) - D(0)]} \tag{4.4}$$

where 1 indicates the best fit model, 0 indicates the next cooler model, and 2 indicates the next hotter model. (We have also repeated this procedure using the absolute value of the difference instead of the square in equation 4.3 — the best fit model is always the same, and the temperature estimated by Equation 4.4 changes by < 10 K).

There are two interesting sets of models available to us. The model colors for the Extended grid have already been calculated by Allard & Hauschildt (1995). More recent models, however, are available in the form of the stellar interior models calculated by BCAH97 for metal-poor stars. The latter calculations use the "NextGen" calculations of Allard & Hauschildt (1997). We take the differences between these two generations of models to be illustrative of the systematic errors that are likely, although this may be a pessimistic assumption. (As noted in Gizis & Reid 1997b, the differences are substantial for the stellar structure predictions of the HR diagram). We compare, in turn, the Extended models to the apparent magnitudes (allowing a of Equation 4.3 to vary), the BCAH97 models to the absolute magnitudes (allowing a to vary), and the BCAH97 models to the absolute magnitudes (keeping a fixed). The BCAH97 models are only available for $[m/H] \leq -1$.

We first consider the results of this procedure for solar metallicity stars. We consider the 95 spectral standards of Kirkpatrick et al. (1991, 1995) that have Leggett (1992) photometry. At each spectral type, we average all the determinations. The results are plotted in Figure 4.9. Our results are in remarkably close agreement with the results of LABDH in the range M3 to M6.5 — our temperatures are $\lesssim 100$ K hotter at a given spectral type, which is a 3% discrepancy. LABDH have shown that their temperature scale improves the agreement with theoretical models. For spectral types earlier than M3 V, the model effective temperatures are definitely too hot in this generation of models, and has been shown to be due to treatment of TiO opacities (Bessell 1995; Allard et al. 1997). This discrepancy is obvious from the spectra, which have very strong molecular absorption, and may be less important in the metal-poor ($[m/H] \leq -1$ models which show weaker absorption. We fit the eclipsing binary CM Dra (LHS 421) with a slightly metal-poor model ($[m/H] = -0.5$). We find a temperature of 3213 K (solar metallicity fits give $T_{eff} = 3371$ K), which compares

favorably with Bessell's observational value of 3100 ± 150 K (Bessell 1995; Habets & Hentze 1981; Lacy 1977). We conclude on the basis of the good agreement with LABDH's fits and the CM Dra measurement that our fitting procedure yields realistic temperatures.

We next consider the sdM and esdM. The results are listed in Table 4.6 and 4.6, where we report only the spectral fits of G97, the Extended model IR fits to the same metallicity models as G97 fit, and the IR fits to BCAH97 (with a varying) for $[m/H] = -1.0$ (for sdM) and $[m/H] = -1.5$ (for esdM). The following results are notable. First, the BCAH97 $[m/H] = -2.0$ models are generally $\sim$ 1 magnitude fainter than the esdM observations, while the $[m/H] = -1.3$ models give better agreement with the esdM — this result is consistent with BCAH97's analysis of the $V-I, M_V$ diagram. Indeed, the BCAH97 $[m/H] = -1.3$ models give better fits (i.e., D is smaller) than the -2.0 models. The BCAH97 $[m/H] = -1.5$ models give the best fits to the esdM, which is consistent with Figure 3 of Gizis & Reid (1997b). There are four esdM2.5 – esdM3.0 (LHS 3382, 1970, 1174, and 3548) in our sample. The G97 spectra give a best fit of 3500K and $[m/H] = -1.5$. For the extended models, we find best fit temperatures in the range $3456 - 3516$ K from the photometry, consistent with G97. The BCAH97 $[m/H] = -1.5$ models give only slightly lower temperatures, $3420 - 3475$K. Thus, the estimate of $\sim$ 3500 K for these stars is supported by the photometry. The cooler esdM are somewhat discrepant: for the stars LHS 205a and 1742a, the G97 results give $[m/H] = -2.0, T_{eff} = 3400$K and 3300 K. Comparison of the Extended models and the photometry yield 3154K and 2982 K respectively. Use of the BCAH97 gives temperatures in the range $3135 - 3300$ K for 205a and $2938 - 3110$ K for 1742a, depending upon the metallicity and whether a is allowed to vary.

4.6 Conclusions

We have obtained low-resolution optical spectroscopy and infrared photometry of a sample of M subdwarfs.

We show that metallicity terms are unlikely to affect VRI photometry for the sdM and earliest esdM stars. The sdM stars lie on the $V - I_C, R - I_C$ sequences defined by near-solar metallicity stars. We present optical/near-infrared HR diagrams that confirm that the main sequence for the esdM is vertical in $I - K, M_K$.

We show that the comparison of broadband VIJHK colors to model predictions leads to a temperature scale for M dwarfs that is similar to that obtained using optical and near-infrared spectra but $\sim$ 3% hotter. We use the same technique to derive temperatures for the sdM and esdM stars. We find that this technique suggests that the coolest esdM stars are a few hundred degrees cooler than the G97's spectral fits suggested. Specifically, LHS 1742a is probably $\sim$ 3000 K. This suggests a mass of $0.09 M_\odot$ according to the BCAH97 models.

Acknowledgments

Skip Staples and Rick Barnes gave, as always, invaluable assistance at the telescope. I am indebted to Neill Reid for his advice, Davy Kirkpatrick for providing access to his spectra, and Eric Persson and Mike Pahre for their invaluable advice on infrared observations. I gratefully acknowledge support by Greenstein and Kingsley Fellowships as well as NASA grants GO-06344.01-95A and GO-05913.01-94A. This research has made use of the Simbad database, operated at CDS, Strasbourg, France.

Bibliography

Ake, T.B., & Greenstein, J.L. 1980, ApJ, 240, 859

Allard, F., & Hauschildt, P.H. 1995, ApJ, 445, 433

Allard, F., & Hauschildt, P.H. 1997, in preparation

Allard, F., Hauschildt, P.H., Alexander, D.R., & Starrfield, S. 1997, ARAA, in press

Baraffe, I., Chabrier, G., Allard, F., & Hauschildt, P.H. 1995, ApJ, 446, L35

Baraffe, I., Chabrier, G., Allard, F., & Hauschildt, P.H. 1997, A&A, in press

Bessell, M.S. 1986, PASP, 98, 1303

Bessell, M.S. 1990a, A&AS, 83, 357

Bessell, M.S. 1990b, PASP, 102, 1181

Bessell, M.S. 1995, The Bottom of the Main Sequence – And Beyond, edited by C.G. Tinney (Berlin, Springer), p. 123

Bessell, M.S., & Brett, J.M. 1988, PASP, 100, 1134

Carney, B.W., Laird, J.B., Latham, D.W., & Aguilar, L.A. 1996, AJ, 112, 668

Dahn, C.C., Liebert, J., Harris, H.C., & Guetter, H.H. 1995, The Bottom of the Main Sequence – And Beyond, edited by C.G. Tinney (Berlin, Springer), p.239

Elias, J.H., Frogel, J.A., Matthews, K, & Neugebauer, G. 1982, AJ, 87, 1029

Gizis, J.E. 1997, AJ, 113, 806 (G97, Chapter 2)

Gizis, J.E., & Reid, I.N. 1997, PASP, 109, 849

Gizis, J.E., & Reid, I.N. 1997, PASP, in press (Chapter 5)

Gunn, J.E., & Oke, J.B. 1983, ApJ, 266, 723

Habets, G.M.H.J., & Heintze, J.R.W. 1981, A&AS, 46, 193

Hawley, S.L., Gizis, J.E., & Reid, I.N. 1996, AJ, 112, 2799

Hayes, D.S. 1985, Proceedings IAU Symposium No. 111, "Calibration of Fundamental Stellar Quantities", ed. D.S. Hayes, E. Pasinetti & A.G.D. Philip (Dordrecht: Reidel), p. 225

Hayes, D.S., & Latham, D.W. 1975, ApJ, 197, 593

Henry, T.J., Kirkpatrick, J.D., & Simons, D.A. 1994, AJ, 108, 1437

Joy, A.H. 1947, ApJ, 105, 96

Kirkpatrick, J.D., Henry, T.J., McCarthy, D.W. 1991, ApJS, 77, 417

Kirkpatrick, J.D., Kelly, D.M., Rieke, G.H., Liebert, J., Allard, F., & Wehrse, R. 1993, ApJ, 402, 643

Kirkpatrick, J.D., Henry, T.J., Simons, D.A. 1995, AJ, 109, 797

Lacy, C.H. 1977, ApJ, 218, 444

Leggett, S.K. 1992, ApJS, 82, 351

Leggett, S.K., Allard, F., Berriman, G., Dahn, C.C., & Hauschildt, P.H. 1996, ApJS, 104, 117

Luyten, W.J. 1979, Catalogue of Stars With Proper Motions Exceeding 0."5 Annually (LHS), (University of Minnesota, Minneapolis, Minnesota)

McCarthy, J.K. 1985, Proc. SPIE, 554, 155

Monet, D.G., Dahn, C.C., Vrba, F.J., Harris, H.C., Pier, J.R., Luginbuhl, C.B., & Ables, H.D. 1992, AJ, 103, 638

Mould, J.R., & McElroy, D.B. 1978, ApJ, 220, 935

Murphy, D.C., Persson, S.E., Pahre, M.A., Sivaramakrishnan, A., & Djorgovski, S. G. 1995, PASP, 107, 1234

Reid, I.N., Hawley, S.L., & Gizis, J.E. 1995a, AJ, 110, 1838

Ruiz, M.T., & Anguita, C. 1993, AJ, 105, 614

Tinney, C.G., Reid, I.N., Gizis, J. & Mould, J.R., 1995, AJ, 110, 3014

Tinney, C.G., Reid, I.N., & Mould, J.R. 1993, AJ, 105, 1045

Table 4.1: IR Photometry

Star	J	σ_J	H	σ_H	Ks	σ_{Ks}	M_{Ks}	Sp. Type
LHS 161	11.69	0.03	11.17	0.03	10.99	0.03	8.06	esdM2.0
LHS 185	12.36	0.03	11.76	0.03	11.56	0.03	7.67	esdM0.5
LHS 192	14.25	0.03	13.75	0.04	13.56	0.05	8.60	esdM1.0
LHS 205a	15.43	0.05	14.80	0.07	14.66	0.10	9.75	esdM4.5
LHS 211	11.22	0.03	10.69	0.03	10.49	0.03	6.78	sdM0.0
LHS 216	11.39	0.03	10.86	0.03	10.65	0.03	8.02	sdM2.5
LHS 218	11.05	0.03	10.51	0.03	10.28	0.03	7.64	M3.5 V
LHS 232	11.52	0.03	11.00	0.03	10.86	0.03	6.71	
LHS 272	9.59	0.03	9.11	0.03	10.06	0.03		sdM3.0
LHS 301	9.73	0.03	0.00	0.00	10.28	0.03	8.94	M3.5 V
LHS 522	11.60	0.03	11.08	0.03	10.92	0.03	8.06	esdK7
LHS 1174	13.77	0.03	13.25	0.03	13.07	0.03	9.05	esdM3.0
LHS 1691	14.25	0.03	13.60	0.03	13.39	0.04		esdM
LHS 1742a	14.64	0.04	14.27	0.05	14.08	0.06	9.72	esdM5.5
LHS 1970	14.58	0.03	14.16	0.04	13.94	0.05	9.34	esdM2.5
LHS 2045	14.80	0.03	14.33	0.04	14.12	0.04	9.35	esdM
LHS 2110	12.64	0.03	12.17	0.03	11.90	0.03	7.79	M4.0 V
LHS 2204	11.89	0.03	11.38	0.03	11.09	0.03	8.39	
LHS 3684	13.54	0.03	12.99	0.03	12.73	0.03	8.64	M4.5 V
LHS 4037	10.98	0.03	11.28	0.03	11.16	0.03		

Table 4.2: Temperature Fits: esdM

LHS	Sp. Type	T_{eff} (G97)	T_{eff} Extended	T_{eff} BCAH97
161	esdM2.0	3600	3484	3537
3382	esdM2.5	3500	3516	3405
1970	esdM2.5	3500	3433	3420
1174	esdM3.0	3500	3456	3437
3548	esdM3.0	3500	3456	3437
375	esdM4.0	3400	3001	3209
205a	esdM4.5	3400	3154	3270
1742a	esdM5.5	3300	2982	2938

Table 4.3: Temperature Fits: sdM

LHS	Sp. Type	T_{eff} (G97)	T_{eff} Extended	T_{eff} BCAH97
467	sdMK7	···	4000	3764
12	sdM0.0	···	4000	3788
211	sdM0.0	···	3736	3654
307	sdM0.5	3700	4000	3888
29	sdM1.0	3700	3559	3585
482	sdM1.5	3600	3591	3534
216	sdM2.0	3600	3508	3440
20	sdM2.5	3600	3417	3373
407	sdM5.0	3400	3347	3302
377	sdM7.0	3200	2890	2840

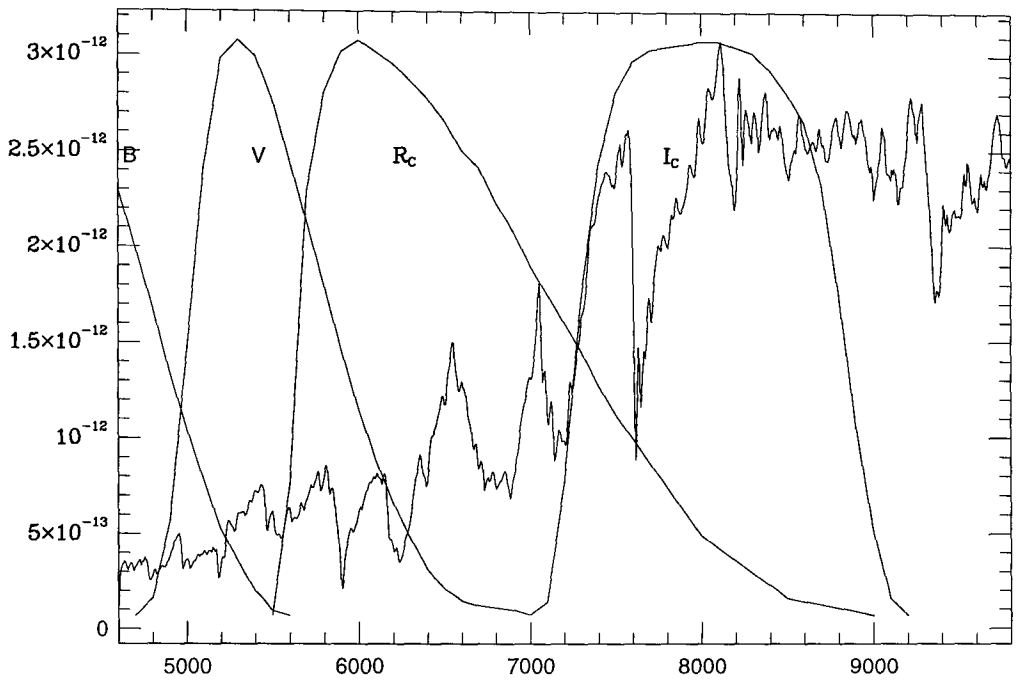

Figure 4.1: Our spectrum of Barnard's Star (LHS 57; Gl 699) with the response of the $BVRI_C$ filters.

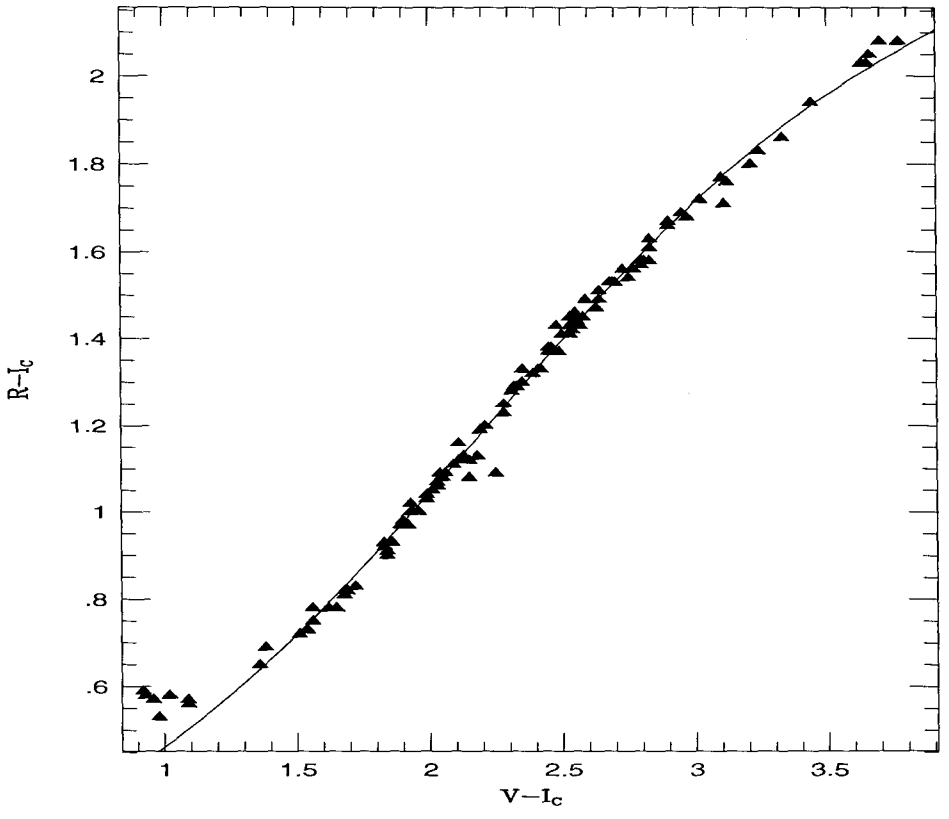

Figure 4.2: The V-I_C and R-I_C colors determined from our spectra. Our data is shown as solid triangles. Also shown is a polynomial fit to Bessell's (1990a) photometry of nearby stars. The agreement between the spectrophotometry and Bessell's photometry is excellent and indicates that our flux calibration is correct. No offset between the data obtained on the non-photometric night and the photometric night is evident. There does not appear to be any offset between the sdM or esdM and the ordinary M dwarfs. The two outliers (LHS 491 and LHS 536) are discussed in the text.

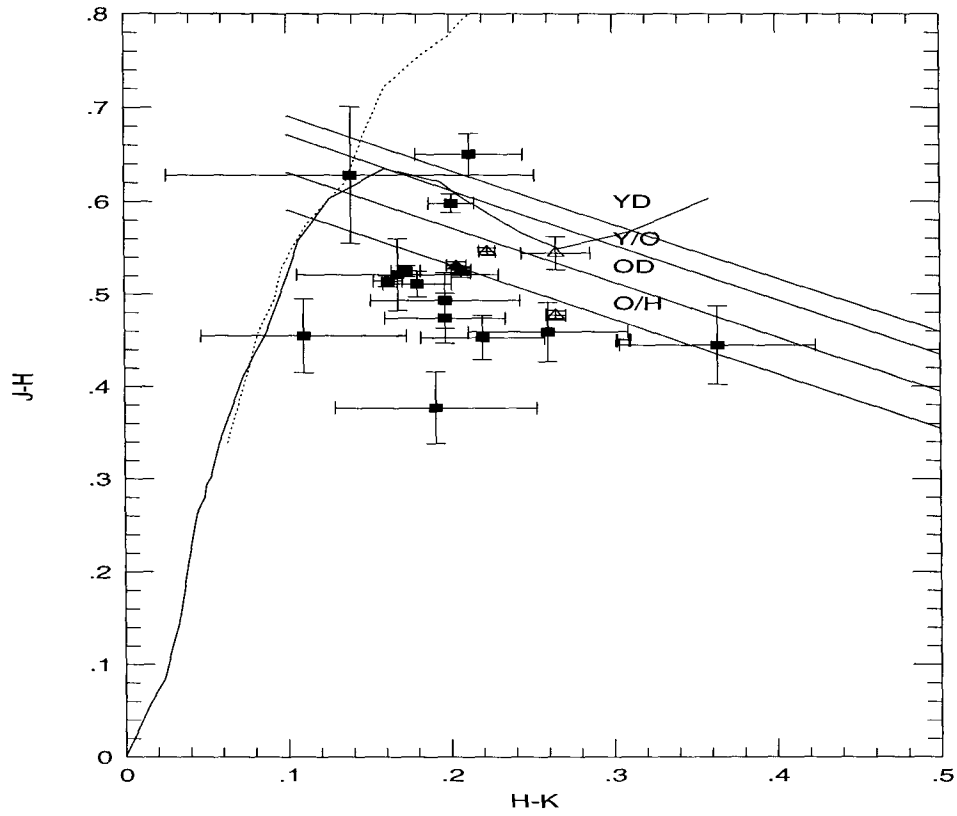

Figure 4.3: The near-infrared color-color diagram. The solid line shows the dwarf sequence of Bessell & Brett (1988), transformed to the CIT system. The dotted lines show the division into metallicity classes given by Leggett (1992). While our observational data have large uncertainties, the most metal-poor stars lie even deeper into the "Halo" region than the less metal-poor stars used by Leggett. Note that our data uses the Ks filter whereas previous work used K.

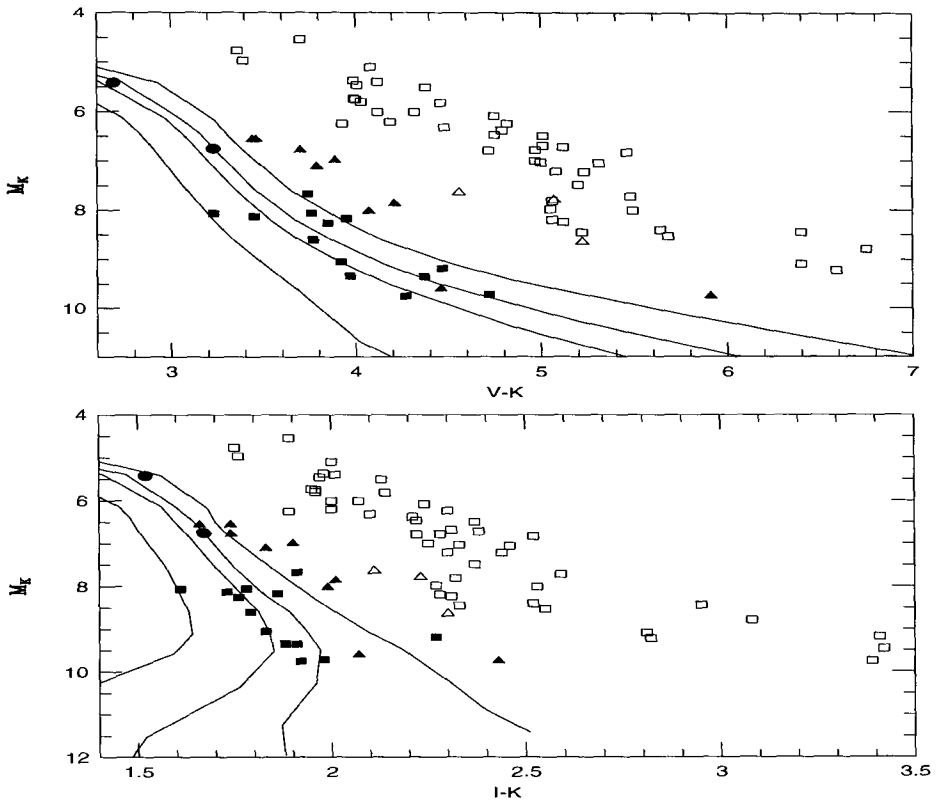

Figure 4.4: The optical/near-infrared HR Diagram. The solid squares are esdM, the solid triangles are sdM, the solid circles are earlier-type subdwarfs, and the open squares are single, nearby M dwarfs. The four lines are the model predictions of BCAH97: from left to right, $[m/H] = -2, -1.5, -1.3$ and -1.0. Note that we have ignored any differences between Ks and K.

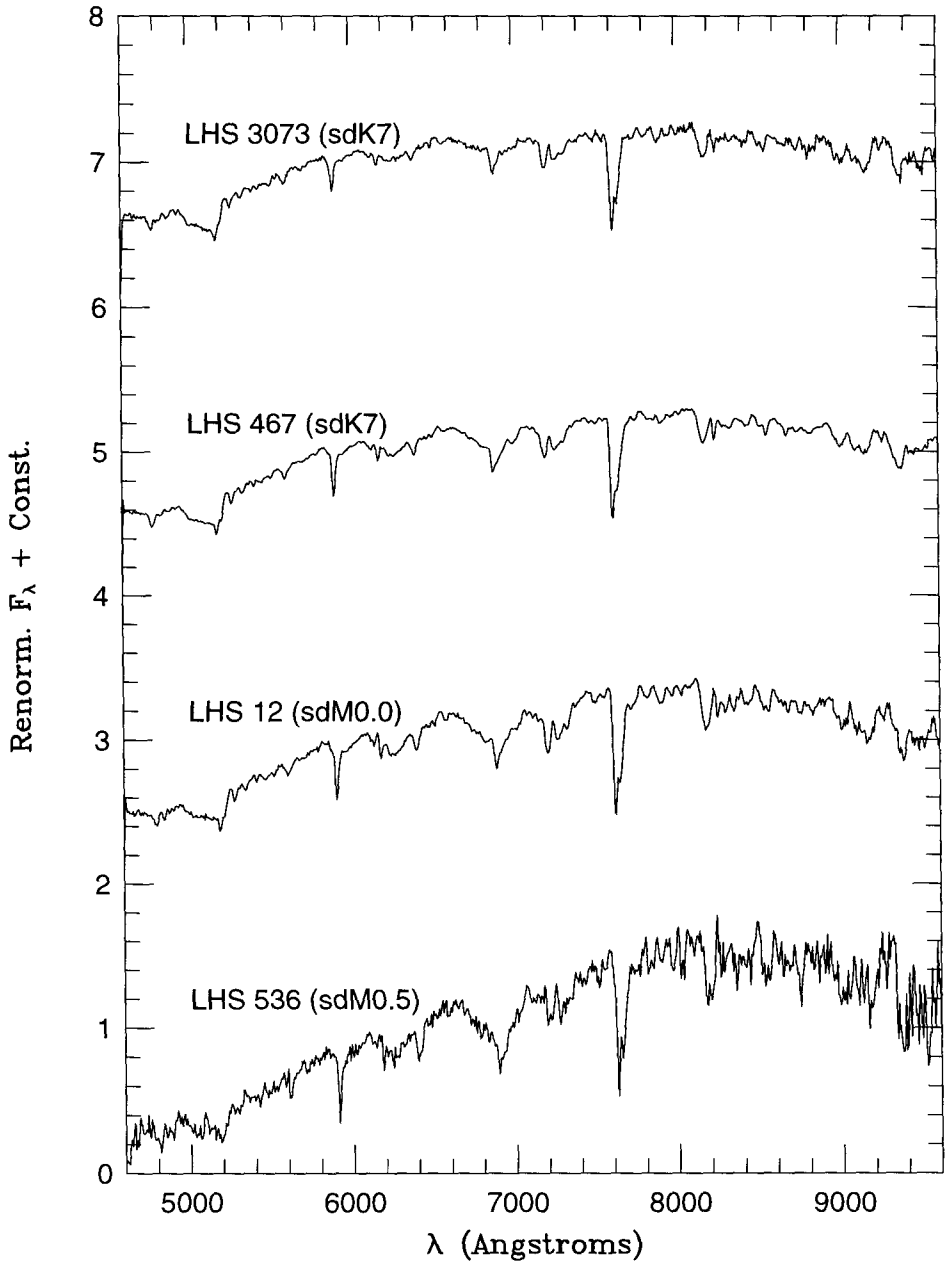

Figure 4.5: A spectral sequence for M subdwarfs (sdM). Our low-resolution spectra are arranged according to the classifications of Gizis (1997).

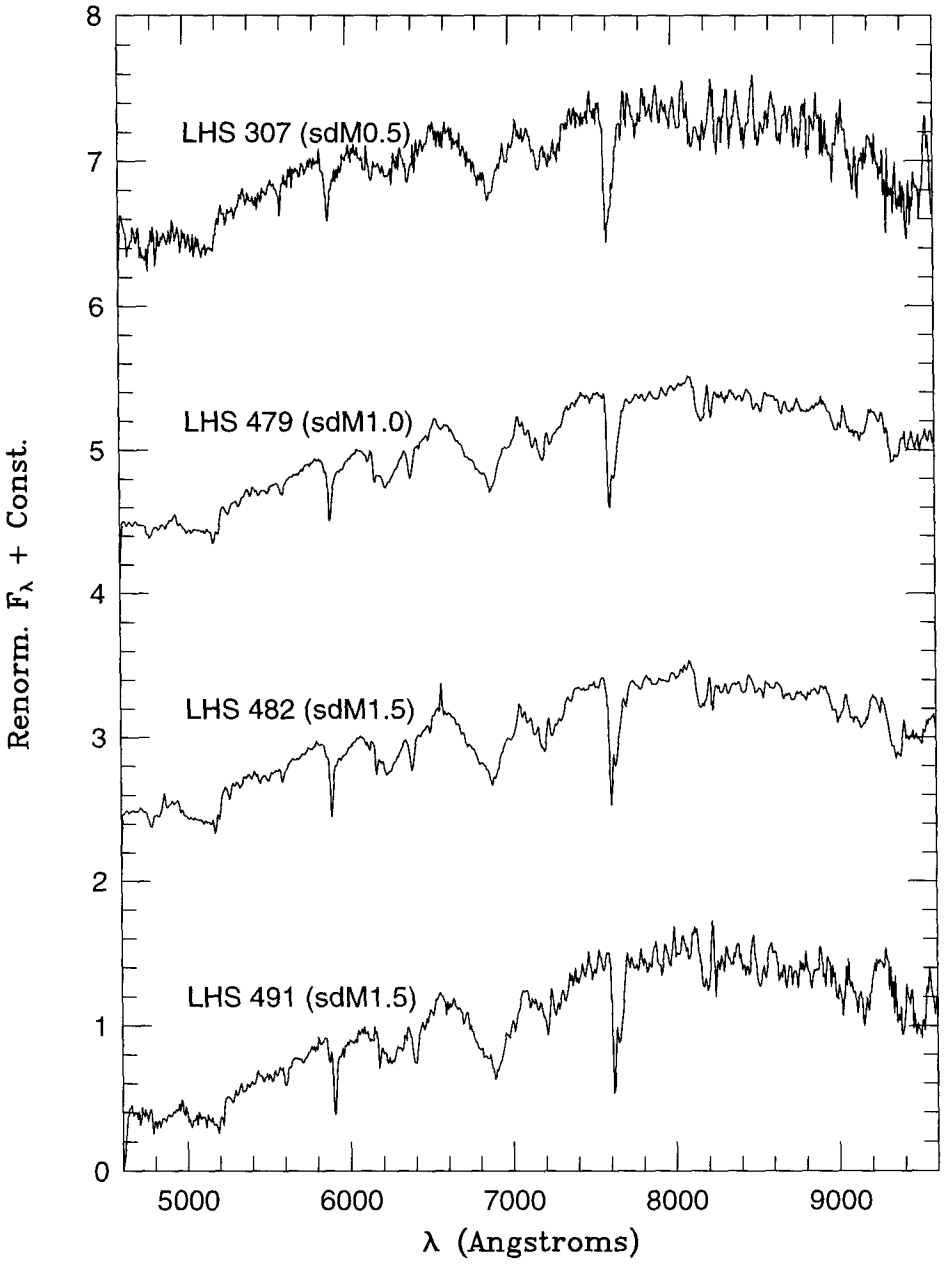
LHS 307 (sdM0.5)
LHS 479 (sdM1.0)
LHS 482 (sdM1.5)
LHS 491 (sdM1.5)
Renorm. F$_\lambda$ + Const.
λ (Angstroms)
0
1
2
3
4
5
6
7
8
5000
6000
7000
8000
9000

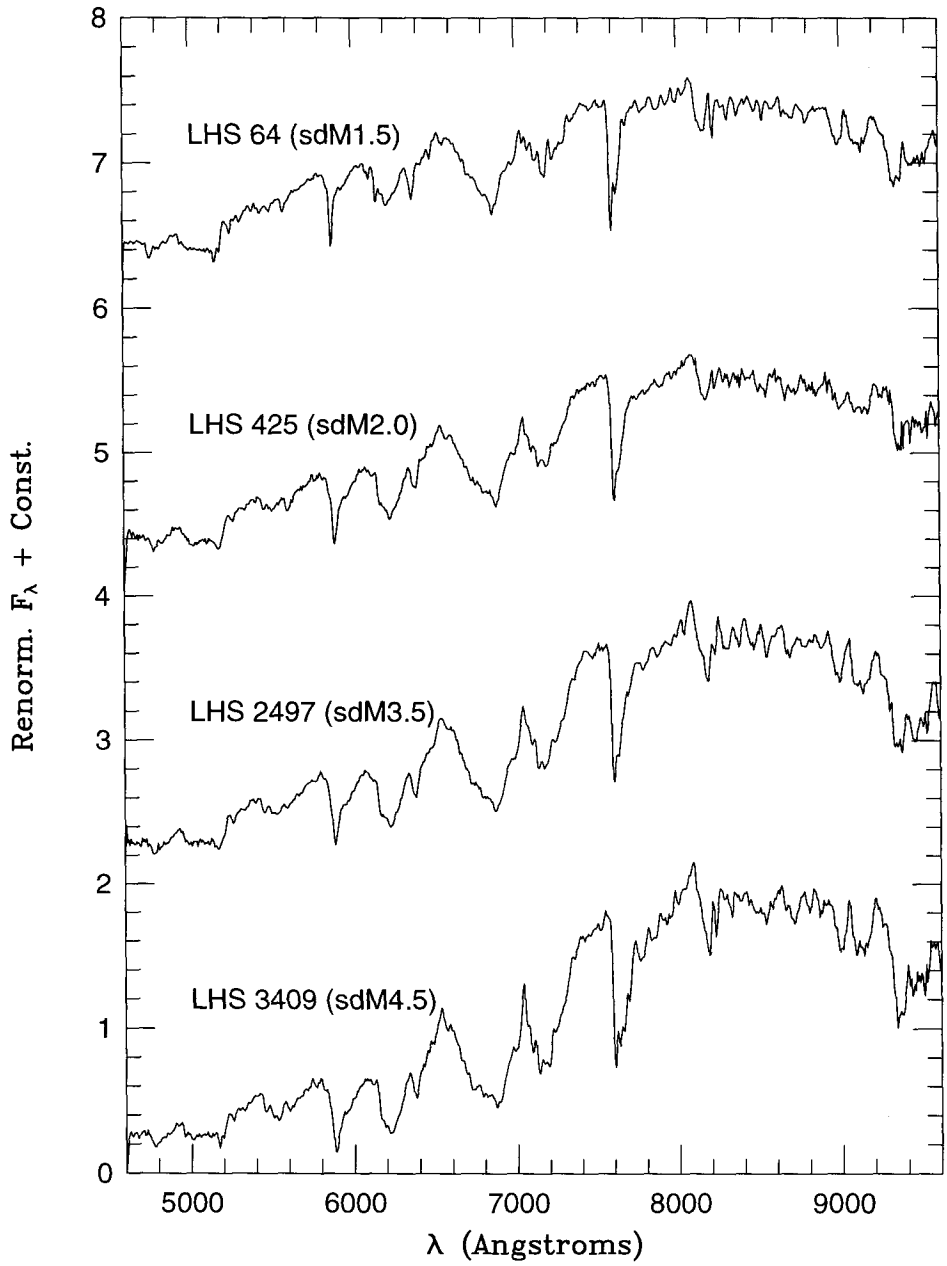
LHS 64 (sdM1.5)
LHS 425 (sdM2.0)
LHS 2497 (sdM3.5)
LHS 3409 (sdM4.5)
Renorm. F_λ + Const.
λ (Angstroms)
0
1
2
3
4
5
6
7
8
5000
6000
7000
8000
9000

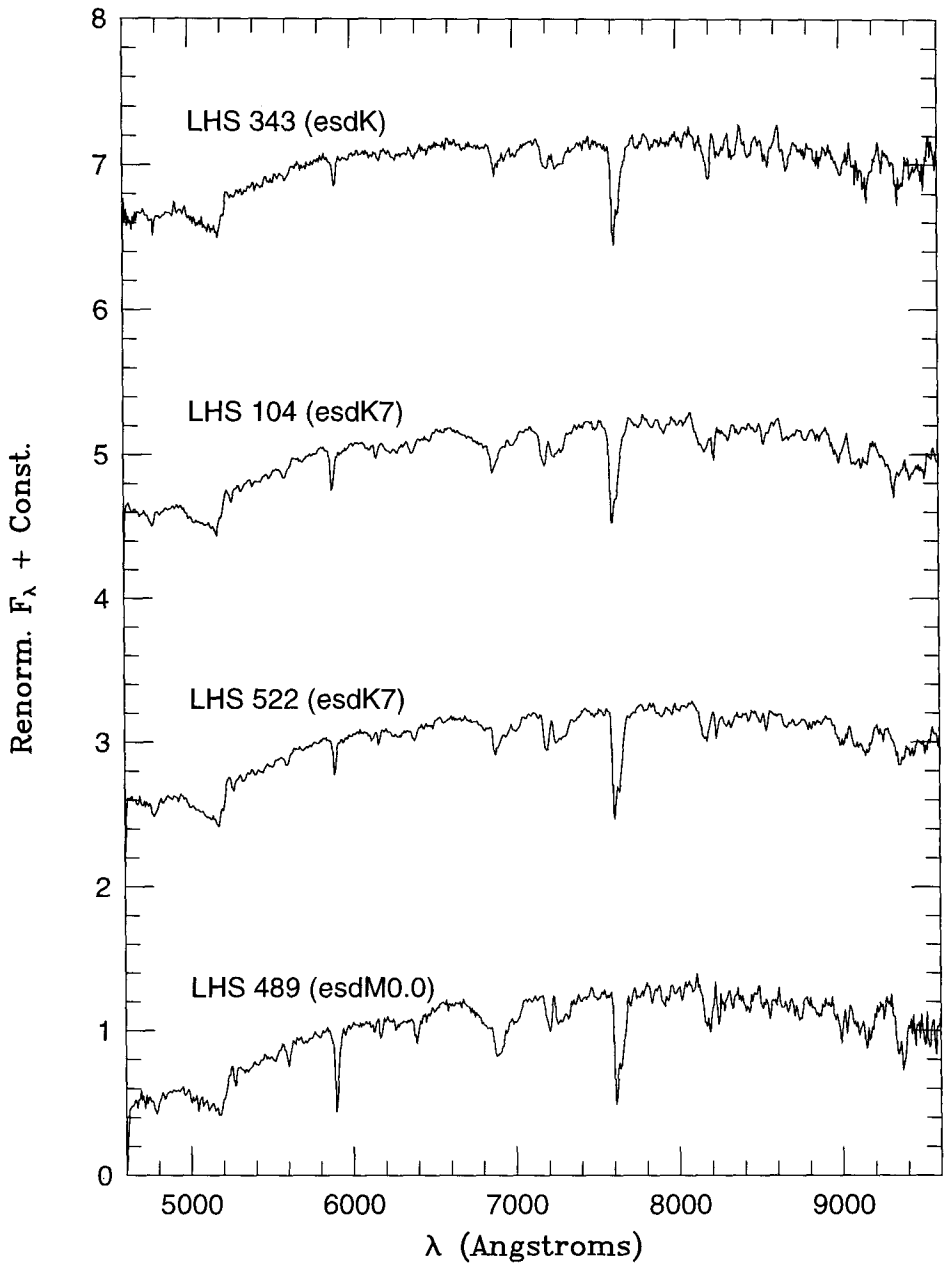

Figure 4.6: A spectral sequence for the late-K and early-M extreme subdwarfs (esdM). Our low-resolution spectra are arranged according to the classifications of Gizis (1997).

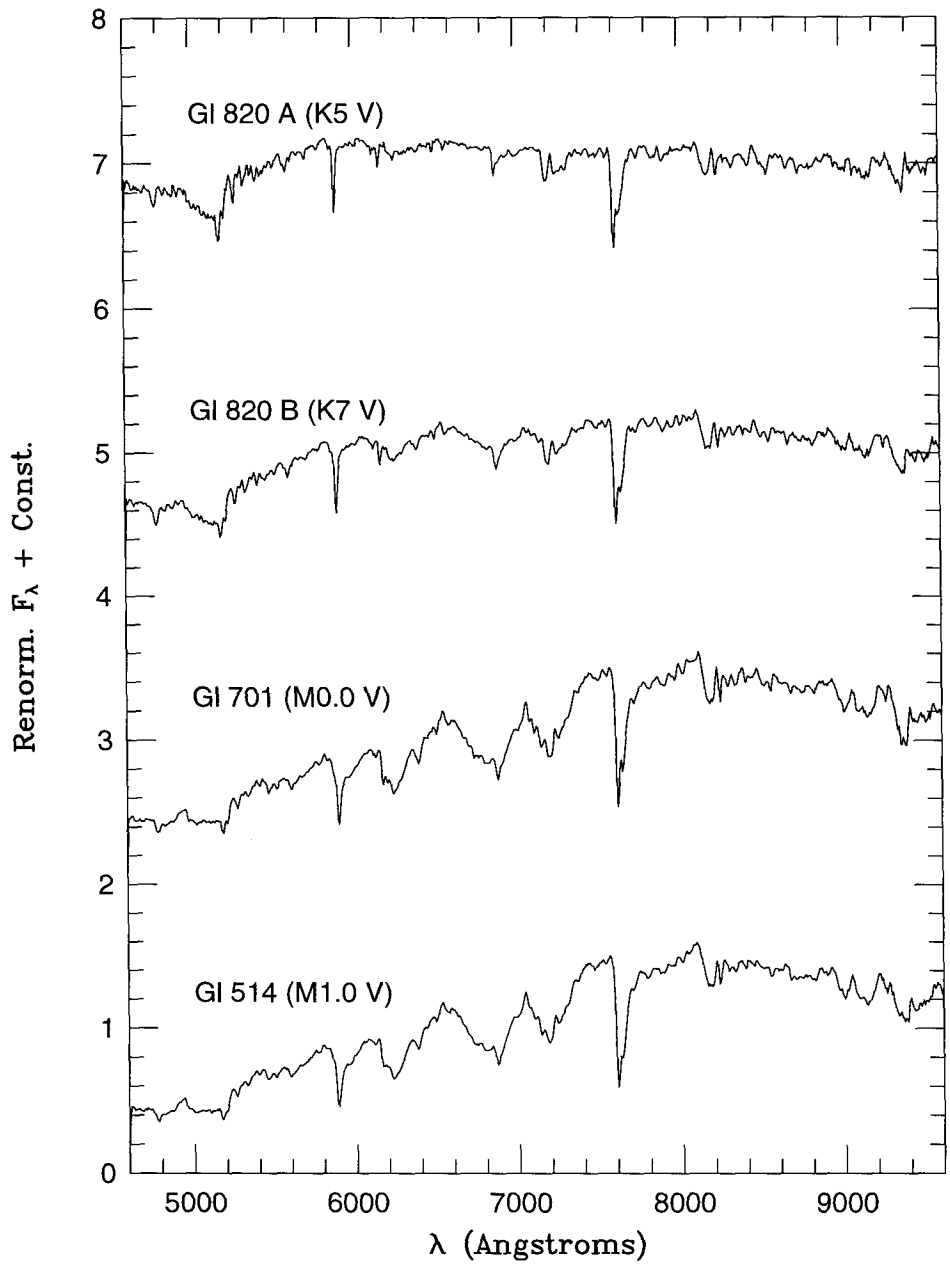

Figure 4.7: A spectral sequence for M dwarfs (M V). Our low-resolution spectra are arranged according to the Kirkpatrick et al. (1991) system.

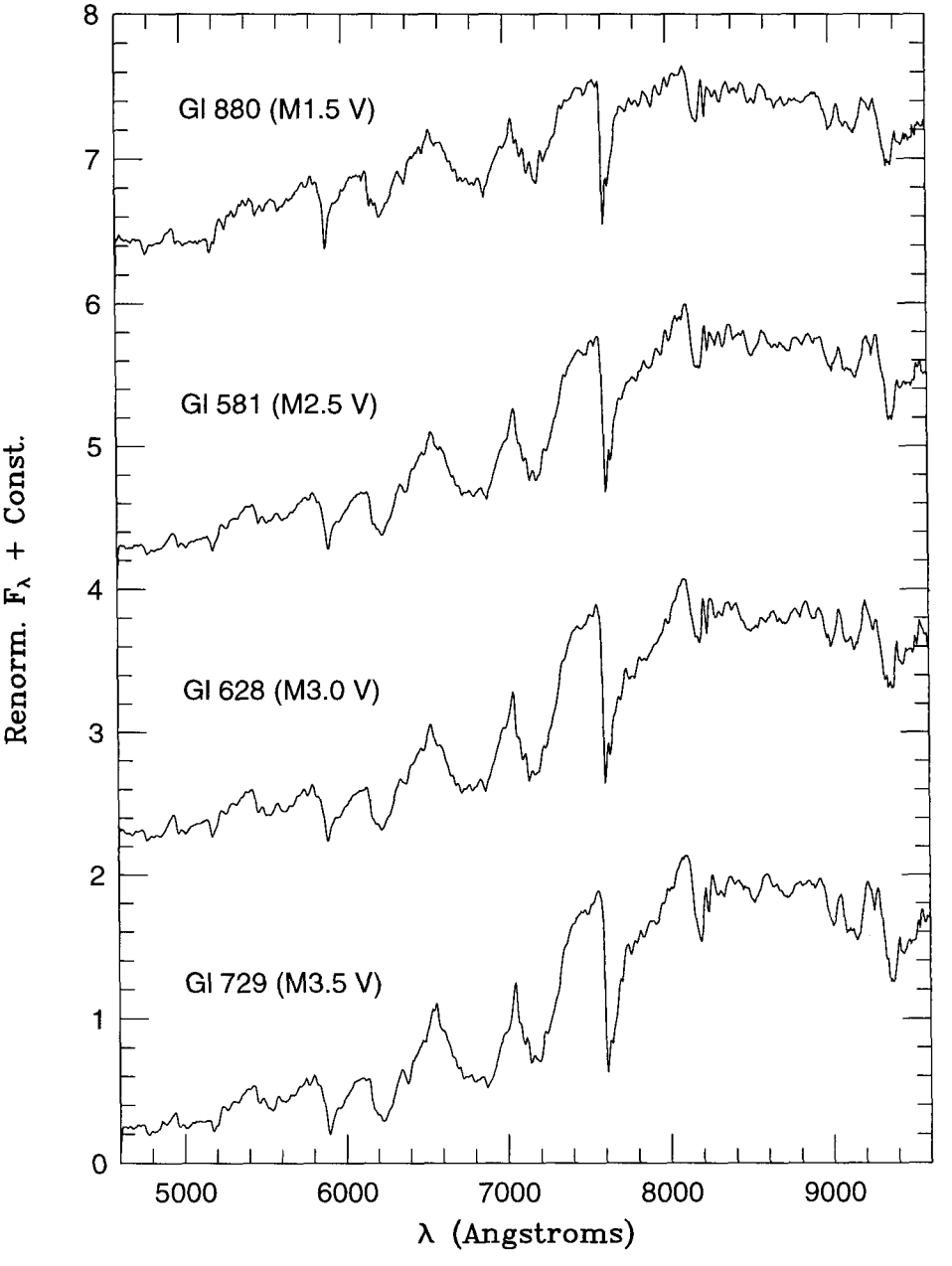
Gl 880 (M1.5 V)
Gl 581 (M2.5 V)
Gl 628 (M3.0 V)
Gl 729 (M3.5 V)
Renorm. F$_\lambda$ + Const.
λ (Angstroms)
0
1
2
3
4
5
6
7
8
5000
6000
7000
8000
9000

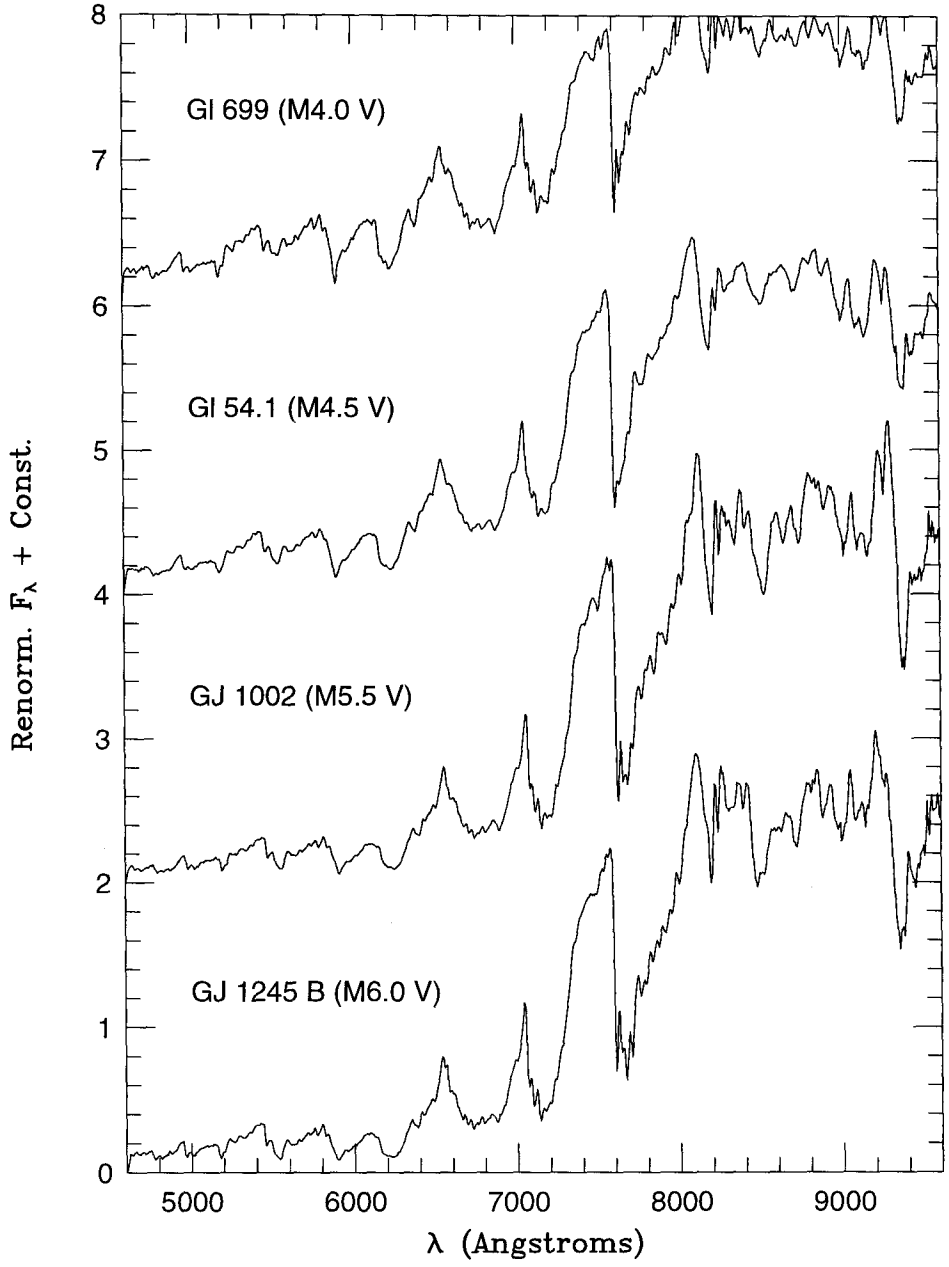
Gl 699 (M4.0 V)
Gl 54.1 (M4.5 V)
GJ 1002 (M5.5 V)
GJ 1245 B (M6.0 V)
Renorm. F$_\lambda$ + Const.
λ (Angstroms)
0
1
2
3
4
5
6
7
8
5000
6000
7000
8000
9000

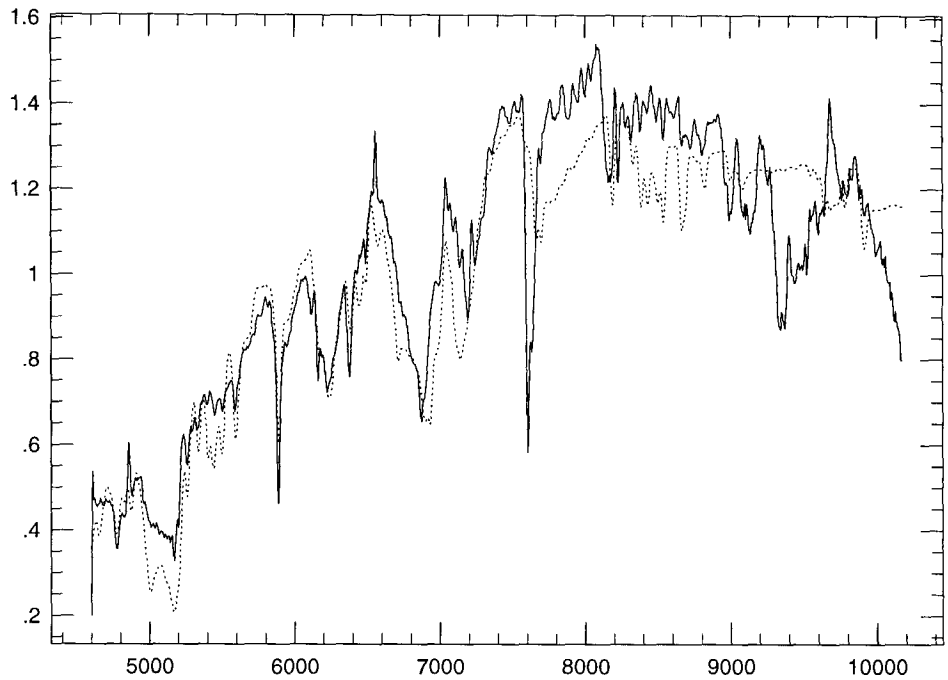

Figure 4.8: Comparison of LHS 482 (solid line) to a T_{eff} = 3600 K, $[m/H] = -1$ model (dotted line).

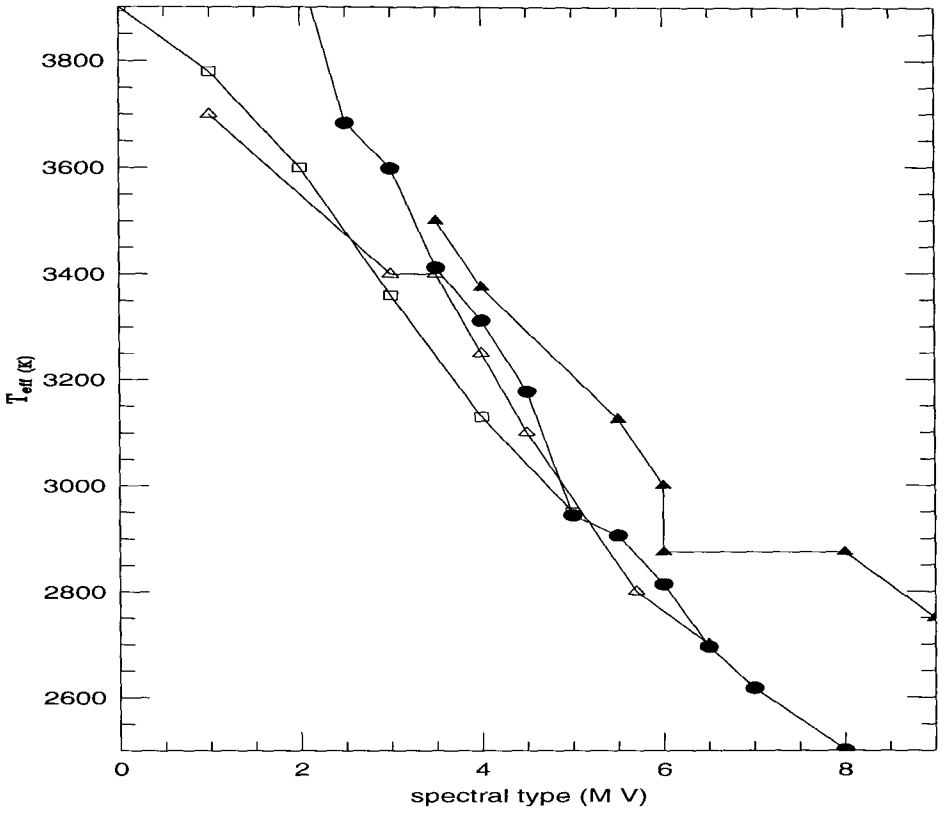

Figure 4.9: A comparison of the temperatures derived in this work from VIJHK photometry (solid circles) with the temperature scales of Kirkpatrick et al. (1993) in solid triangles, LABDH in open triangles, and Bessell (1995) in open squares. Our results are only slightly ($\sim$ 3%) hotter than LABDH. The overestimate of the temperatures for stars earlier than M3 in our procedure is due to the treatment of the TiO opacity in the model atmospheres.

Chapter 5 Forever Young: High Chromospheric Activity in M Subdwarfs

Abstract

We present spectroscopic observations of two halo M subdwarfs which have $H\alpha$ emission lines. We show that in both cases close companions are the likely cause of the chromospheric activity in these old, metal-poor stars. We argue that Gl 781 A's unseen companion is most likely a cool helium white dwarf. Gl 455 is a near-equal-mass M subdwarf system. Gl 781 A is rapidly rotating with $v \sin i \approx 30$ km s^{-1}. The properties of the chromosphere and X-ray coronae of these systems are compared to M dwarfs with emission (dMe). Although the relative strength of the X-ray coronae to the $H\alpha$ emission are similar to that seen in field and young cluster dMe, Gl 781 A's activity level is significantly weaker than the young cluster dMe. This suggests that different ages and/or metallicities can make two otherwise equally rapidly rotating, equal-mass stars have different activity levels.

5.1 Introduction

It has long been noted that most old halo stars show little magnetic activity relative to young disk stars — indeed, Joy (1947) used "a weakening of emission lines" as one of the criteria for identifying M subdwarfs. For disk stars, magnetic activity has been extensively studied from the onset of the convective envelope amongst F stars down to the hydrogen burning limit (as reviewed by Haisch & Schmitt 1996). Comparatively little is known about the activity of Population II stars — recent studies of Population II stars have addressed chromospheric activity of single stars (Peterson & Schrijver 1997) and X-ray emission in binary systems (Ottmann et al.

1997, hereafter OFP), but these studies targeted near-solar mass stars rather than very-low-mass stars. Nevertheless, the Population II M subdwarfs are worthy of study because stars with $M \lesssim 0.35 M_{\odot}$ are thought to be fully convective for all metallicities (Chabrier & Baraffe 1997), and therefore may have a different dynamo mechanism than solar mass stars which have radiative/convective zone boundaries (Giampapa et al. 1996;Durney et al. 1993). Moderate resolution spectra of very-low-mass stars allow the identification of high activity ("dMe") stars by the presence of $H\alpha$ emission lines while at the same time allowing the classification (Gizis 1997, hereafter G97) of metal-poor stars as sdM (M subdwarfs) and esdM (extreme M subdwarfs). In our recent Palomar/Michigan State University (PMSU) Nearby-Star Spectroscopic Survey (Reid et al. 1995; Hawley et al. 1996), two of 2063 stars showed both $H\alpha$ emission and anomalously weak TiO bands, indicating that these stars are sdMe. The PMSU sample consisted of the known M stars within 25 parsecs, and therefore was largely made up of disk near-solar metallicity stars. Subsequently, G97 surveyed a sample of cool high-velocity stars, identifying an additional 27 sdM and 17 esdM. Including our recent spectra of previously unobserved faint high-proper-motion stars (Gizis & Reid 1997a;Gizis & Reid 1997b), we have observed a total of 68 sdM and esdM stars. Only the original two subdwarfs show emission. G97 classified these stars, finding that Gl 781 (LHS 482) is sdM1.5e and Gl 455 (LHS 2497) is sdM3.5e. By fitting the synthetic spectra of Allard and Hauschildt (1995), G97 showed that the sdM stars have $[m/H] \approx -1.2 \pm 0.3$.

We present additional observations of these two sdMe systems aimed at understanding their nature and investigating the characteristics of their activity. Both stars prove to be close binary systems. We present the data in Section 5.2, discuss the magnetic activity in Section 5.3, and summarize our conclusions in Section 5.4.

5.2 Data Analysis

Spectra were obtained using the echelle spectrograph (McCarthy 1985) of the Palomar 60-in. telescope. The red cross-dispersing prisms were used, yielding wavelength

coverage from 4700Å to 9200Å with gaps between orders beyond 7000Å. The 2 pixel resolution was 0.3Å. Gl 455 was observed on 31 December 1995, 4 January 1996, and twice on 6 January 1996. Gl 781 was observed 23 times on UT dates 08-09 August 1996; four other observations were taken in July 1994.

The echelle data were reduced on a Sparc 5 running UNIX using the ECHELLE FIGARO routines (Tomaney & McCarthy, in prep.). Radial velocities were found by cross-correlation with the M-dwarf standards from Marcy & Benitz (1989). Comparison of other M-dwarfs observed on the same observing runs to high precision radial velocities show that the accuracy is ± 2 km s^{-1}; these uncertainties will be discussed in more detail in Gizis et al. (in prep.). The radial velocities are given in Tables 5.1 and 5.2.

No lines from a companion were seen in the spectrum of Gl 781 (Figure 5.1), which shows large velocity variations (Joy 1947); however, our monitoring yields a reliable period estimate. T. Mazeh and D. Goldberg kindly calculated orbital solutions using both June 1995 and August 1996 data. Due to the large separation in time between the observations, there are a number of different possible periods. Orbital solutions for each period are given in Table 5.3. Note that all periods lie within the range 0.497 ± 0.001 days. We will refer to the observed, brighter sdM star as Gl 781 A and the unseen, fainter companion as Gl 781 B. The mass of Gl 781 A is likely to be $\sim 0.25 M_{\odot}$ according to the models of D'Antona and Mazzitelli (1996) and Baraffe et al. (1995). With the observed mass function, $M \sin i = 0.3 M_{\odot}$ for Gl 781 B.

The absorption lines in Gl 781 A are broadened compared to other M-dwarfs observed with the same setup. To measure this broadening, we artificially broadened spectra of non-rotating stars obtained on the same night by convolving with the rotation profile (Gray 1992). We used the M1.5 V star Gl 880 as the standard. Marcy and Chen (1992) determined the upper limit on this star's rotational velocity to be 1.1 ± 1.1 km s^{-1}. The least squares fit of the atomic lines yields $v \sin i = 30 \pm 5$ km s^{-1}. To rule out the possibility of metallicity differences causing the broadening, we have repeated this procedure using the inactive sdM1.5 star LHS 64. LHS 64 does not show measurable broadening relative to Gl 880, and fitting the Gl 781 spectra to

artificially broadened LHS 64 spectra again yields $v \sin i = 30$ km s^{-1}.

The $H\alpha$ and $H\beta$ emission lines show significant variability. The $H\alpha$ line varies between 1.0Å and 1.3Å in the August 1996 spectra, with no dependence on orbital phase. In the July 1994 spectra, $H\alpha$ is seen between 1.3 and 1.6Å. Previous low resolution observations (Reid et al. 1995) observed $H\alpha$ in a stronger state (1.9Å). The $H\beta$ region is observed at low signal to noise, but $H\beta$ is definitely also variable with equivalent width of 1.7Å when $EW_{H\alpha} = 1.3$. Based on low-resolution spectrophotometry, obtained with the Palomar 60-in. telescope and spectrograph in July 1996, we estimate the continuum flux level as 1.1×10^{-13} ergs cm^{-2} s^{-1} Å^{-1} at $H\alpha$ and 4.7×10^{-14} ergs cm^{-2} s^{-1} Å^{-1} at $H\beta$. These indicate a line flux between 1.1 and 2.1×10^{-13} ergs cm^{-2} s^{-1} for *H alpha*, and a Balmer decrement of 1.8 for the $EW_{H\alpha} = 1.3$ observation. The He D3 line was detected with observed equivalent width of 0.15 ± 0.5Å. The He triplet at 6678Å was also marginally detected with an equivalent with of $\sim$ 0.1Å (this line is difficult to measure as it lies near a TiO bandhead).

We have used low-resolution spectrophotometry to convert these equivalent widths to fluxes. The spectra were obtained with the Palomar 60-in. telescope in July 1996 with wavelength coverage over the same region as the echelle spectra (the observations will be described in more detail in a forthcoming paper). The continuum region around $H\alpha$ has a flux of 1.1×10^{-13} ergs cm^{-2} s^{-1} Å^{-1} and that near $H\beta$ has a flux of 4.7×10^{-14} ergs cm^{-2} s^{-1} Å^{-1}.

Our four echelle spectra of Gl 455 clearly indicate it is a double-lined spectroscopic binary, but do not provide enough data to determine the orbital parameters. In the first two spectra (31 Dec. and 4 Jan.), the absorption lines from both components are resolved, with the cores separated but the wings overlapping. The other two spectra (6 Jan.) do not show line doubling. The small shift (0.9 km s^{-1}) seen for the observations separated by two hours suggests the period is much longer than Gl 781's period. We note that the velocity data are consistent with a $\sim$ 16 day period. It should also be noted that since the lines are never completely separated we cannot rule out the possibility that there is a third star in this system; G97 showed

that the two components of Gl 455 appear to lie above the sdM sequence in the HR diagram even after correcting for binarity. We do not detect rotational broadening in this system, indicating that $v \sin i < 15$ km s^{-1}. Since our resolution is insufficient to detect rotational broadening in most dMe (Gizis et al. 1998), this limit on the rotation is not surprising.

The $H\alpha$ equivalent width of Gl 455 AB is not resolved, so the reported equivalent widths are for the combined spectrum. In the December 1995 spectrum, the $H\beta$ line is resolved sufficiently to show that both components are in emission. Significant variability is present: the four equivalent widths of $H\alpha$ are $0.9, 1.1, 0.3, 0.6$Å and $H\beta$ are $2.0, 1.6, 0.3, 0.7$Å.

We have searched the ROSAT All-Sky Survey (Voges et al. 1996) to determine if the sdMe are X-ray sources. We match Gl 781 with 1RXS J200503.8+542609 and Gl 455 with 1RXS J120219.1+283507. The hardness ratio (HR1) given in the catalog is nearly identical with the hardness ratio (HR) used by Schmitt et al. 1995 to study nearby dM and dMe stars. We therefore determine the count rate-to-energy conversion factor (CF) using their equation

$$\mathrm{CF} = (5.30\mathrm{HR1} + 8.31) \times 10^{-12} \mathrm{ergs\ cm^{-2}\ counts^{-1}}$$

The derived X-ray fluxes are given in Table 5.4.

5.3 Discussion

5.3.1 The Binary Gl 781 and Its History

The observed mass function of the system and the theoretically estimated mass of Gl 781 A imply that Gl 781 B is more probably more massive ($M_B \sin i \approx 0.3 M_\odot$). Together with the fact that no lines are seen, this mass implies that Gl 781 B is a faint, cool white dwarf. The line strengths, colors, and absolute magnitude of Gl 781 A are similar to other sdM, so we estimate that the white dwarf is $\gtrsim 2$ magnitudes fainter, i.e. $M_V \gtrsim 13$. Ordinary white dwarfs ($M \sim 0.6 M_\odot$) have ages $\gtrsim 10^9$ years

at this luminosity (D'Antona & Mazzitelli 1990; we have used the Liebert et al. 1988 bolometric corrections). As shown below, the most likely possibility is that Gl 781 A is a $\sim 0.35 M_{\odot}$ helium white dwarf — the corresponding lower limit on the age is 2×10^9 years (Hansen & Phinney 1997).

The detection of rotational broadening serves as a constraint on the possible system parameters. Assuming that the Gl 781 A's rotational period is the same as that of the system,

$$\sin i = \frac{P \times (v_{rot} \sin i)}{2\pi R_{\rm Gl781A}}$$

The radius of the star is not known but can be estimated, either from stellar interior models, or by using the bolometric corrections and effective temperatures from model atmospheres (Allard and Hauschildt 1995) as fit by G97. Using the latter method, we estimate $L \approx 4.6 \times 10^{31}$erg s^{-1} and $T_{eff} \approx 3600$K, so $R \approx 0.28 R_{\odot}$. This estimate is in good agreement with stellar interior models (Baraffe et al. 1997). We then find that we expect v_{rot} to be 29 ± 6 km s^{-1}, compared to the observed $v_{rot} \sin i$ of 30 ± 5 km s^{-1}, suggesting the system is viewed nearly edge on, with $\sin i \approx 1$. If $\sin i$ is indeed near unity, then the white dwarf companion has an unusually small mass. Gravitational redshift measurements show that the distribution of white dwarf masses in wide binaries is strongly peaked at $M = 0.59 M_{\odot}$ (Reid 1996). This peak mass cannot be reconciled with the radius of GL 781 A deduced from the observed luminosity and effective temperature. Thus, the observations require that Gl 781 B is about half the mass of the typical relatively isolated white dwarf.

The small present day separation of the two stars, $a \approx 7 R_{\odot}$, implies that Gl 781 A was engulfed when Gl 781 B became a red giant. (Recall that the present day brighter companion, the sdM, was then the secondary by both mass and luminosity). There was therefore a phase of common envelope evolution. Since the mass of Gl 781 A is $\sim 0.25 M_{\odot}$ and the original mass of Gl 781 B was $M \gtrsim 1 M_{\odot}$ (since it has already evolved and cooled), it is clear that the mass ratio was greater than ~ 4 when the Gl 781 B became a red giant and first engulfed the companion. Iben & Livio (1993) have reviewed this situation and shown that a common envelope will form and that

the secondary (Gl 781 A) will not accrete a significant amount of mass. After being engulfed, Gl 781 A caused mass loss from Gl 781 B, possibly ending B's evolution as a He white dwarf with relatively low mass ($\sim 0.4 M_{\odot}$) instead of allowing B to become a CO white dwarf ($M \approx 0.6 M_{\odot}$). This would be consistent with the estimate of $\sin i$ from the detected rotational broadening. The calculations of Iben et al. (1997) indicate that for systems with 12 hour periods, helium white dwarfs with very-low-mass ($M < 0.3 M_{\odot}$) main sequence companions should be about seven times more common than CO white dwarfs with very-low-mass main sequence companions.

5.3.2 Chromospheric and Coronal Activity

For M dwarfs, membership in a very close ($P \lesssim 5$ days) binary system is thought to be a sufficient condition for high chromospheric activity — rapid rotation at relatively old age is maintained by tidal interactions between the two stars (Bopp & Fekel 1977; Young et al. 1987). Both Gl 455 and Gl 781 prove to be short period binaries, with Gl 781 A having detectable rotation, and therefore we attribute their activity to their binary nature. Gl 781 A's companion is not likely to affect the activity (except by being the cause of Gl 781 A's rapid rotation). Although red dwarfs near hot white dwarfs show $H\alpha$ emission due to reprocessing of the white dwarf's EUV flux in the chromosphere of the red dwarf (Schultz et al. 1996), Gl 781 B's low luminosity ($M_V > 13$) implies that it is not a significant source of EUV flux. Furthermore, Gl 781 A's emission is not arising from the hemisphere facing the white dwarf, since there is no correlation between the strength of $H\alpha$ with orbital phase in the August 1996 data. The white dwarf is therefore not causing the emission by incident radiation or other line-of-sight effects. We also attribute the X-ray flux to a normal corona generated by Gl 781 A's rapid rotation, rather than accretion onto the white dwarf, since at present Gl 781 A is only about 10% of the size of its Roche lobe as estimated by Eggleton's (1983) formula. We note also that the X-ray flux is not due to some sort of "basal" emission since none of the known sdM and esdM without $H\alpha$ emission are detected in X rays by ROSAT.

Metal-poor stars are usually associated with an extremely old (10^{10} yr) population. Preston et al. (1996), however, have identified young, A-type metal-poor main-sequence stars with large velocities which they suggest are the residue of a merger with a satellite galaxy (or galaxies). Presumably these stars have lower mass counterparts, and if the M-subdwarfs have emission lifetimes comparable to field M-dwarfs (Hawley et al. 1996), then these young M-subdwarfs will show detectable $H\alpha$ emission. We cannot directly rule out either Gl 455 or Gl 781 as members of this young, metal-poor population. The cooling time for the white dwarf in Gl 781 is at least 2 Gyr, which is too long to maintain such rapid rotation if M subdwarfs lose angular momentum like field M dwarfs. Overall, the binary nature of the two systems appears to be sufficient to explain their activity.

The properties of sdMe relative to (near-solar metallicity) dMe are important because they provide a unique perspective on the generation of strong activity. Gl 781 A and Gl 455 AB are the only known highly active, metal-poor, cool main sequence stars. Gl 781 A is of particular interest because its high rotational velocity is similar to the rotational velocities observed in the Pleiades cluster members of the same mass (Jones et al. 1996). In comparing the properties of the sdMe, it should be remembered that considerable dispersion exists in the chromospheric and coronal properties of even coeval, homogeneous samples such as the Pleiades and Hyades clusters, and that even larger dispersion exists in field samples. Thus any relations based upon only two systems must be viewed with caution.

We first note that the data suggest that the chromospheres and coronae of the sdMe are quite similar to disk dMe stars, despite the great metallicity difference between the two classes. The sdMe X-ray hardness ratios, which are sensitive to the coronae temperatures, are comparable to the field dMe with similar X-ray luminosities. The ratios of $H\alpha$ to $H\beta$ fluxes are similar to that seen in field dMe stars (Hawley et al. 1996; Gizis et al. 1998). The strength of the He D3 line is normal compared to the $H\alpha$ line, and correspondingly the strength of the He 6678 line is normal compared to the He D3 line. The correspondence between this sdMe and the dMe suggest that the physical properties (e.g., temperature) of the lower chromosphere (traced by the

Balmer lines), upper chromosphere (helium lines), and corona (X-ray) do not depend strongly on metallicity.

We measure the overall activity of each star using the ratios of the X-ray luminosity (L_X) and the $H\alpha$ luminosity ($L_{H\alpha}$) to the star's bolometric luminosity. We focus on Gl 781 A since we know the orbital period and $v \sin i$, allowing a comparison to disk dMe stars with similar rotation rates. Gl 455 A and B are more slowly rotating than Gl 781 A, but the period is unknown.

Jones et al. (1996) have measured $v \sin i$ for M dwarfs in the Pleiades, including stars with the mass ($\sim 0.25 M_\odot$) of Gl 781 A. These stars prove to have similar rotational velocities to Gl 781 A. Hence, we can directly compare the metal-poor star Gl 781 A to a population of stars with similar masses and rotation rates. There are three notable differences between Gl 781 A and the Pleiads: first, Gl 781 A is has an age of 2 Gyrs or more, at least 20 times the age of the Pleiades; second, Gl 781 A is metal-poor ($[m/H] \approx -1.2$) whereas the Pleiades have near-solar metallicity; third, Gl 781 A's companion might induce internal and surface differential rotation different from that of single stars (Young et al. 1987). Despite its comparable rotational velocity, Gl 781 A's ratios of L_X and $L_{H\alpha}$ to L_{bol} are both low (by about 1 order of magnitude) compared to similar mass stars in the Pleiades (Hodgkin et al. 1995). The emission is also weak compared to the M dwarfs in the Hyades cluster (Reid et al. 1995b). Evidently the activity level of Gl 781 A is lowered by one (or more) of the three factors noted above or else some additional, unrecognized factor.

We may also compare the activity of the sdM binaries to that of nearby field dM binaries. Like the M subdwarfs, these M dwarfs have activity induced by the rapid rotation caused by very close companions. We have detected a further 16 SB2 M dwarf binaries using the same echelle configuration as used for the current observations (Gizis et al. 1998). Matching these objects with the ROSAT All Survey, we find that only two have $\log(L_X/L_{bol}) < -3.5$. This suggests that the binary sdMe are indeed relatively weak in activity compared to similar binary dMe stars, although the samples are too small to attach a meaningful statistical significance to this result.

OFP's survey of spectral type FGK metal-poor binaries has shown that a sample

of Population II short-period binaries analogous to RS CVn binaries are at least one order of magnitude less X-ray luminous than the disk RS CVn binaries, although some Population II binaries are as luminous as the RS CVn binaries. They have suggested that the X-ray line emission is reduced due to the relative lack of metals in the corona of Population II systems with $-1.4 < [m/H] < -0.4$. Our sdM lie in the low-metallicity end of that range. The weakness of the activity of the metal-poor lower-mass stars, which might have a completely different dynamo operating, is consistent with the OFP suggestion that the lack of metals is an important factor. We note the chromospheric line emission is apparently also weakened by an equal amount, so the metallicity must affect the chromosphere as well. Of course, both the sdM and the higher mass OFP stars are also old, so as OFP note, it is possible that the magnetic field is affected by their great age.

5.4 Conclusions

We have obtained spectra of two halo very-low-mass metal-poor systems that show $H\alpha$ and X-ray emission. Both prove to be close binary systems, which accounts for their high activity level. We deduce that Gl 781 A's unseen companion is a cool white dwarf. The present-day orbital period of 12 hours implies that the system passed through a phase of common envelope evolution. Gl 455 AB consists of two near-equal luminosity sdMe.

The strength of the X-ray coronae of the sdMe relative to the $H\alpha$ chromosphere is well within the range observed in dMe stars in the field and in young clusters.

Despite Gl 781 A's very rapid rotation ($P_{orb} = 0.5$ days, $v \sin i = 30$ km s^{-1}), it has activity that is much weaker than Pleiades stars of equal mass that are equally rapidly rotating. Taken together, the sdMe binaries have weaker activity levels than most field dMe binaries. This shows that the rotation rate is not the only important factor setting the activity level of very low mass stars. Older age and/or lower metallicity may be the cause, since they are the most notable characteristics of the sdMe. This is consistent with the trend seen in higher mass Population II binaries, which have

relatively weak coronae compared to their disk counterparts. The sdM data suggests that some of the dispersion seen in disk relationships for M dwarfs could be due to the known dispersion in metallicity and age, although this cannot account for the dispersion seen in open clusters. With only two sdMe systems, these results are necessarily uncertain. Unfortunately, it will be difficult to significantly increase the sample of sdMe and esdMe since the two systems discussed here are the only such binaries detected amongst a total of 68 LHS catalog sdM and esdM stars observed from Palomar (Gizis 1997;Gizis & Reid 1997a;Gizis & Reid 1997b)

Acknowledgments

I would like to thank the staff of Palomar Observatory and in particular Skip Staples for assistance with the observations. T. Mazeh & D. Goldberg kindly computed the orbital solutions. Neill Reid and Suzanne Hawley gave helpful comments. I gratefully acknowledge support by Greenstein and Kingsley Fellowships as well as NASA grants GO-06344.01-95A and GO-05913.01-94A. This research has made use of the Simbad database, operated at CDS, Strasbourg, France.

Bibliography

Allard, F., & Hauschildt, P.H. 1995, ApJ, 445, 433

Baraffe, I., Chabrier, G., Allard, F., & Hauschildt, P.H. 1995, ApJ, 446, L35

Baraffe, I., Chabrier, G., Allard, F., & Hauschildt, P.H. 1997, A&A, in press

Bopp, B.W., & Fekel, F. 1977, AJ, 82, 490

Chabrier, G., & Baraffe, I. 1997, A&A, in press

D'Antona, F., & Mazzitelli, I. 1990, ARAA, 28, 139

D'Antona, F., & Mazzitelli, I. 1996, ApJ, 456, 329

Dempsey, R.C., Linsky, J.L., Fleming, T.A., & Schmitt, J.H.M.M. 1997, ApJ, 478, 358

Durney, B.R., De Young, D.S., & Roxburgh, I.W. 1993, Solar Physics, 145, 207

Eggleton, P.P., ApJ, 268, 368

Fleming, T.A., Schmitt, J.H.M.M., Giampapa, M.S. 1995, ApJ, 450, 401

Giampapa, M.S., Rosner, R., Kashyap, V., Fleming, T.A., Schmitt, J.H.M.M., & Bookbinder, J.A. 1996, ApJ, 463, 707

Gizis, J.E. 1997, AJ, 113, 806 (G97)

Gizis, J.E., & Reid, I.N., Hawley, S.L. 1998, in preparation

Gizis, J.E., & Reid, I.N. 1997, PASP, in press (August 1997)

Gizis, J.E., & Reid, I.N. 1997, PASP, in press (November 1997)

Haisch, B., & Schmitt, J.H.M.M. 1996, PASP, 108, 113

Hansen, B.M.S., & Phinney, E.S. 1997, MNRAS, in press

Hartmann, L.W., & Noyes, R.W. 1987, ARAA, 25, 271

Hawley, S.L., Gizis, J.E., & Reid, I.N. 1996, AJ, 112, 2799

Hodgkin, S.T., Jameson, R.F., & Steele, I.A. 1995, MNRAS, 274, 869

Iben, I. Jr., & Livio, M. 1993, PASP, 105, 1373

Iben, I. Jr., Tutukov, A.V., & Yungelson, L.R. 1993, PASP, 105, 1373

Jones, B.F., Fischer, D.A., & Stauffer, J.R. 1996, AJ, 112, 1562

Joy, A.H. 1947, ApJ, 105, 96

Kirkpatrick, J.D., & McCarthy, D.W. 1994, AJ, 107, 333

Liebert, J., Dahn, C.C., & Monet, D.G. 1988, ApJ, 332, 891

Marcy, G.W., & Benitz, K.J. 1989, ApJ, 344, 441

Marcy, G.W., & Chen, G.H. 1992, ApJ, 390, 550

McCarthy, J.K. 1985, Proc. SPIE, 554, 155

Monet, D.G., Dahn, C.C., Vrba, F.J., Harris, H.C., Pier, J.R., Luginbuhl, C.B., & Ables, H.D. 1992, AJ, 103, 638

Noyes, R.W., Hartmann, L.W., Baliunas, S.L., Duncan, D.K., & Vaughn, A.N. 1984, ApJ, 279, 763

Ottmann, R., Fleming, R.A., & Pasquini, L. 1997, A&A, 322, 785

Pallavicini, R., Gloub, L., Rosner, R., Vaiana, G.S., Ayres, T., & Linsky, J.L. 1981, ApJ, 248, 279

Peterson, R.C., & Schrijver, C.J. 1997, ApJ, 480, L47

Preston, G.W., Beers, T.C., & Shectman, S.A. 1994, AJ, 108, 538

Reid, I.N., Hawley, S.L., & Gizis, J.E. 1995a, AJ, 110, 1838

Reid, I.N., Hawley, S.L., & Mateo, M. 1995b, MNRAS, 272, 828

Reid, I.N. 1996, AJ, 111, 2000

Schmitt, J.H.M.M., Fleming, T.A., & Giampapa, M.S. 1995, ApJ, 450, 392

Schultz, G., Zuckerman, B., & Becklin, E.E. 1996, ApJ, 460, 402

Voges, W., et al., 1996, A&A, in press

Young, A., Sadjadi, S., & Harlan, E. 1987, ApJ, 314, 272

Table 5.1: Velocity Data for Gl 781

JD	V_{rad}	JD	V_{rad}
2449559.787284	70.59	2450304.002925	-134.41
2449560.793864	58.07	2450304.022841	-150.44
2449561.789240	57.89	2450304.661833	-47.03
2449561.856991	-37.40	2450304.707263	20.89
2450303.661066	-61.09	2450304.757906	75.85
2450303.685817	-23.23	2450304.801232	87.79
2450303.710209	16.40	2450304.806716	86.17
2450303.715577	22.64	2450304.811984	85.73
2450303.742898	58.07	2450304.816111	82.87
2450303.773024	77.66	2450304.872800	34.81
2450303.821616	84.31	2450304.925684	-39.83
2450303.881348	32.56	2450304.975199	-111.42
2450303.932413	-42.01	2450305.021252	-152.47
2450303.973081	-102.64		

Table 5.2: Velocity Data for Gl 455

JD	V^A_{rad}	V^B_{rad}	ΔV_{rad}	Comment
2450083.053575	52.9	-1.6	54.5	Resolved
2450087.002654	57.7	-1.1	58.7	Resolved
2450088.909443	29.2	$\cdots$	< 15	Unresolved
2450088.996125	30.1	$\cdots$	< 15	Unresolved

Table 5.3: Orbital Solutions for Gl 781

	P	γ	K	e	ω	T_0	$f(m)$
A	0.49603807	-33.97	123.31	0.0136	212.	2450193.974	0.0965
σ_A	0.00000057	0.40	0.63	0.0043	17.	0.024	0.0015
B	0.49636949	-34.06	123.31	0.0123	212.	2450194.397	0.0966
σ_B	0.00000050	0.35	0.56	0.0038	17.	0.024	0.0013
C	0.49670134	-34.15	123.29	0.0109	212.	2450194.323	0.0966
σ_C	0.00000049	0.34	0.54	0.0037	19.	0.026	0.0013
D	0.49703363	-34.23	123.27	0.0095	211.	2450194.249	0.0966
σ_D	0.00000052	0.36	0.57	0.0039	23.	0.031	0.0013
E	0.49736636	-34.31	123.24	0.0081	210.	2450194.174	0.0966
σ_E	0.00000059	0.42	0.66	0.0045	31.	0.043	0.0015
F	0.49769953	-34.38	123.20	0.0066	208.	2450194.097	0.0966
σ_F	0.00000070	0.49	0.77	0.0052	45.	0.062	0.0018
G	0.49803314	-34.45	123.16	0.0051	204.	2450194.018	0.0966
σ_G	0.00000082	0.58	0.91	0.0061	70.	0.097	0.0021

Table 5.4: Activity Measurements

Object	d (pc)	L_{bol}	L_X	HR1	$EW_{H\alpha}$	$\log(L_{H\alpha}/L_X)$
Gl 781 A	16.6	4.6×10^{31}	2.2×10^{28}	-0.41	1.3	-0.59
Gl 455 AB	20.3	2.0×10^{31}	1.9×10^{28}	-0.74	0.6	-1.11

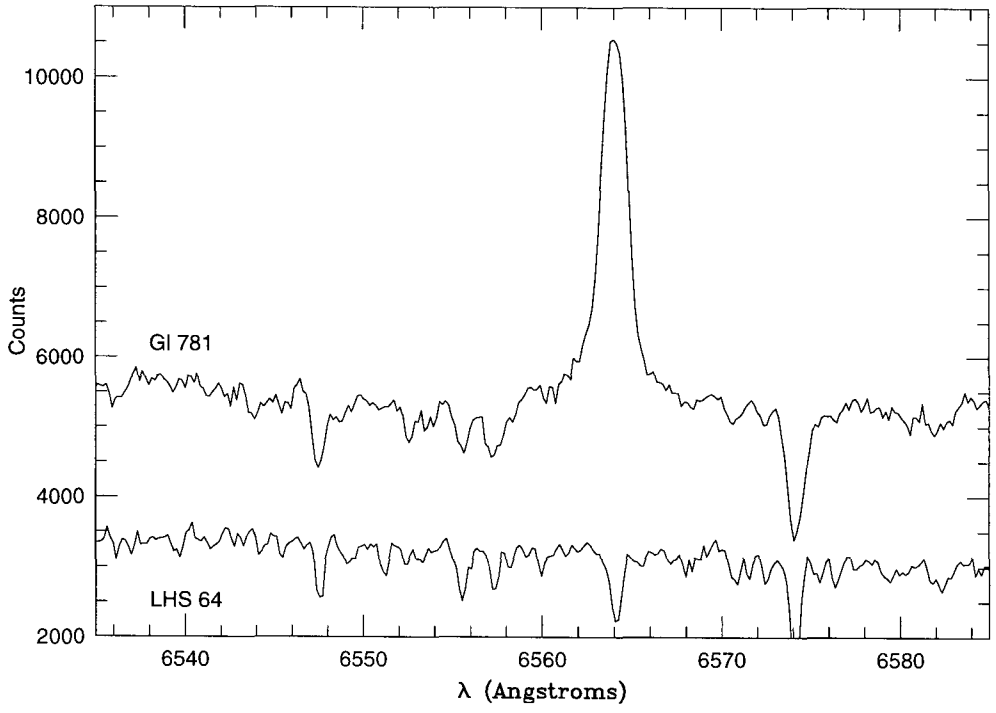

Figure 5.1: Spectra of the sdM1.5 stars Gl 781 and LHS 64. LHS 64 has been shifted by 338 km s^{-1} to match GL 781 A at this epoch. Note the broadening of Gl 781 A's absorption lines with respect to LHS 64. No lines from a companion to Gl 781 A are evident.

Chapter 6 The Population II Luminosity Function

6.1 Introduction

One of the most straightforward, at least in principle, yet fundamental measurements of a population of stars is a count of the numbers of stars of differing luminosities. The resulting "luminosity function" (LF), the number of stars per magnitude, is directly related to the "mass function" (MF), the number of stars per unit mass, through the mass-luminosity relationship.

The luminosity function of Population II stars, the old metal-poor component of the Galaxy, has been a subject of research for over 20 years. Schmidt (1975) used a complete sample of 18 high proper motion ($\mu \geq 1.295''$ yr^{-1}; $m_{pg} \leq 15.95$) stars to make the first determination of the field Population II luminosity and mass functions (down to $M_{pg} = 13$, corresponding to $M_V \sim 11$ or $M \sim 0.2M_\odot$). Although the resulting mass function was consistent with a power-law of slope $\alpha = 1$ or $\alpha = 2$, the measurements clearly rule out the Population II stars as a significant component of the dark matter halo, a conclusion only reinforced by Hartwick, Cowley, & Mould's (1984) finding that metal-poor $0.1M_\odot$ stars are not abundant enough to make up the dark matter. The studies thus showed that even the lowest mass main sequence stars are not viable dark matter candidates, a conclusion especially interesting given the recent claim by Alcock et al. (1997) that $\sim 0.5M_\odot$ microlensing events account for a significant portion of the dark matter, but were not precise enough to make conclusions about astrophysics.

It is important to determine the mass function for the metal-poor population because it formed under quite different conditions early in the universe's history. At present, it is not known what is the most important factor in setting the mass of stars.

Adams & Fatuzzo (1996) have presented a "semi-empirical mass function" that seeks to relate initial condition of the star forming cloud to the final mass of the star, with the dominant physical processes being accretion and mass loss from a stellar wind. They note that their theory is preliminary and not yet proven, and it is certainly true that other variables have been proposed as important, such as cloud-cloud coagulation (e.g., Murray & Lin 1996) and fragmentation (e.g., Zinnecker 1984).

Given this uncertainty in the theory, it would be of considerable value simply to determine if the stellar mass function varies as a function of initial conditions, for example metallicity or cluster density. Population II field stars provide the possibility of comparing their mass function to the near-solar metallicity field disk stars, In addition, HST has recently (De Marchi and Paresce 1995; Paresce et al. 1995; Elson et al. 1995; Cool et al. 1996) been able to determine luminosity functions of globular clusters, which can be directly compared to the field to test the effects of cluster density on star formation.

In this paper, we determine the luminosity function of the field Population II using a new proper motion survey based upon the first and second Palomar Sky Surveys. In Section 6.2, we discuss some general problems with the selection of halo stars. In Section 6.3, we describe the data used in our survey and the methods used to select a halo sample. In Section 6.4, we estimate the luminosity function of a "pure" halo sample. In Section 6.4.2, we use our survey to determine the fraction of the halo overlooked in the Section 6.4 luminosity function. In Section 6.5, we estimate the mass function. We discuss the luminosity and mass functions in Section 6.6. In Section 6.7, we summarize our results.

6.2 Selection of Halo Stars — General Principles

Measurement of the Population II luminosity function is considerable more difficult than the measurement of the Population I luminosity function, for the simple reason that the Population II represents a tiny fraction of stars locally. The Population I luminosity function is determined by counts of the catalogued stars within five

to ten parsecs (Reid & Gizis 1997) or within survey cones of $\sim$ 100 parsecs depth (Stobie et al. 1989; Tinney 1993) without significant contamination by metal-poor stars. The would-be census-taker of the Population II must literally exclude $\sim$ 99.8% of the stars in the survey volume. This requires an efficient method of eliminating the disk stars before time-consuming followup observations are obtained. Because Population II stars have very large motions, an initial sample of proper motion stars increases the halo contribution from $\sim$ 0.2% to $\sim$ 30% (Schmidt 1975). Such selection criteria introduce some kinematic bias, but lead to a much more manageable sample. Nevertheless, such a sample is still dominated by old disk (Population I) and "thick disk" (Intermediate Population II) stars. As recognized by Schmidt (1975) and further discussed by Bahcall & Casertano (1986, hereafter BC), even a small proportion of contamination by high velocity disk stars (sometimes called the "thick disk" or "Intermediate Population II") can lead a gross overestimate of the space density of the halo. In order to ensure a pure halo sample, Schmidt imposed a restrictive velocity criterion ($v_{tan} > 250$ km/s) and then applied a correction to account for halo stars with smaller velocities. BC used Monte Carlo simulations to argue that the correction factor for a cutoff velocity of 220 km s^{-1} is 3.03. This technique has more recently been used to derive a halo luminosity function from the LHS catalog stars with $0.8''\mathrm{yr}^{-1} \leq \mu \leq 2.50''\mathrm{yr}^{-1}$ and $11.0 < m_r < 18.1$ (Dahn et al. 1995).

If trigonometric parallaxes are available for the target stars, then the distances and tangential velocities are easily estimated and the appropriate kinematic criteria can be applied. This is the case for the Schmidt (1975) sample and the Dahn et al. (1995) samples. Measurement of a useful trigonometric parallax requires both years of observing — and requires the the target to be relatively nearby ($d \lesssim 100$ pc). Expansion of the sample to cover a larger space volume requires a less direct method of distance estimation. A photometric parallax can be estimated using the measured color and a color-absolute magnitude relation determined by stars with high quality parallaxes.

For the initial selection of halo candidates, a more appropriate way of proceeding is to use the "reduced proper motion", H, first used by Luyten (1939). It is defined

as

$$H = m + 5\log\mu + 5 = M + 5\log\frac{v_{tan}}{4.74} \tag{6.1}$$

where m is the apparent magnitude and M is the absolute magnitude. Note that H is distance independent and determined entirely by observables. If we assume a color-magnitude relationship, we can plot constant tangential velocity contours on the data. Figure 6.1 illustrates the concept. The 2111 observable M dwarfs within 25 parsecs (Reid et al. 1995; Hawley et al. 1996) are plotted. (Note that the increasing proper motion bias for redder stars in the catalog is clearly evident.) The lines illustrate where a disk population with halo-like velocities will lie, and how halo stars will be even more easily distinguished in the diagram. Stars drawn from a population that is subluminous in the color-magnitude diagram have systematically larger H at a given color, mimicking the effects of increasing v_{tan}. Fortunately, metal-poor stars are subluminous in V-I and R-I vs. M_I color-magnitude diagrams, increasing the offset from lower velocity disk stars. We have therefore selected our sample of candidate halo stars using photographic V-I or R-I colors samples that correspond to $v_{tan} \geq 220$ km s^{-1} for a disk population. Since halo stars are metal-poor, they will in fact be included in our candidate sample at smaller tangential velocities with a cutoff velocity that is a function of metallicity. This is indeed fortunate — as shown by Gizis (1997), the coolest metal-poor stars are *superluminous* at a given color in the B-V,M_V color-magnitude diagram. Thus, in the B-V,H_V diagram, a reduced proper motion cutoff tends to exclude metal-poor stars relative to higher metallicity stars.

6.3 Selection of Halo Stars — Data

6.3.1 Overview of Sample Selection

We utilized the techniques described above to define our sample. Proper motion stars were identified using the first and second epoch Palomar Sky Surveys, as described in Section 6.3.2). An initial cut of the sample was made to select large tangential velocity

stars, as described in Section 6.3.3. We then obtained spectra of each candidate halo star to estimate its metallicity and radial velocity, as described in Section 6.3.4.

6.3.2 Proper Motions

We used Schmidt Plates (each covering $\sim$ 25 sq. degrees) with a $\sim$ 40 year separations to search for faint proper motion stars. The fields analyzed are listed in Table 6.7. The first epoch plates for all fields were from the first Palomar Observatory Sky Survey (hereafter POSSI) taken with the 48-in. Oschin Telescope. For the most part, the second epoch plates were taken with the 48-in. Oschin Telescope (for the Palomar Observatory Second Sky Survey, POSSII) or the U.K. Schmidt telescope (UKS). These second epoch plates were used by Tinney, Reid, & Mould (1993, hereafter TRM) in their determination of the Population I luminosity function. The POSSI scans were performed by the APM group. The POSSII/UKS plates were scanned by COSMOS. One additional field, centered near the North Galactic Pole, was used. The analysis of this plate is described by Reid (1990). The second epoch plates for this field were taken with the Palomar 48-in. Oschin Telescope in 1976 and were scanned by COSMOS. The scans yield positions (both pixel x,y positions on the plate and right ascension, declination positions on the sky), magnitudes, and classification as stars, galaxies, "merged stars," or noise. All objects classified as noise were excluded from further analysis.

Before the search for proper motion stars, the objects (stars and galaxies) identified in the scans of the plates taken at the same epoch must be matched. In the case of the first epoch POSSI data, this is straightforward, since the O and E plates (corresponding roughly to photometric B and R observations) were taken on the same night. Thus there is no real motion between the time of the observations and the plate scans can be matched by demanding positional coincidence to a high level of precision. For our second epoch TRM data, the IIIaF (photometric R) and IV-N (photometric I) plates were not observed on the same night. TRM paired the objects identified on their scans using a 3 arcsec box. Since the TRM plates were taken $\sim$ 3

years apart, this procedure will lose the highest ($\mu \gtrsim 1$ arcsec yr^{-1}) proper motion stars. In our survey, this is not a concern because the 40 year separation between the first and second epoch, with the lack of plates at intermediate epoch, implies that stars with high proper motion cannot be reliably identified due to the large number of possible pairings. Our analysis of the luminosity function fully accounts for an upper proper motion limit of 0.375 arcsec yr^{-1}. We should also note that the TRM plates are restricted to the region within 3 degrees of the plate center in order to avoid the vignetted regions near the edge of the plates, and that the COSMOS scans did not cover the entire plate. The appropriate area of the survey is given in Table 6.7. It should be noted that the POSSI field centers do not correspond to the POSSII/UKSRC field centers. Thus, between one and four POSSI plates were paired with the TRM fields, as listed in Table 6.7.

The identification of the proper motion stars was made as follows. First, an initial pairing of objects within a 3 arcsecond box was made. Within this close a radius, the matching is unambiguous. Figure 6.2 illustrates the agreement between the r_P and E magnitudes for one representative pairing (POSSII Field 513 and POSSI E102). Most of the outliers evident in this plot are correct pairings of extended objects (galaxies or merged stars) — they are outliers due to differences in the definitions of magnitudes used by the two machines, as well as the different plate characteristics. For this study, we are only interested in the stars, so such outliers are unimportant. Having paired the unambiguous matches, we obtain a list of unmatched objects — these objects have no counterparts within 3 arcseconds at the other epoch and are good candidates for proper motion stars. Eliminating the paired objects, we then find all possible matches within 15 arcsec of these unmatched objects. We exclude those pairings which have magnitudes inconsistent with the E -r_P relation defined by the close matches — inconsistent being more than 1 magnitude away at the bright ($r_P = 12$) end to 1.5 magnitudes away at the faint ($r_P = 19$) end. These limits were chosen as "conservative" limits, in the sense that some false pairings will be included in order to avoid excluding true proper motion stars.

The vast majority of objects on the plate should show insignificant proper motion

between the two epochs, but directly matching the right ascension and declination catalog positions leads to many (false) proper motion objects. These false objects are due to systematic errors in the relative positions of the two catalogs (caused by differing plate centers, inadequacy of the plate model, plate variations, telescope differences, etc.) These systematic positional errors can be corrected by determining the transformation between the original pixel positions for the two epochs (x_1, y_1 and x_2, y_2). Both our own experience with the TRM fields and the Reid (1990) analysis showed that a polynomial solution over the entire plate works poorly, producing many false proper motion stars. Analysis over smaller regions, however, is effective. Each plate was divided into approximately one by one degree regions and the positional transformation determined using second-order two-dimensional polynomials. Only the matches within 3 arcseconds were used for the initial solution. The solution was then iterated twice to exclude those objects with large ($> 2''$) residuals. In addition, objects classified as galaxies were excluded, since the position of an extended object may be poorly defined. We then used these polynomial solutions to determine the proper motions of *all* stars in the field. The stars that proved to have $\mu \geq 0.1$ arcsec yr^{-1} defined our sample of proper motion stars. The selection of the candidate halo stars is described in Section 6.3.3.

The proper motions described above are measured relative to faint stars, which on these plates have typical distances of $\sim 500 - 4000$ pc. Thus we expect the reference frame to have a small, but non-zero, mean proper motion. We derive the conversion from this relative frame to an absolute (extragalactic) frame by using the objects classified as galaxies. Specifically, we use the ϕ-parameter defined by Picard (1991). We take $200 < \phi < 600$ for these purposes, which provides a sample dominated by galaxies. The upper cutoff is taken to exclude the "fuzziest" galaxies — we found that these "fuzzy" galaxies have large spurious proper motions, which we attribute to the different plate material for the different epochs, scanning machines, and centroiding procedures. In Figure 6.3, we plot the distribution of galaxy proper motions and stellar proper motions for the fields. It is clear that the galaxies do indeed show a systematic shift with respect to the stars. Table 6.7 lists the median proper motions

($\Delta\mu$) derived for the galaxies, which at most amount to 5.2 mas yr^{-1}. We have checked these values by comparison with the projection of the solar motion and rotational lag for the thick disk and halo populations. The direction of motion derived by the galaxies (i.e., the *sign* of the proper motions) agrees with the expectations. These values given in Table 6.7 are used to correct the relative proper motions to an absolute system:

$$\mu_{abs} = \mu_{rel} - \Delta\mu$$

We also give the observed standard deviation of the galaxies. The values are in the range $10.6 - 17.0$ mas yr^{-1}. These are an estimate of the uncertainties of our proper motions, but we expect that the extended galaxies should have poorer positions and hence proper motions than the stars.

The NLTT catalog (Luyten 1979-1980) offers an opportunity to check both the completeness and accuracy of our measurements. As noted by many authors, identifying the NLTT stars can be difficult since some of the positions are quite poor (for example, we find a star that matches the magnitudes and proper motion of LP 621-64, but is 10 *arcminutes* east of Luyten's position). Excluding stars which are too bright, too faint, or too blue (i.e., too faint to be seen on the IV-N plates), we find that 122 of 137 NLTT stars are recovered, implying a completeness of 89%. We find that the standard deviations of $\mu_\alpha^{us} - \mu_\alpha^{NLTT}$ and $\mu_\delta^{us} - \mu_\delta^{NLTT}$ are in the range 10 to 25 mas yr^{-1}. Luyten estimated his motions to be accurate to $\pm 15 - 25$ mas yr^{-1}. The combination of our uncertainties estimated from the galaxies and the NLTT uncertainties account for the observed scatter.

6.3.3 Reduced Proper Motions

Selection of halo candidates using reduced proper motion requires photometry in addition to the proper motions. We have used the photometry from the second epoch plates which provides us with R and I measurements for each star (except in the NGP field, for which we have V and I).

We adopt the photometric calibration determined by TRM using CCD measure-

ments for each plate. Because their ("Palomar") calibration is on a unique system, we describe it briefly here. A complete description is given by TRM. The best defined photometric system in R and I for late-type stars is the Cousins system (Cousins 1973)[1] However, M-dwarfs have strong color terms in this system because the R_C band filter extends far into the I band — as a result, the effective wavelength of the R_C filter moves redward for cooler stars, as discussed by Bessell (1986). The POSSII IIIaF emulsion plus filter combination does not have this long redward tail, so its color term will differ significantly from the normal Cousins system. The POSSII response is close to the Gunn r filter defined by Thuan & Gunn (1976). Therefore, TRM's CCD calibrations of the fields used Gunn r_G and i_G filters but observed *Cousins* late-type standards. These CCD magnitudes were matched to the COSMOS photographic magnitudes. They found that no significant I color term was necessary to calibrate the observations but, as expected, a strong R color term was necessary. Thus, their photometric observations consist of an R magnitude, denoted r_P, an I magnitude, denoted i_P, and a color, denoted $(r-i)_P$, for each star. The relation between the standard Cousins color and the Palomar color is

$$(r-i)_P = 0.162 + 0.439(R-I)_C + 0.671(R-I)_C^2 - 0.36(R-I)_C^3 + 0.074(R-I)_C^4 \tag{6.2}$$

$$i_P = I_C \tag{6.3}$$

Note that TRM use the relation $i_P = I_C - 0.046$, but examination of their Figure 2 indicates that there is no offset between i_P and I_C for $(R-I)_C < 1.2$, which is the color of the halo stars in our survey. The V and I photometric calibration for the NGP field is described in Reid (1990).

The reduced proper motion diagram for Field 513 is shown in Figure 6.4. We

[1]As in TRM, we use the "R" and "I" to denote generic R and I photometry on any system and indicate particular photometric systems with subscripts. Thus R-I_C is Cousins R-I, $(r-i)_P$ is TRM's Palomar system, and $(r-i)_G$ is Gunn R-I.

plot as a solid line the cutoff corresponding to $v_{tan} = 220$ km s^{-1} for the disk main sequence determined by TRM. This main sequence is a second-order polynomial:

$$M_i = 5.56037 + 0.458615 \times (r-i)_P + 1.32084 \times (r-i)_P^2 \qquad (6.4)$$

This is the cutoff we have applied for the selection of the halo candidates for spectroscopic followup. Recently, we have pointed out that the disk main sequence shows evidence for a "kink" at spectral type M4.0 V (Gizis and Reid 1996; Reid & Gizis 1997; Clemens et al. 1997) This "kink" occurs at $(R-I)_C \approx 1.6$, so it is not relevant to selection of candidate halo subdwarfs, at least for this survey.

6.3.4 Spectroscopy

For each candidate halo star, we obtained spectra in order to determine the radial velocity and metallicity. The Hale 200-in. and the Las Campanas Du Pont 100-in. telescopes were used to obtain spectra in the wavelength range $6100 - 7300$Å with ~ 3Å resolution. These parameters were chosen to correspond to the observations of nearby M-dwarfs (Reid et al. 1995; Hawley et al. 1996) and M-subdwarfs (Gizis 1997) that we have already published. For the 200-in. observations, we used the Double Spectrograph (Oke and Gunn 1982). In August 1995, the blue camera was set to observe $6000 - 6900$Å and the red camera was set to $6700 - 8000$Å using 600 l/mm gratings blazed at 4000Å and 10000Å respectively. In October 1995, a new red camera was installed in the double spectrograph and was used in all subsequent runs to observe the region $\lambda 6000 - 7400$Å at 1.4 Å pix^{-1} with the 600 l/mm grating blazed at 10000Å. With this setup, the blue camera was used to cover $4000 - 5500$Å with a 300 l/mm grating blazed at 3990Å. In practice, this blue camera data were useful only for the bluest ($(r-i)_P < 0.6$) stars. The 100 in. telescope observations used the modular spectrograph with a 1200 line grating blazed at 7500Å.

For each star, we determined the radial velocity and spectral type. During each observing run, we observed K and M radial velocity standard stars drawn from the list of Marcy & Benitz (1989). A velocity for each candidate halo star was determined

by cross-correlating with the best match standard star. Comparison of subdwarfs with known radial velocities observed during the same runs shows that the accuracy is ± 20 km s^{-1} (Gizis 1997). Using these radial velocities, we measured TiO and CaH bandstrength indices. These indices were originally defined by Reid et al. (1995). Each index measures the ratio of the flux (F_ν) within the absorption feature to nearby pseudo-continuum points. Table 2.7 lists the wavelength definitions of the features (W) and the pseudo-continuum (S1,S2) points. We have defined a spectral classification system using these indices (Gizis 1997). Stars are classified as disk stars (M V), M subdwarfs (sdM), or extreme M subdwarfs (esdM). We have shown on the basis of model atmosphere calculations (Allard and Hauschildt 1995) that these empirical classifications correspond to $[m/H] \approx -0.5$, $[m/H] \approx -1.2 \pm 0.3$, and $[m/H] =\approx -2.0 \pm 0.5$. Each halo candidate star has been classified using this system.

6.4 The Luminosity Function

In this section, we calculate the luminosity function from the data described in Section 6.3. The luminosity function, $\Phi(M_I)$, is defined as the number of stars per cubic parsec per magnitude in a bin centered at M_I . Our luminosity function is calculated in the I band. We use Schmidt's $1/V_{max}$ technique to estimate $\Phi(M_I)$

$$\Phi_{obs} = \sum \frac{1}{V_{max}} \tag{6.5}$$

$$V_{max} = \frac{\Omega}{3}(d^3_{max} - d^3_{min}) \tag{6.6}$$

Where Ω is the solid angle on the sky of the survey, d_{max} is the maximum distance that a given star could have been detected in this survey, and V_{max} is the corresponding volume. A minimum distance, D_{min}, also appears to account for the distance at which the star would have evaded detection due to the upper proper motion limit

of $\mu_{max} = 0.375''$ yr^{-1}. The maximum distance may be limited either by the lower proper motion limit ($\mu_{min} = 0.100''$ yr^{-1}) or the limiting magnitudes (R_0, I_0), hence

$$d_{max} = d \times \mathrm{Min}\left(\frac{\mu}{\mu_{\mathrm{min}}}; \mathrm{dex}[0.2(\mathrm{R} - \mathrm{R}_0)]; \mathrm{dex}[0.2(\mathrm{I} - \mathrm{I}_0)]\right) \tag{6.7}$$

We estimate the associated error by assuming that each star contributes an uncertainty of $1/V_{max}$ (Felton 1976). Then

$$\sigma_\Phi^2 = \sum \frac{1}{V_{max}^2} \tag{6.8}$$

As noted in Section 6.2, a correction must be applied to the observed space density of stars with $v_{tan} \geq v_{cutoff}$ in order to obtain the space of density of halo stars. Thus,

$$\Phi_{halo} = \frac{1}{\chi}\Phi_{obs} \tag{6.9}$$

The discovery fraction χ is a function of position on the sky. In our case, we compute χ for each field in the survey. This procedure is described in Section 6.4.2.

A check on the completeness of the survey may be found by considering

$$\left\langle \frac{V}{V_{max}} \right\rangle = \left\langle \left(\frac{d}{d_{max}}\right)^3 \right\rangle \tag{6.10}$$

which considers the ratio of the volume V corresponding to the star's actual distance d to V_{max}. In the case of a spatially uniform sample, such as the halo over the volume probed by this survey, we expect $\left\langle \frac{V}{V_{max}} \right\rangle = 0.5$. We find that eight of our nine fields are within 1σ of 0.5, and conclude that the survey is complete.

6.4.1 Adopted Color-Magnitude Relations

We use the photometry and parallax data compiled by Gizis (1997) to determine color-magnitude relations appropriate for each spectral class of star (M V; sdM; esdM). There are many sdM and esdM with accurate distance determinations available, mainly due to the efforts of the USNO CCD parallax program (Monet et al.

1992), which allows us to determine the following relations:

$$M_I^{sdM} = 4.24 + 2.40 \times (V - I) \tag{6.11}$$

$$M_I^{esdM} = 4.58 + 2.92 \times (V - I) \tag{6.12}$$

These relations are valid for $(V - I) \geq 1.6$. Our survey is sensitive primarily to the fainter redder M subdwarfs, but it is useful to have a luminosity estimator for the bluer subdwarfs. For these stars, the above linear relations are no longer appropriate, due to a "kink" in the main sequence at $V - I \sim 1.5$ (c.f., D'Antona & Mazzitelli 1996; Baraffe et al. 1997). Unfortunately, there are few parallax K subdwarfs and fewer with red (RI) photometry. The Hipparcos mission, however, has determined parallaxes for many G subdwarfs. We therefore fit a linear relation to the Hipparcos G subdwarfs supplemented by the available K subdwarfs from the Fourth Edition of the Yale Parallax Catalog (van Altena et al. 1996). In this region, models predict that for $[m/H] \lesssim -1$ the absolute magnitudes are insensitive to metallicity (Baraffe et al. 1997). We select only stars with $v_{tan} > 220$ km s^{-1} to ensure a halo sample. The data are shown are in Figure 6.5. There are 29 subdwarfs with $\frac{\sigma_\pi}{\pi_t} < 0.2$, $5 \leq M_V < 10$, and $0.5 < V - I < 1.4$. We find

$$M_I^{esdG/sdG} = 2.99 + 3.16 \times (V - I) \tag{6.13}$$

This slope is consistent with the slope measured in globular clusters by Santiago et al. (1996). We obtain an approximation to the main sequence relation in the "kink" by imposing continuity. This implies

$$M_I^{sdK} = 2.72 + 3.35 \times (V - I) \tag{6.14}$$

$$M_I^{esdK} = -5.47 + 9.20 \times (V - I) \tag{6.15}$$

The slope for the "esdK" is probably too steep but is adequate for our purposes, since our survey is aimed at the M subdwarfs.

Disk population stars with $V - I < 2.9$ are well described by the relation derived by Stobie et al. (1989). The high velocity stars in Gizis (1997) which are spectroscopically classified as M V stars nevertheless lie ~ 0.5 magnitudes below the disk mean sequence. Since the "M V" stars in our survey have high velocities, we assume that they are equally subluminous and therefore obey the following relationship:

$$M_I^{K,M\ V} = 3.39 + 2.34 \times (V - I) \tag{6.16}$$

These above relations can only be used for the NGP field, where we have V and I photometry. Unfortunately most sdM and esdM lack R photometry, while we have only R and I data for the remaining fields in our survey. Hence we have determined the relationship between $(V-I)_C$ and $(r-i)_P$ using Equation 6.2 and Bessell's (1990) VRI_C photometry of nearby stars. We find:

$$\begin{aligned}(r-i)_P &= 0.147746 + 0.452023(V-I)_C - 0.393217(V-I)_C^2 + \\ &\quad 0.360629(V-I)_C^3 - 0.101972(V-I)_C^4 + 0.009343(V-I)_C^5 \end{aligned} \tag{6.17}$$

Applying this transformation to the $(V-I)_C$ color of each parallax star, we find that

$$M_I^{sdM} = 5.37 + 3.53 \times (r-i)_P \tag{6.18}$$

$$M_I^{esdM} = 5.96 + 4.29 \times (r-i)_P \tag{6.19}$$

Relations 6.18 and 6.19 are valid for $(r-i)_P \geq 0.77$. It is possible that the R-I,V-I transformation for the extreme M subdwarfs is not the same as that for disk M dwarfs. Currently available photometry (Gizis 1997) is unable to resolve the issue, since the photometry comes from many different sources which are known to require transformations (Bessell & Weis 1987). — some, but not all, of the esdM are $\sim$

0.05 bluer in $(R-I)_C$ than the $(V-I)_C$ color would predict. Given the known sources of uncertainty in the photographic photometry and trigonometric parallaxes, this possible color error is of little significance. The spectrophotometry presented in Chapter 4 shows that there is no significant color term for the sdM stars or the earliest (esdK7; esdM0.0) extreme subdwarfs.

For stars with $(r-i)_P < 0.77$, we transform Equations 6.13, 6.14 and 6.15 and obtain:

$$M_I^{esd/sdG} = 1.98 + 8.26 \times (r-i)_P \tag{6.20}$$

$$M_I^{sdK} = 3.51 + 5.93 \times (r-i)_P \tag{6.21}$$

$$M_I^{esdK} = -3.30 + 16.28 \times (r-i)_P \tag{6.22}$$

Equation 6.20 applies for $0.31 < (r-i)_P < 0.66$.

For the high-velocity M V stars, we again assume they are 0.5 magnitudes subluminous relative to the disk sequence. For $(r-i)_P \geq 1.1$, we use TRM's disk sequence (Equation 6.4) with a 0.5 magnitude offset. For bluer stars, we derive a disk main sequence from the Bessell (1990) data. Applying the 0.5 magnitude offset, we obtain:

$$M_I = 4.31 + 3.50 \times (r-i)_P \tag{6.23}$$

6.4.2 Kinematic Corrections

The luminosity function computed using the above technique, although correct in shape, represents only the fraction of the halo that has $V_{tan} \geq 200$ km s^{-1} (in the directions of our particular fields). This detected fraction depends upon the kinematics of the halo. Given a kinematic model of the halo, we can calculate the discovery fraction (χ) for each field.

The halo can be fairly well represented by Gaussian distributions in U,V, and W.[2] BC have shown that variations of ± 5 km s^{-1} in the kinematic parameters ($\langle V \rangle$,σ_U, σ_V,σ_W) imply variations of less than 4% in χ. Some studies of the Galactic halo, however, have found significantly different kinematic parameters. Specifically, Beers and Sommer-Larson (1995, hereafter BSL) have found substantially hotter halo kinematics based upon a sample of non-kinematically selected metal-poor stars. We have therefore simulated our survey using both the input BC and BSL parameters. For this simulation, we have increased the space density of the halo so that the simulated samples consist of $\gtrsim 10000$ detected stars per field. For a given luminosity function, $\chi_{BSL} \approx 1.53\chi_{BC}$. In Table 6.7, we compare the predictions of the U,V, and W velocity distributions of the two models to the actual data for stars with $M_I > 8.5$. We emphasize that these are the predicted velocity characteristics of the kinematically-biased observed sample, not the true halo kinematics. We also give the probability that the observed data and the model simulations are drawn from the same distributions, as determined by Kolmogorov-Smirnov tests. For the U and W velocities, the predictions of both models are indistinguishable for the data, as verified by the results of Kolmogorov-Smirnov tests. The observed mean V velocity of -193 ± 14 km s^{-1}, however, is consistent with the BC predictions ($\langle V \rangle = -200$ km s^{-1}) and not the BSL predictions ($\langle V \rangle = -250$ km s^{-1}). The KS test confirms this, finding that the BSL model is 1000 times less likely than the BC model for our data set. We therefore adopt the kinematic corrections appropriate for the BC model parameters. These corrections are listed in Table 6.7.

6.4.3 The Observed Luminosity Function

Using the observed photometry and the spectral classifications, we are able to estimate an absolute magnitude and apparent distance modulus using the appropriate color-magnitude relations. In each field, we calculate the luminosity function using the

[2]We use the standard notation of (U,V,W) for the space velocity components, in which U represents the motion towards the Galactic center ($l = 0$,$b = 0$, V represents motion in the direction of Galactic rotation, and W represents motion perpendicular to the Galactic plane.

Equations 6.5 to 6.7. We combine all the fields together to make our best estimate luminosity function, calculated for 0.5 magnitude bins, which is listed in Table 6.5.

We compare our luminosity function to the BC determination of brighter stars as well as the Dahn et al. (1995) measurement of the faint end of the luminosity function. BC estimate absolute magnitudes using the Eggen (1983) distance estimates based upon photometric parallaxes. Since these other surveys report their measurements in terms of M_V, we transform their luminosity function to M_I using the main sequences derived in this paper and the equation

$$\Phi(M_I) = \Phi(M_V) \left| \frac{dM_v}{dM_I} \right| \tag{6.24}$$

For Dahn et al. (1995), we use equation 6.12 since most of their stars will be extreme M subdwarfs (we do not transform the bluer stars which lie in the esdK "kink"). Figure 6.6 shows that our results are consistent with the Dahn et al. measurement, which is based upon trigonometric parallaxes.

We divide the BC luminosity function into two categories: $[m/H] \leq -1.5$, corresponding to the esdM; and $[m/H] > -1.5$. We use the CLLA measurements of halo stars to find that 71% of halo stars (defined by their velocity, $V < -220$ km s^{-1}) are in the former category. We then assume for the FGK BC subdwarfs that this metallicity distribution applies in each luminosity bin (this assumption is clearly only an approximation). We do not consider the $M_V > 9$ bins since the photometric relation used by BC is not a good description of esdK and esdM stars. The two resulting BC luminosity functions are shown in Figure 6.6.

Note also the dramatic dip in the BC luminosity function at $M_V \approx 8$, $M_I \approx 7$ which BC note is a 3σ effect. It is now recognized that features in a photometric luminosity function may be the result of features in the mass-luminosity relationship (D'Antona 1986), and the assumption of a smooth power-law has even been used to derive the mass-luminosity relation (Kroupa et al. 1995). Reid & Gizis (1997) have shown that features in the color-magnitude relation can cause spurious dips and peaks in the photometric luminosity function for the disk. The dip in the BC

luminosity function is suspiciously close to the "kink," which is observed in globular cluster color-magnitude diagrams and predicted theoretically (D'Antona & Mazzitelli 1996). We speculate that this "kink" may be responsible for the BC dip; that is, the mean color-magnitude relation used to estimate M_V may introduce systematic biases in $\Phi(M_V)$. As can be seen in Figure 6.5, the available data for K subdwarfs are not sufficient to pin down the kink in the field.

It is likely, however, that there is an additional problem with the BC luminosity function. As can be seen from Figure 6 of Dahn et al. (1995), the BC luminosity function has half as many stars as the trigonometric parallax surveys (Schmidt 1975; Dahn et al. 1995) in the range $6 < M_V < 10$. This suggests that there is some bias or incompleteness in the BC sample. The BC luminosity function is, however, valuable because it has much better number statistics in this range, and thus provides better constraints on the slope of the luminosity function (modulo the problems with photometric surveys noted above). We therefore have "corrected" the BC luminosity function upwards by a factor of two, as seen in Figure 6.7. Note that the implied luminosity function that joins our luminosity function to the BC luminosity function is now shallower and not discontinuous.

6.5 The Mass Function

In order to derive a mass function (Ψ, in units of solar masses per cubic parsec per solar mass) from the luminosity function (Φ), we require knowledge of the mass-luminosity relation. Specifically,

$$\Psi(Mass) = \Phi(M_I)\frac{dM_I}{dMass} \tag{6.25}$$

As emphasized by D'Antona (1986), the results depend on the slope of the mass-luminosity relationship, which remains uncertain. Unfortunately, there are no empirical data on masses of cool metal-poor stars, so we must rely upon model calculations. In Figure 6.8 and 6.9, we plot the mass function derived for the sdM and the esdM

in the survey using the model of Baraffe et al. (1997). The points at $M < 0.35M_{\odot}$ are the results for this survey. The higher mass points in the two figures are from BC and will be discussed separately.

Our mass function gives an estimate of the relative metallicity distribution at $[m/H] < -1.5$ (esdM) and $[m/H] > 1.5$. For the CLLA sample of FGK subdwarfs, 71% of the 136 halo stars have $[m/H] < -1.5$; implying that if the mass function of the two metallicity groups is similar, the number ratio of esdM/sdM should be 2.45 at a given mass. We find that at $0.18M_{\odot}$, the density ratio is $\frac{0.00950}{0.00425} = 2.24$. Given the uncertainties, this is essentially perfect agreement. This suggests that in the halo, the mass function is invariant over a wide range of metallicity, at least if we compare the $\sim 0.7M_{\odot}$ stars to the $\sim 0.15M_{\odot}$ stars.

Our data, however, provide a poor constraint on the form of the mass function. Over the mass ratio we sample, the power-law indices $0 < \alpha < 2$ are all acceptable fits, especially taking into account the uncertainties in the mass-luminosity relationship. A strongly rising ($\alpha > 2$) mass function below $0.2M_{\odot}$ is ruled out. For constraints over a larger mass range, we can compare our data to BC's data for brighter stars. We transform their luminosity function using the same mass-luminosity relations. The results are plotted in Figure 6.8 and favor a steep power-law ($\alpha \approx -2$). We believe, however, that this is the result of using the original BC luminosity function which may be a factor of two too low. Note especially that the mass function is discontinuous just where the two sources meet. The mass function resulting from the revised luminosity function is shown in Figure 6.9. A power-law of $\alpha \approx -1.35$ is consistent with the data for both lower and higher metallicity stars. As noted above, the dip in the BC luminosity function, which now appears as a dip in the mass function, may be an artifact of the linear main sequence adopted by BC.

The mass function that we have derived is somewhat steeper than that we have derived previously for the disk ($\alpha = 1.05$, Reid & Gizis 1997), although the differences in technique and the uncertainties in mass-luminosity relations require us to view this difference as merely suggestive. Indeed, Kroupa et al. (1993) have derived a slope $\alpha = 1.3$ for disk stars, which would be in agreement with our derived mass function.

We conclude that there is at most a weak difference between the field metal-poor Population II and the disk near-solar metallicity mass functions.

6.6 Globular Clusters

Since the installation of WFPC2, HST has been able to observe faint stars in globular clusters to nearly the hydrogen burning limit. To date, I-band luminosity functions have been published for the clusters ω Cen (Elson et al. 1995), M 15 (De Marchi and Paresce 1995, 47 Tuc (De Marchi and Paresce 1995, NGC 6397 (Paresce et al. 1995; Cool et al. 1996), and NGC 6656 (De Marchi and Paresce 1997). These luminosity functions peak near $M_I \approx 9$, declining for fainter stars. As discussed by all of the authors noted above, it is extremely difficult to transform these luminosity functions into reliable mass functions based upon the present theoretical models. De Marchi and Parsece (1997) have argued that, at least for the lowest metallicity clusters, this decline is not due to the loss of the lowest-mass cluster stars but is an intrinsic feature of the clusters. In addition to theoretical calculations (Richer et al. 1991) that the mass function at large core radius (in the absence of tidal stripping) is quite close to the Initial Mass Function (IMF), they find that the two globular clusters (NGC 6397 and NGC 6656) with similar metallicity but very different dynamical histories have nearly identical luminosity functions. They show the drop then implies with present day models that the initial mass function "flattens out and probably drops below $\sim 0.2 M_\odot$." Our luminosity function shows no evidence for a dramatic drop at $M_I > 9$. Figure 6.10 plots our luminosity function with ω Cen and M15. Our luminosity function is completely consistent with ω Cen, which shows a flat luminosity function at the faintest magnitudes. It appears to be inconsistent at the $2 - 3\sigma$ level with M15. Assuming our luminosity function is correct, the difference in the luminosity function suggests that the mass function of field stars has more very-low-mass stars than globular clusters. If the globular cluster present-day mass functions are indeed the IMFs, then this is important evidence that at the lowest masses, star formation is a function of environment. Note that we have found in

Gizis (1997) that the HR diagram of the properly classified sdM and esdM agrees with the HST observations of globular clusters; so the difference is unlikely to be due to stellar physics. We note that Reid (1997) has derived distances to many globular clusters and found that they are more distant than previously thought. This increases the discrepancy between the M15 and the field luminosity functions, since the peaks are made brighter by ~ 0.3 magnitudes. The agreement between our data and ω Cen suggests that the ω Cen mass function would provide the best estimate of the initial mass function.

6.7 Summary

We have derived a new estimate of the space density of very low mass metal-poor stars. Comparison to other surveys shows that we are in agreement with the Dahn et al. (1995) survey based upon trigonometric parallaxes of LHS catalog stars. We find that a mass function with a power-law slope $\alpha = 1.35$ matches the data. Most importantly, there is no evidence of a steep decrease or increase of the mass function below $0.2M_{\odot}$.

Our survey has also resulted in an independent measure of the properties of the Population II halo from very low mass stars. The kinematics of the M subdwarfs are consistent with the results of nearby surveys, such as Bahcall & Casertano (1986). Specifically, our local sample of metal-poor sdM and esdM have kinematics consistent with prograde rotation about the Galactic center. This is consistent with higher mass stars, which have prograde rotation for local stars but retrograde rotation at for halo sample high above the plane (CLLA; Majewski 1993).

We find that the esdM are 2.5 times as common as sdM at $\sim 0.2M_{\odot}$. This is consistent with the relative numbers of metal-poor ($[m/H] \leq -1.5$) and metal-rich ($[m.H] > -1.5$) G subdwarfs found by CLLA. Note that the two metallicity scales are comparable because Gizis & Reid (1997) have found agreement between the CLLA metallicities of FGK subdwarf primaries with metallicities based upon G97. The agreement of the metallicity distribution at both low and high mass implies that the

mass function is not a strong function of metallicity for the low mass halo stars. This result is supported by the general similarity of the mass functions derived for the two metallicity bins considered; however, this result depends upon uncertain model mass-luminosity transformations.

Acknowledgments

We thank Chris Tinney and Mike Irwin for assistance with the plate scans and the staff of Palomar Observatory for their capable support. J.E.G. is grateful for partial support through Greenstein and Kingsley Fellowships as well as NASA grants GO-05353.01-93A, GO-05913.01-94A, and GO-06344.01-95A, This work is based partly on photographic plates obtained at the Palomar Observatory 48-inch Oschin Telescope for the Second Palomar Observatory Sky Survey which was funded by the Eastman Kodak Company, the National Geographic Society, the Samuel Oschin Foundation, the Alfred Sloan Foundation, the National Science Foundation grants AST84-08225, AST87-19465, AST90-23115 and AST93-18984, and the National Aeronautics and Space Administration grants NGL 05002140 and NAGW 1710. This research has made use of the Simbad database, operated at CDS, Strasbourg, France.

Bibliography

Adams, F.C., & Fatuzzo, M. 1997, ApJ, 464, 256

Ake, T.B., & Greenstein, J.L. 1980, ApJ, 240, 859

Alcock, C. et al. 1997, ApJ, 486, 697

Allard, F., & Hauschildt, P.H. 1995, ApJ, 445, 433

Bahcall, J.N., & Casertano, S. 1986, ApJ, 308, 347

Baraffe, I., Chabrier, G., Allard, F., and Hauschildt, P.H. 1997, A&A, in press

Beers, T.C., & Sommer-Larsen, J. 1995, ApJS, 96, 175

Bessell, M.S. 1986, PASP, 98, 1303

Bessell, M.S. 1990, A&AS, 83, 357

Bessell, M.S., & Weis, E.W. 1987, PASP, 99, 617

Clemens, J.C., Reid, I.N., Gizis, J.E., & O'Brien, M.S., 1997, ApJ, submitted

Cool, A.M., Piotto, G., & King, I.R. 1996, ApJ, 468,, 655

Cousins, A.W.J. Mem.R.A.S., 77, 223

Dahn, C.C., Liebert, J., Harris, H.C., & Guetter, H.H. 1995, The Bottom of the Main Sequence – And Beyond, edited by C.G. Tinney (Berlin, Springer), p.239

D'Antona, F. 1986, ApJ, 320, 653

D'Antona, F., and Mazzitelli, I. 1996, ApJ, 456, 329

Dawson, P.C. 1986, ApJ, 311, 984

De Marchi, G., & Paresce, F. 1995a, A&A, 304, 202

De Marchi, G., & Paresce, F. 1995b, A&A, 304, 211

De Marchi, G., & Paresce, F. 1997, ApJ, 476, L19

Elson, R.A.W., Gilmore, G.F., Santiago, B.X., & Casertano, S. 1995, AJ, 110, 682

Eggen O.J. ApJS, 51, 183

Felton, J.E. 1976, ApJ, 207, 700

Gizis, J.E. 1997, AJ, 113, 806

Gizis, J.E., & Reid, I.N. 1996, AJ, 111, 365

Hartwick, F.D.A., Cowley, A.P., & Mould, J.R. 1984, ApJ, 286, 269

Hawley, S.L., Gizis, J.E., & Reid, I.N. 1996, AJ, 112, 2799

Kroupa, P, Tout, C.A., & Gilmore, G. 1993, MNRAS, 262, 545

Luyten, W.J. 1939, Publ. Minnesota, 2, 121

Luyten W. J., 1979-1980, New Luyten Catalogue of Stars with Proper Motions Larger than Two Tenths of an Arcsecond, (Minneapolis, University of Minnesota), computer-readable version on ADC Selected Astronomical Catalogs Vol.1 - CD-ROM

Marcy, G.W., & Benitz, K.J. 1989, ApJ, 344, 441

Monet, D.G., Dahn, C.C., Vrba, F.J., Harris, H.C., Pier, J.R., Luginbuhl, C.B., & Ables, H.D. 1992, AJ, 103, 638

Murray, S.D., & Lin, D.C. 1996, ApJ, 467, 728

Oke, J.B., & Gunn, J.E. 1982, PASP, 94, 586

Paresce, F., De Marchi, G., & Romaniello, M. 1995, ApJ, 440, 216

Picard, A. 1991, AJ, 102, 445

Reid, I.N. 1997, AJ, 114, 161

Reid, I.N., Hawley, S.L., & Gizis, J.E. 1995, AJ, 110, 1838

Reid, I.N., & Gizis, J.E. 1997, AJ, 113, 2246

Richer, H.B., & Fahlman, G.G. 1992, Nature, 358, 383

Richer, H.B. Fahlman, G.G., Buonanno, R., Fusi Pecci, F., Searle, L., & Thompson, I.B. 1991, ApJ, 381, 147

Schmidt, M. 1968, ApJ, 151, 393

Schmidt, M. 1975, ApJ, 202, 22

Stobie, R.S., Ishida, K., & Peacock, J.A. 1989, MNRAS, 238, 709

Tinney, C.G. 1993, ApJ, 414, 279

Tinney, C.G., Reid, I.N., & Mould, J.R. 1993, ApJ, 414, 254

Thuan, T.X., & Gunn, J.E. 1976, PASP, 88, 543

van Altena, W.F., Lee, J.T., & Hoffleit, E.D. 1995, The General Catalogue of Trigonometric Stellae Parallaxes, Fourth Edition (Schenectady, L. Davis Press)

Zinnecker, H. 1984, MNRAS, 210, 43

Table 6.1: Survey Plates

Field	α (B1950)		δ	Source	Epoch	Plate	Epoch
829	02	00	+00	UK/PII	1987.83	EO852	1953.78
831	02	40	+00	UK/PII	1981.92	EO1283	1954.90
						EO1453	1955.81
832	03	00	+00	UK/PII	1986.89	EO363	1951.69
						EO1453	1955.81
262	10	15	+45	POSSII	1987.34	EO672	1953.12
NGP	13	04	+29	Palomar	1976.23	EO1393	1955.29
868	15	00	+00	UK/PII	1987.30	EO1402	1955.30
						EO1613	1957.32
513	15	00	+25	POSSII	1987.34	EO102	1950.35
						EO87	1950.30
						EO1390	1955.29
						EO1092	1954.49
889	22	00	+00	POSSII	1990.55	EO1146	1954.57
890	22	20	+00	POSSII	1990.82	EO364	1951.69
						EO1146	1954.57

Table 6.2: Relative to Absolute Proper Motions

Field	$\Delta\mu_\alpha$	$\Delta\mu_\delta$	σ_α	σ_δ
	mas	mas	mas	mas
262	2.6	5.2	13.0	13.7
513	4.4	4.2	12.1	11.8
829	-3.7	3.8	14.9	13.9
831	-2.0	2.3	17.0	16.0
832	-4.3	3.9	13.6	12.6
868	3.2	3.3	13.6	12.6
889	-0.2	4.3	10.6	10.6
890	-0.9	3.4	11.9	11.5
NGP	5.0	3.9	...	...

Table 6.3: Kinematic Corrections

Field	Area (sq. deg)	M_I^{lim}	$1/\chi$
829	25.32	17.3	2.51
831	26.49	17.3	2.57
832	25.32	17.3	2.56
262	14.56	17.3	2.51
NGP	28.00	17.3	2.36
868	25.29	17.3	2.54
513	25.29	17.3	2.58
889	25.30	17.3	3.19
890	25.26	17.3	3.04

Table 6.4: Kinematic Comparison

	Data	BC	BSL
σ_U	144	146	141
Probability (U)		0.65	0.37
$\langle V \rangle$	-193	-200	-250
σ_V	89	90	88
Probability (V)		0.80	8×10^{-4}
σ_W	94	102	113
Probability (W)		0.21	0.26

Table 6.5: Halo Luminosity and Mass Functions

M_I	Φ 10^{-5} pc^{-3}	σ_Φ Mag^{-1}	Mass $M_\odot$	Ψ 10^{-5} pc^{-3}	σ_Ψ $M_\odot^{-1}$
		sdM			
8.5	3.27	0.96	0.30	2.1	
9.0	2.92	0.90	0.24	2.9	
9.5	2.92	1.35	0.20	3.8	
10.0	2.92	2.92	0.16	4.7	
		esdM			
9.5	6.88	2.64	0.18	9.5	
10.0	5.32	2.41	0.15	9.5	
10.5	4.66	3.49	0.13	11.6	

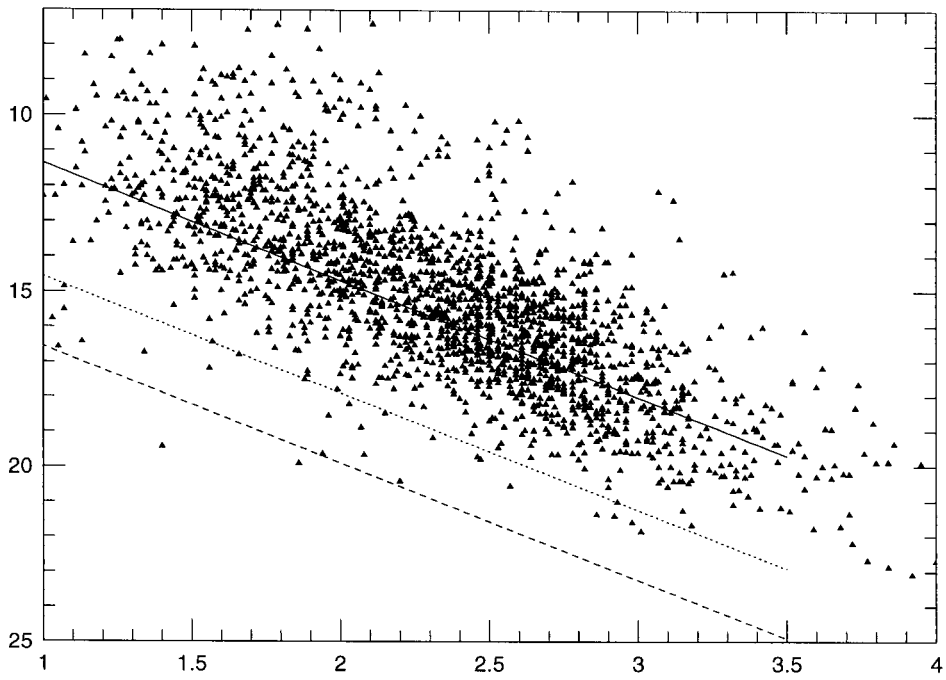

Figure 6.1: A color - reduced proper motion $(V-I, H_V)$ diagram for a nearly volume limited sample of stars within 25 parsecs. The 2111 observable known nearby M dwarfs (Reid et al. 1995; Hawley et al. 1996) are plotted. For some stars, the V-I photometry was estimated on the basis of their spectral type. The solid line plots a disk population using the Stobie et al. (1989) main sequence and $v_{tan} = 50$ km s^{-1} . The dotted line plots the same main sequence with $v_{tan} = 220$ km s^{-1} . The dashed line plots a main sequence that is two magnitudes subluminous, roughly corresponding to the sdM. It is clear that volume limited samples are a poor way of selecting high velocity samples.

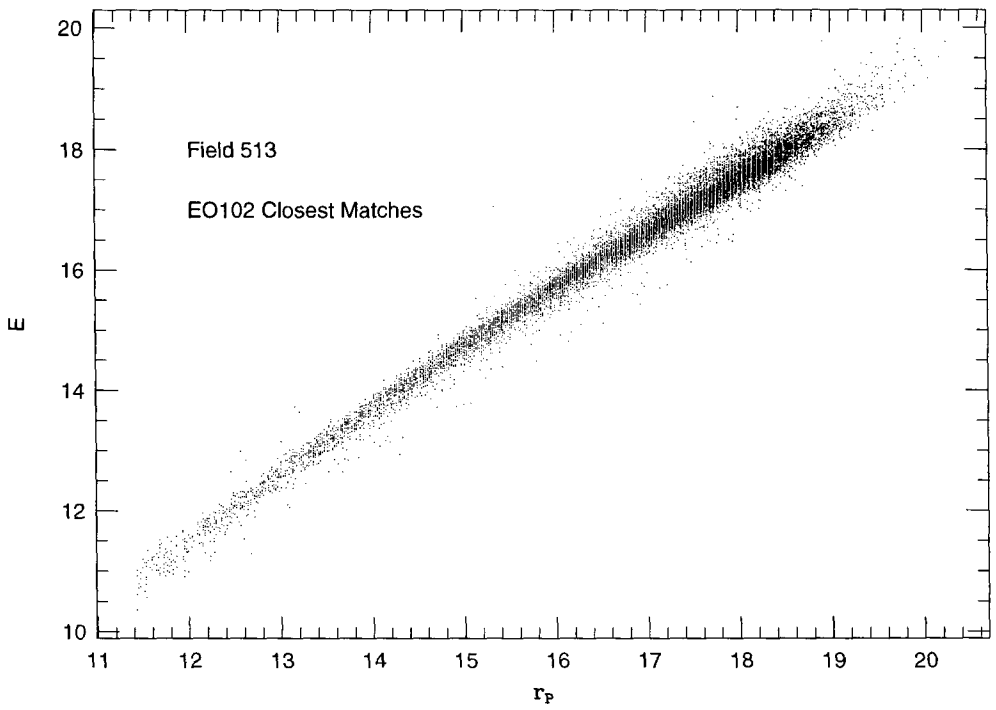

Figure 6.2: Comparison of magnitudes for matches within 3 arcsec for the POSSII 513 dat and POSSI plate E102. The outlier points are due to galaxies and merged sources which are treated differently by the two measuring machines.

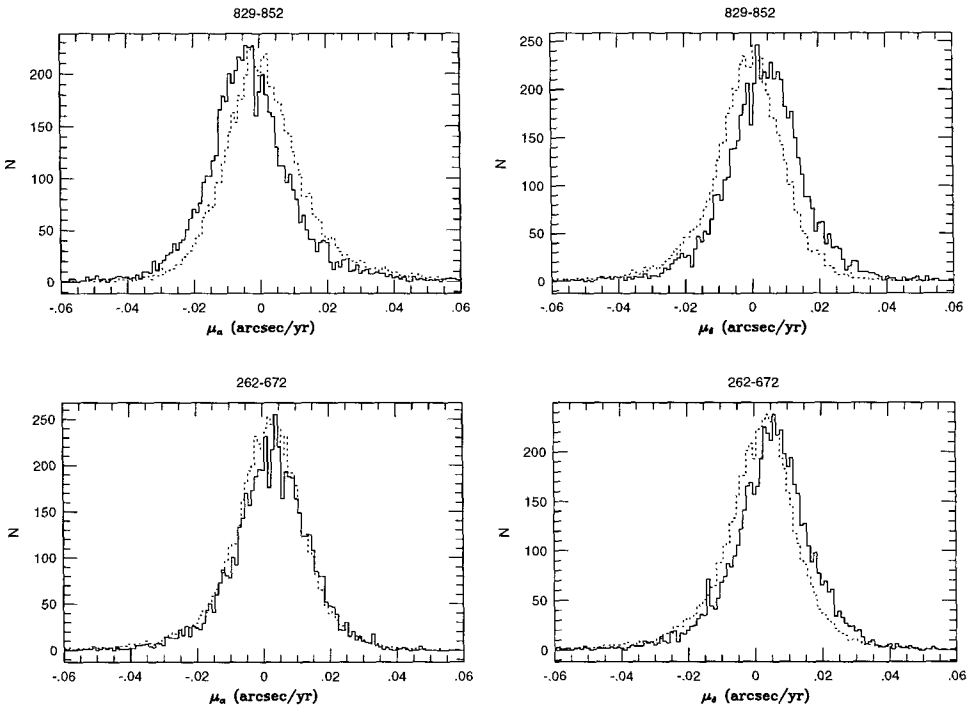

Figure 6.3: Measured relative proper motions for galaxies and stars. The amplitude of the stellar histograms have been scaled down by a factor of ~ 100. The median of the galaxy distribution defined the correction to absolute proper motions.

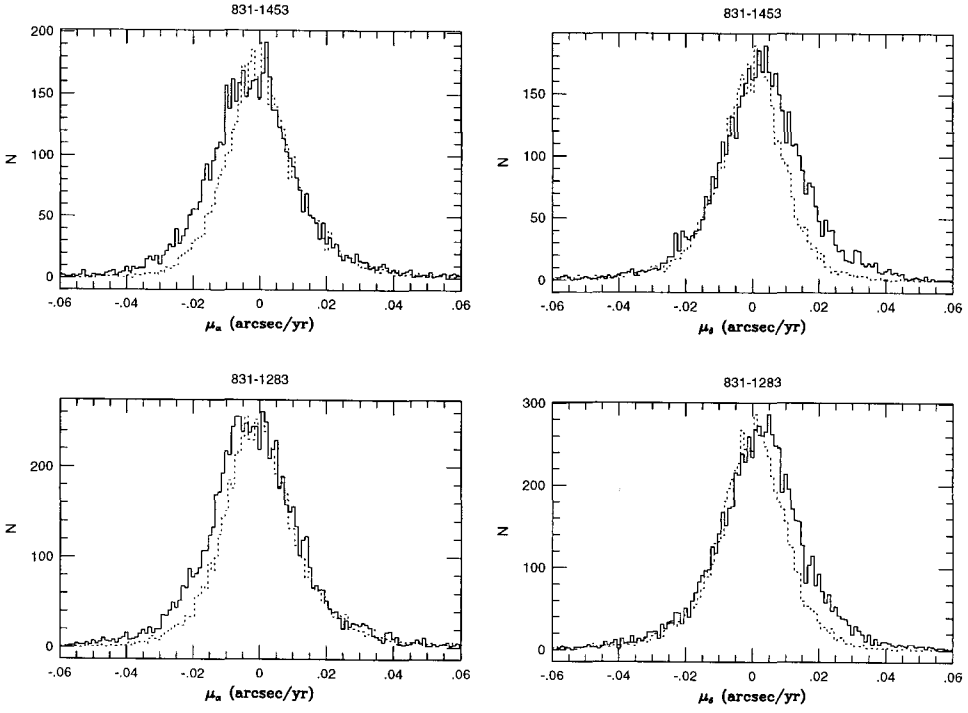
831-1453
N
μ_α (arcsec/yr)
831-1453
N
μ_δ (arcsec/yr)
831-1283
N
μ_α (arcsec/yr)
831-1283
N
μ_δ (arcsec/yr)

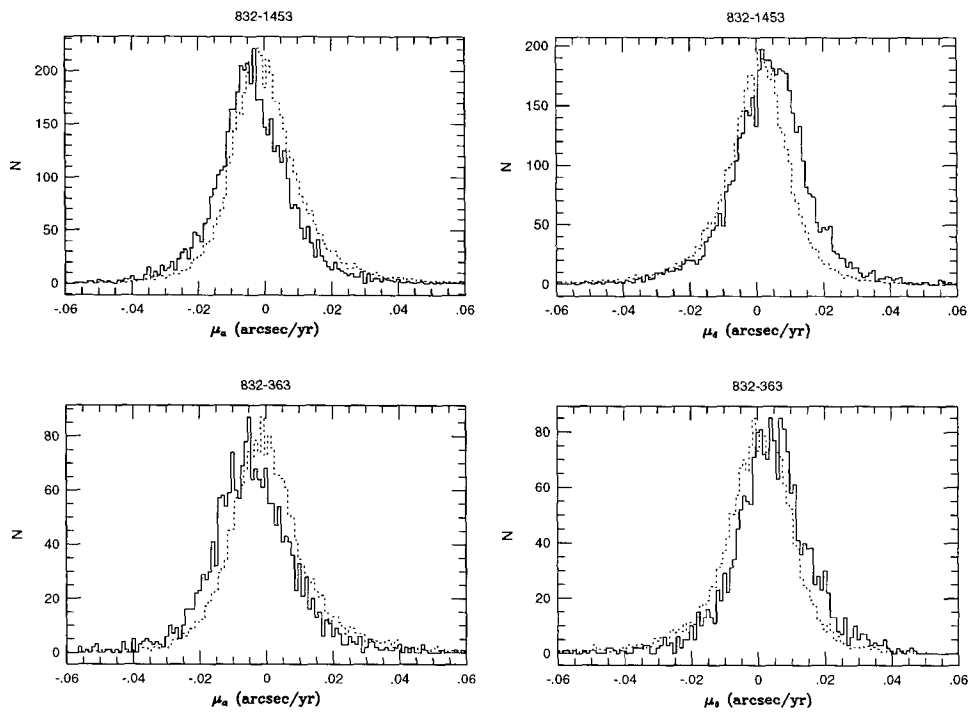
832-1453
N
μ_α (arcsec/yr)
832-1453
N
μ_δ (arcsec/yr)
832-363
N
μ_α (arcsec/yr)
832-363
N
μ_δ (arcsec/yr)

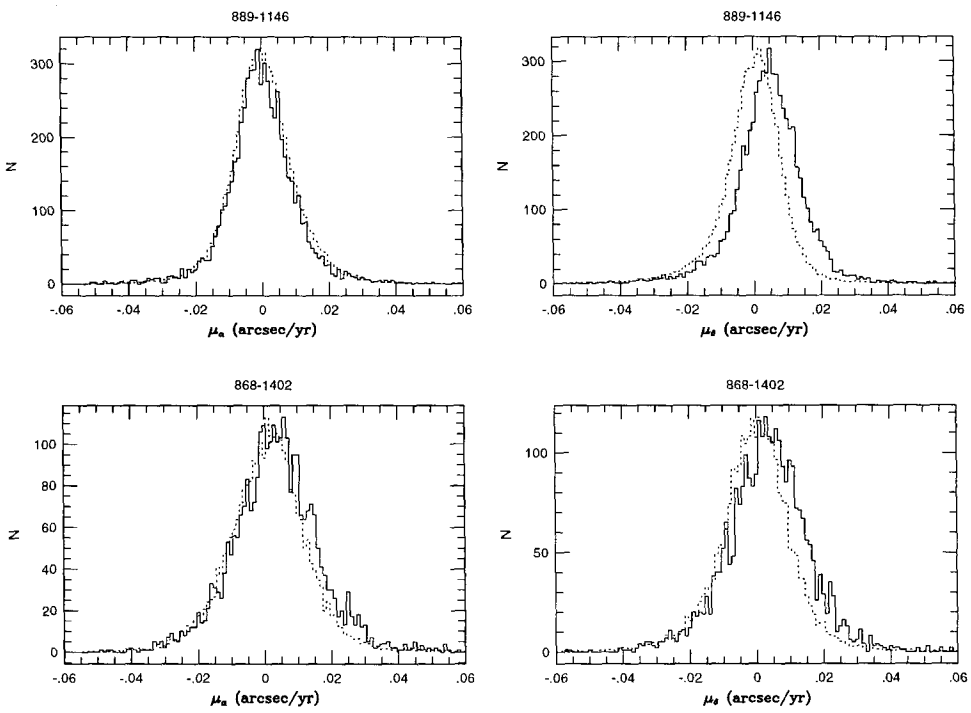
889-1146
N
300
200
100
0
-.06
-.04
-.02
0
.02
.04
.06
μ_α (arcsec/yr)
889-1146
N
300
200
100
0
-.06
-.04
-.02
0
.02
.04
.06
μ_δ (arcsec/yr)
868-1402
N
100
80
60
40
20
0
-.06
-.04
-.02
0
.02
.04
.06
μ_α (arcsec/yr)
868-1402
N
100
50
0
-.06
-.04
-.02
0
.02
.04
.06
μ_δ (arcsec/yr)

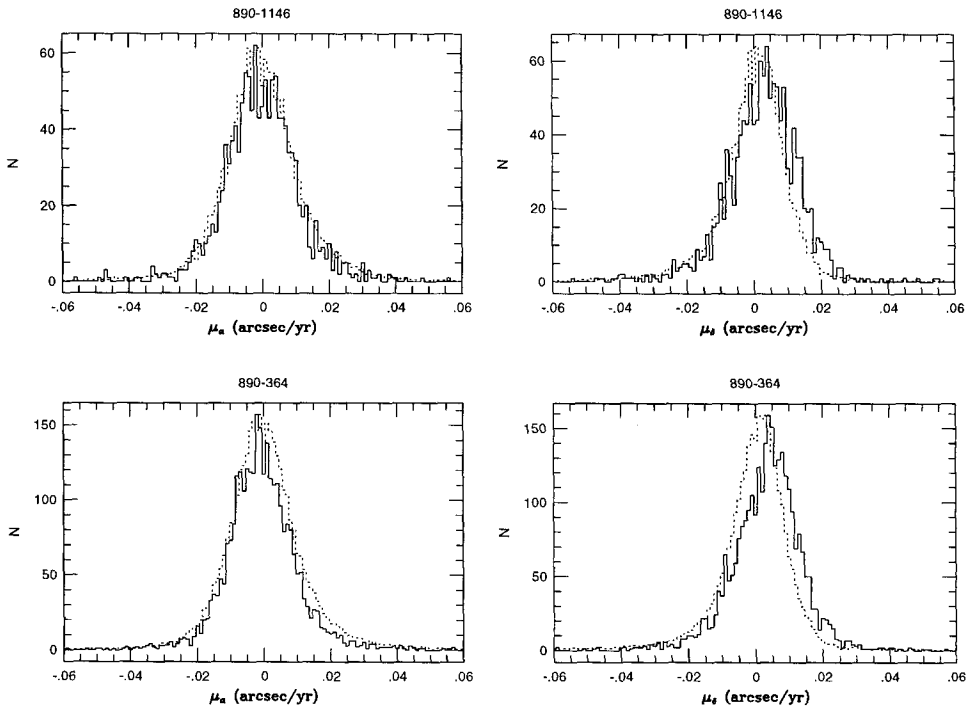
890-1146
N
60
40
20
0
-.06
-.04
-.02
0
.02
.04
.06
μ_α (arcsec/yr)
890-1146
N
60
40
20
0
-.06
-.04
-.02
0
.02
.04
.06
μ_δ (arcsec/yr)
890-364
N
150
100
50
0
-.06
-.04
-.02
0
.02
.04
.06
μ_α (arcsec/yr)
890-364
N
150
100
50
0
-.06
-.04
-.02
0
.02
.04
.06
μ_δ (arcsec/yr)

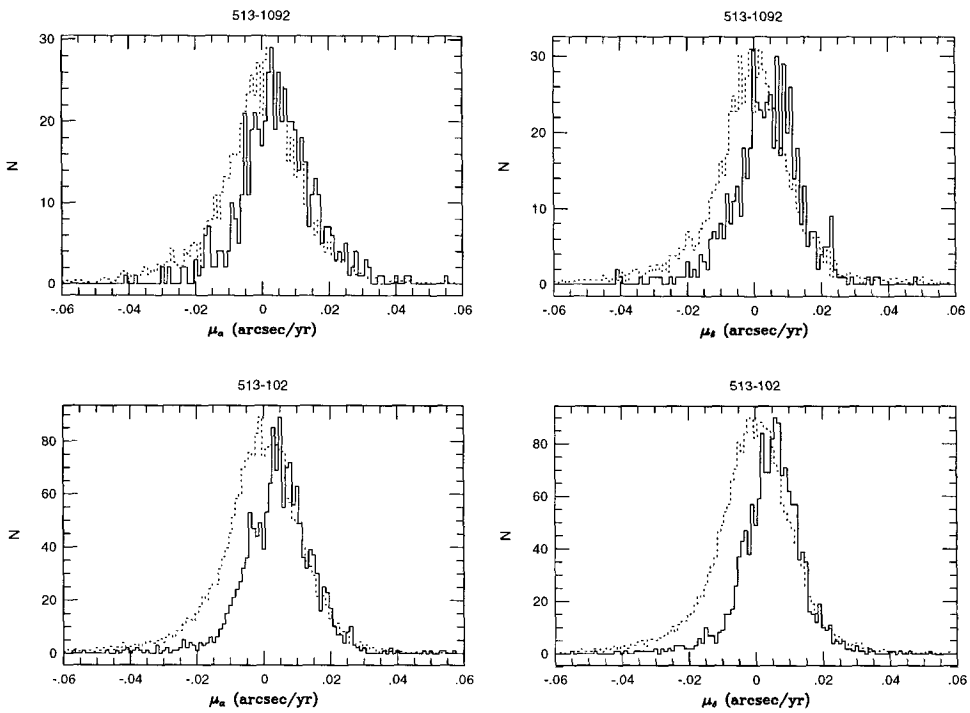
513-1092
N
μ_α (arcsec/yr)
513-1092
N
μ_δ (arcsec/yr)
513-102
N
μ_α (arcsec/yr)
513-102
N
μ_δ (arcsec/yr)

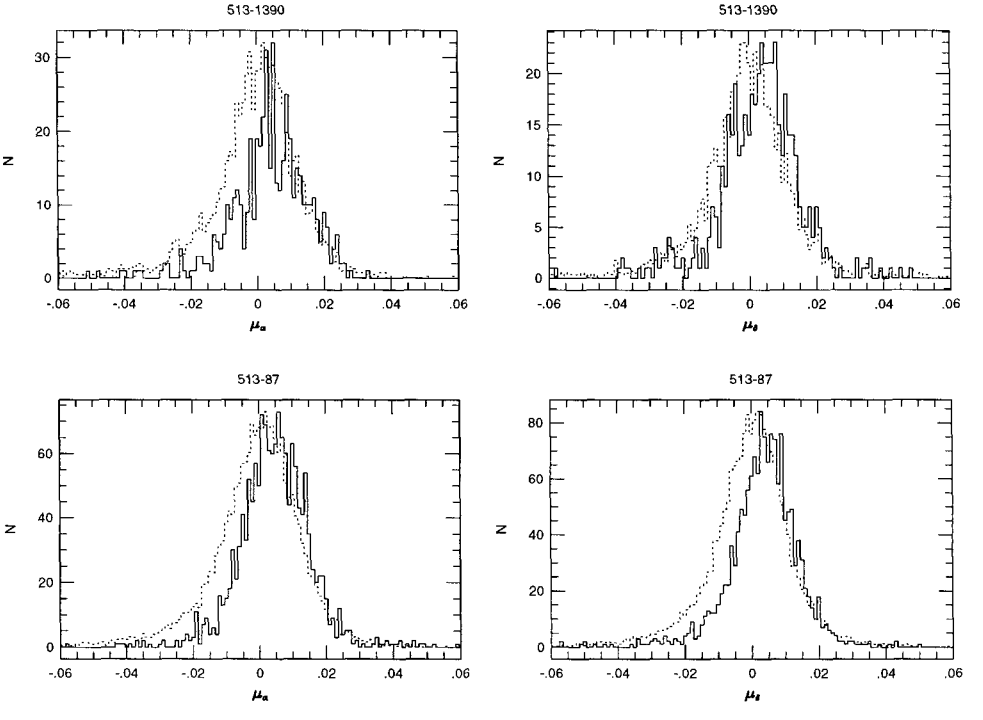
513-1390
N
μ_α
513-1390
N
μ_δ
513-87
N
μ_α
513-87
N
μ_δ

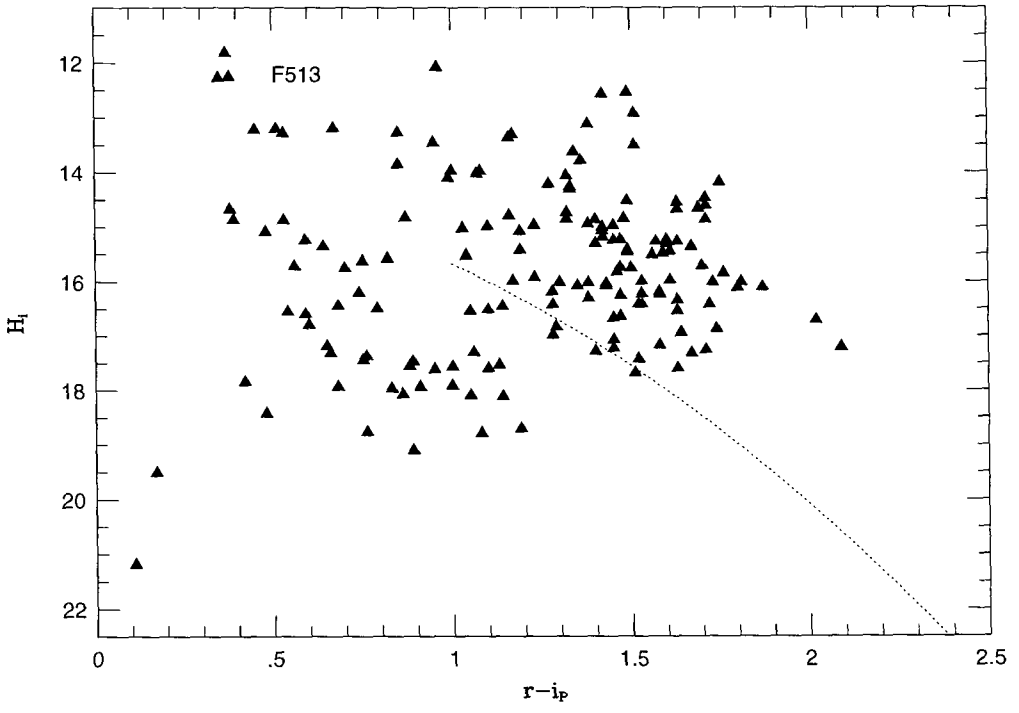

Figure 6.4: The reduced proper motion diagram for Field 513. Halo stars lie below the dotted line, which corresponds to 220 km s^{-1} for near-solar metallicity disk stars.

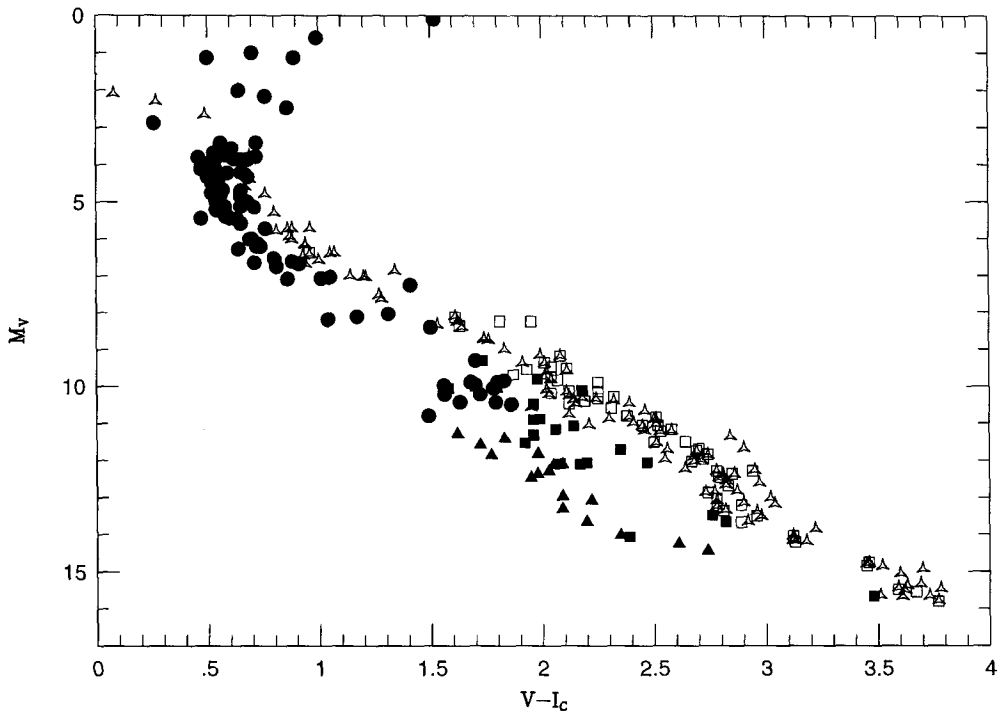

Figure 6.5: The HR Diagram for stars using trigonometric parallaxes. Solid Circles are stars with $v_{tan} > 220$ km s^{-1} from the Yale Parallax Catalog (van Altena et al. 1995 or the Hipparcos Catalog, solid squares are sdM (Chapter 2), and solid triangles are esdM. The disk sequences is shown using nearby stars (three-cornered stars and open squares)

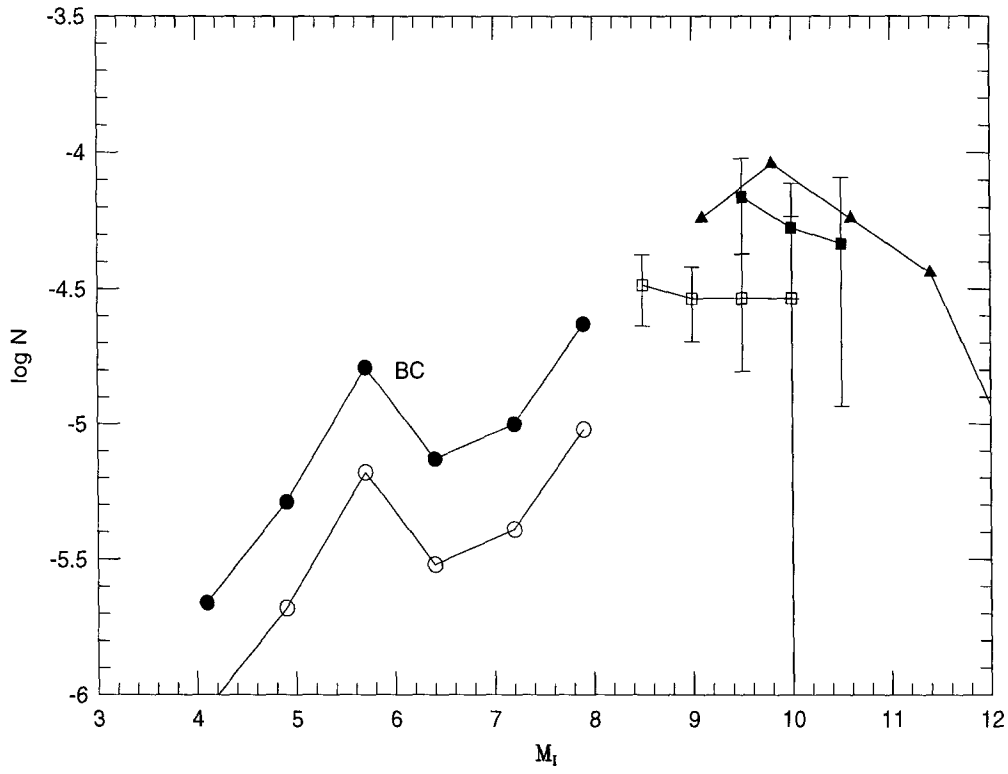

Figure 6.6: Our estimated luminosity function for sdM (open squares) and esdM (solid squares). Also shown is the luminosity function determined by Dahn et al. (1995), transformed to M_I, as solid triangles and the luminosity function for higher luminosity halo stars determined by BC. Using the CLLA metallicity distribution, the BC luminosity function has been divided into high (open circle) and low (solid circle) metallicity groups that correspond to the sdM and esdM. Note that the BC luminosity function and our luminosity function together are very steep and appear to be discontinuous.

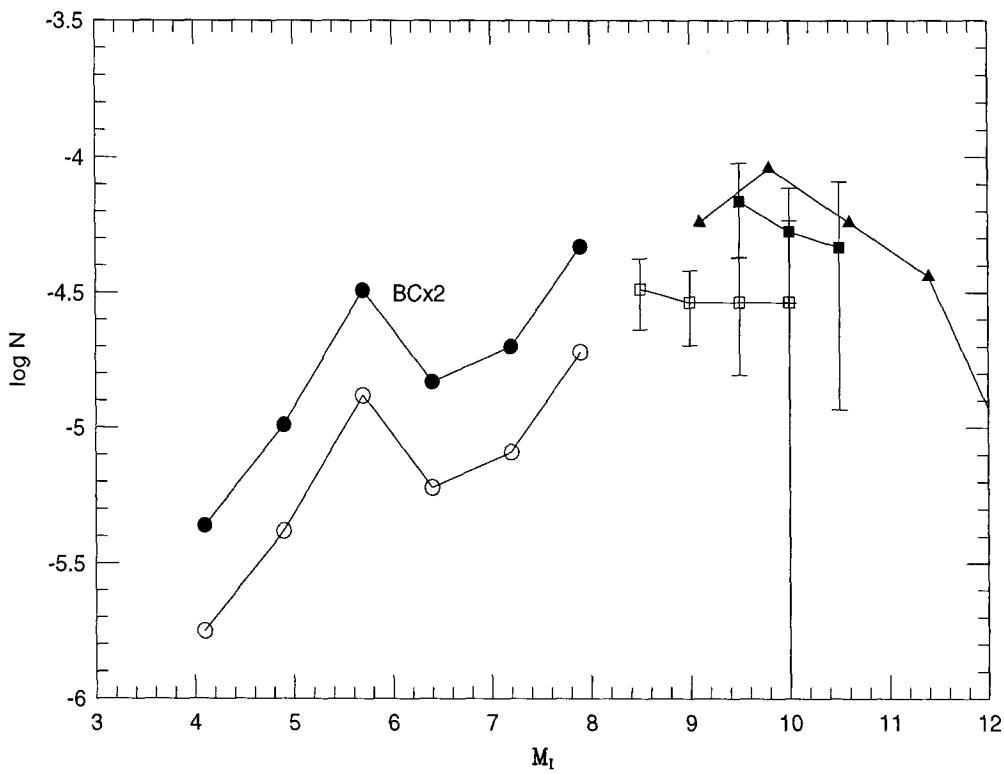

Figure 6.7: The same as the previous figure, except that the BC luminosity function has been multiplied by a factor of two to bring it into agreement with the trigonometric parallax samples. Note that the BC and our luminosity function now imply a much shallower slope to the luminosity function.

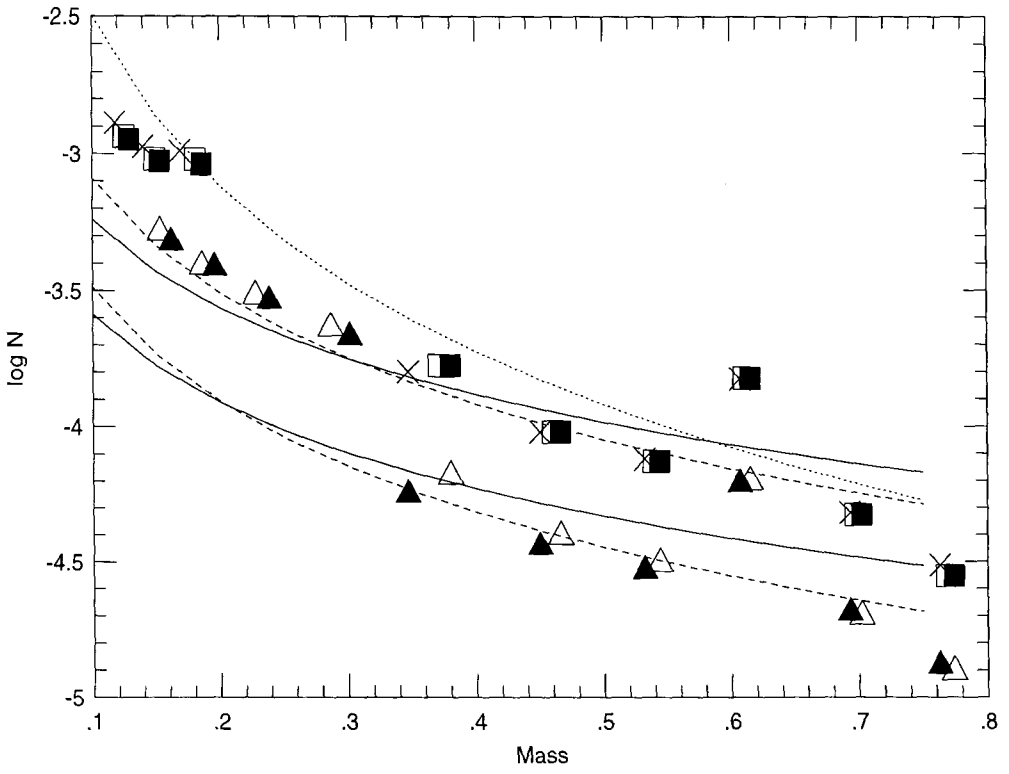

Figure 6.8: The derived mass function of the halo for the extreme M-subdwarfs (esdM) and M-subdwarfs (sdM). The data points for $M < 0.2M_{\odot}$ (esdM) and $M < 0.35M_{\odot}$ (sdM) are from our survey and correspond to $r - i_P > 0.8$. The higher mass data points are from the Bahcall & Casertano (1986) luminosity function. The models of Baraffe et al. (1997) have been used for the transformation. The esdM have been transformed using $[m/H] = -1.3$ (solid squares), $[m/H] = -1.5$ (open squares), and $[m/H] = -2.0$ (crosses). The sdM have been transformed with the $[m/H] = -1.0$ (solid triangles) and $[m/H] = -1.3$ (dotted line) models. The lines show power-law mass functions with slope $\alpha = 1.05$ (solid line), $\alpha = -1.35$ (dotted line), and $\alpha = -2.0$ (dashed line). The mass function shows clear evidence for a discontinuity where we have joined the BC survey to our own.

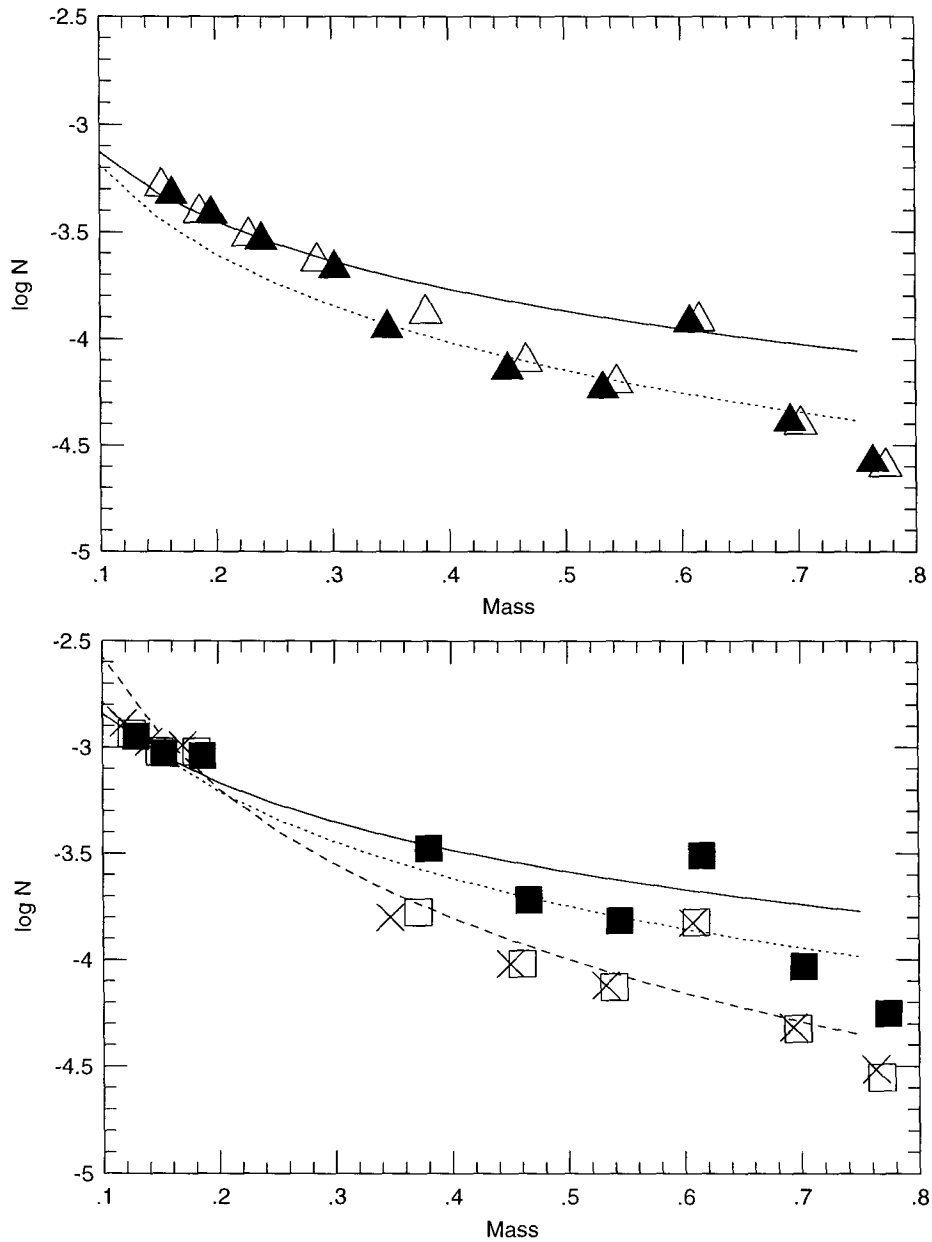

Figure 6.9: We plot the mass function derived using the "corrected" BC luminosity function. Symbols are the same as for the previous figure. The mass function is now smooth, consistent with a power-law of $\alpha \approx 1.35$.

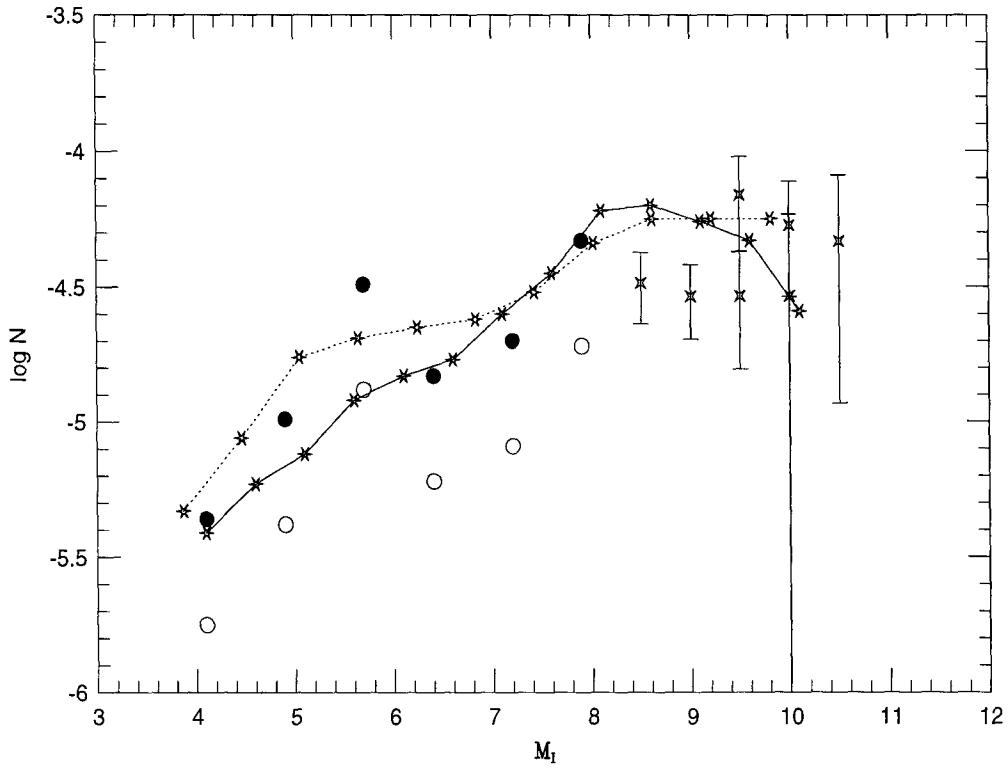

Figure 6.10: The globular clusters ω Cen (dotted line) and M15 (solid line) compared to the esdM and sdM luminosity functions. The luminosity function of ω Cen is in excellent agreement with . M15, in contrast, is discrepant with the steep decline in the cluster luminosity function not detected in the field. If the clusters are more distant, as advocated by Reid (1997), the the M15 discrepancy becomes worse.

Chapter 7 Summary

7.1 Summary of our Results

We have presented a spectroscopic classification scheme that allows metal-poor cool stars to be easily characterized in a well-defined system. This should allow the all-too-common confusion over whether or not a given star is significantly metal-poor to be avoided in the future. The use of CaH and TiO features allows cool stars to be classified in terms of both temperature and metallicity. Two useful subgroups of subdwarfs can be identified: the M subdwarfs (sdM) which have $[m/H] \approx -1.2$ and the extreme M subdwarfs (esdM) which have $[m/H] \approx -2$. This thesis has shown that despite the remaining discrepancies between observations and model atmospheres, the properties of M subdwarfs can be understood. The metallicities derived from model atmospheres are in agreement with external checks such as globular clusters, (some) interior models, and G subdwarf/ M subdwarf pairs.

We have also found two highly active M subdwarfs. Normally a sign of youth, we show that the short-period binary nature of the two systems is the most likely explanation for their activity. Although drawing conclusions from a sample of only two stars is risky, it appears that the metal-poor stars have weaker activity than young open cluster stars with similar rotation rates. This is consistent with the behavior seen in higher mass stars.

Counts of faint proper motion stars indicate that many M subdwarfs are present in the Galactic halo. The resulting mass function, although uncertain, appears to be consistent with a power-law and is at most mildly different from the disk near-solar metallicity mass function. This implies that star formation is remarkably similar at all measurable times in Galactic history, despite the considerable evolution of the physical surroundings.

In addition, the proper motion survey has demonstrated that, as expected, the

very low mass stars of the halo have similar properties to their higher mass counterparts. Specifically, the metallicity distribution and kinematics are consistent at the two masses. It is now clear that there are no shocking surprises lurking at lowest masses of the Population II. On the other hand, M subdwarfs are becoming viable alternative probes of the halo. Their cool temperatures mean that different elements can be investigated

7.2 The Future

Future sky surveys (Sloan, 2MASS, etc.) should allow the very bottom of the Population II main sequence to be reached. Color selection, if accurate enough photometry can be obtained, may be most important in the near-future since it will be some time until a deep second epoch survey, allowing selection by proper motion, can be conducted. In addition, these other deep surveys may allow stars cooler than LHS 1742a and LHS 377 to be identified and studied. The models predict that cooler metal-poor stars are possible but should be very rare, since they represent only a small range in mass.

Further studies of globular clusters should allow fainter cluster members to be identified based upon their proper motions. In addition, deep spectroscopy may allow the spectroscopic classification to be tested directly. Unfortunately, most of the closest and hence most favorable targets are in the southern hemisphere, and will have to await the new telescopes under construction.

Other properties of the metal-poor main sequence need to be investigated. We have obtained Hubble Space Telescope time which should allow an estimate of the binary fraction of M subdwarfs to be made for the first time. In addition, there is a good possibility that a system suitable for mass determinations will be identified. Empirical masses to test the stellar models are badly needed.

Finally, this thesis shows that properties of M subdwarfs are becoming well enough understood that they can become probes of the Galactic halo. Since they are much more abundant than higher mass stars, the local sample can be greatly increased

and, in principle, trigonometric parallaxes can be obtained. Furthermore, their low temperatures mean that different elements are observable, which will eventually allow new probes of the chemical history of the Galaxy. The oxygen abundance is thought to have a significant effect on M subdwarf spectra, and new models may allow the oxygen abundances of the halo to be investigated in a new and independent way.